Master of Science Thesis

Potential Flow Modelling of Boundary Layer Ingesting Configurations

Tomáš Kukučka

Delft University of Technology

TUDelft

Master of Science Thesis

Potential Flow Modelling of Boundary Layer Ingesting Configurations

by

Tomáš Kukučka

as a requirement for obtaining the degree of Master of Science
at Delft University of Technology,
to be defended publicly on Thursday the 22nd of June, 2023 at 13:30.

Student number:	4542703	
Thesis committee:	Prof Dr. Ing. Georg Eitelberg,	TU Delft, chair
	Dr. Tomas Sinnige,	TU Delft, supervisor
	Dr. Anh Khoa Doan,	TU Delft
Daily supervisor:	Martijn van Sluis, MSc	TU Delft

Cover: Taken somewhere over the Atlantic Ocean while writing this thesis

TUDelft

Acknowledgements

I would like to thank everyone who helped me during the course of writing this thesis. First and foremost I would like to thank Martijn van Sluis, who supervised me on a daily basis and was always available for discussions. I would also like to thank Tomas Sinnige and Georg Eitelberg, who gave me expert feedback multiple times during the course of this work. Last but not least, I would like to thank my parents and my friends, who always supported me and were there when I needed them.

Tomáš Kukučka
Delft, June 2023

Summary

Boundary Layer Ingestion (BLI) is a promising technology for reducing the impact of aviation on the environment. By placing a propulsor on an aircraft such that it ingests the slower moving air within the boundary layer, a decrease in power consumption can be achieved. Evaluating the performance of BLI configurations remains a challenge though. Many conventional methods for computing the thrust and drag of an aircraft cannot be used due to the interference between the airframe and the propulsor. As a result, researchers have to rely on either low fidelity methods with limited accuracy, or on expensive CFD simulations. In this work, an attempt was made to create a computationally inexpensive method that can evaluate the drag, thrust and propulsive power of an axisymmetric fuselage with a BLI propulsor. The method proposed relies on potential flow modeling and makes use of a boundary layer model and several corrections.

The first step of creating the computational model focused on modelling the fuselage as a body of revolution. This has been done by creating a potential flow model and coupling it with a laminar and a turbulent boundary layer model. The second step concerned the modelling of the actuator disc. An existing potential flow actuator disc model was used as a basis. Several adjustments have been made to it in order to increase its stability and make coupling it with the body of revolution model possible. In the third step, the two models were coupled together and a correction has been formulated for taking the boundary layer wake into account.

The various parts of the model, as well as the combined computational model have been progressively validated using experimental and CFD results. Several methods for computing the surface pressure along the body have also been investigated. A method for correcting the surface pressure based on flow curvature within the boundary layer was derived. Based on validation using experimental data, the model was shown capable of predicting drag as well as pressure distributions within and outside of the boundary layer. Taking the APPU configuration as an example, the possibility of computing the power saving coefficient was demonstrated.

Contents

List of symbols

Symbol	Definition	Unit
C_d	Drag coefficient	-
C_f	Friction coefficient	-
C_P	Pressure coefficient	-
C_T	Thrust coefficient	-
D_p	Pressure drag	N
D_v	Viscous drag	N
D_t	Total drag	N
F_c	Centripetal force	N
H	Shape factor	-
J	Advance ratio	-
L	Length	m
M	Mach number	-
N	Number	-
$\dot{m}$	Mass flow	kg/s
P	Power	W
p_s	Static pressure	Pa
p_t	Total pressure	Pa
q	Dynamic pressure	Pa
R	Radial coordinate	m
r_c	Radius of curvature	m
Re	Reynolds number	-
T	Thrust	N
U	Velocity	m/s
X	Streamwise coordinate	m
x	Distance along body surface	m
y	Distance above body surface	m
α	Surface angle	Rad
ρ	Air density	[kg/m^3]
δ	Boundary layer thickness	m
δ_1	Displacement thickness	m
δ_2	Momentum thickness	m
μ	Dynamic viscosity	kg/m/s
τ	Wall shear stress	Pa

Acronyms

APPU	Advanced Propulsion and Power Unit
APU	Auxiliary Power Unit
BET	Blade Element Theory
BLI	Boundary Layer Ingestion
BOR	Body of Revolution
CENTRELINE	Concept validation study for fuselage wake-filling propulsion integration
CFD	Computational Fluid Dynamics
DisPURSAL	Distributed Propulsion and Ultra-high By-Pass Rotor Study at Aircraft Level
EIS	Entry Into Service
ESDU	Engineering Sciences Data Unit
LTT	Low Turbulence Tunnel
NASA	National Aeronautics and Space Administration
NOVA	Nextgen ONERA Versatile Aircraft
ONERA	French National Aerospace Research Centre
PBM	Power Balance Method
PSC	Power Saving Coefficient
RANS	Reynolds-Averaged Navier-Stokes
STARC-ABL	Single-Aisle Turboelectric Aircraft with an Aft Boundary-Layer Propulsor

1

Introduction

According to the goals set up by the Flightpath 2050 Europe's Vision for Aviation, the CO_2 emissions and NO_x emissions of air travel must be reduced by 75 % and 90 % respectively per passenger kilometer by the year 2050 with respect to the year 2000 benchmark [1]. As a result, a lot of research is currently aimed at progressively reducing the emissions of aircraft. One of the technologies that received much attention in the past decade is Boundary Layer Ingestion (BLI), a technology that has been long known in the field of marine engineering. Integrating the propulsor such that it ingests the relatively slow moving boundary layer of the airframe rather than the much faster external flow, the propulsive efficiency of the system can be increased. [2] The fuselage of an airplane is the most suitable component for BLI due to its large contribution to the total viscous drag [3]. Several transport aircraft with an aft fuselage BLI propulsor were conceptualized and studies have concluded that a reduction of fuel consumption in the range of 4.7 to 14 % may be possible [4, 5, 6].

Currently, the Advanced Propulsion and Power Unit (APPU) project[1] running at Delft University of Technology is aimed at investigating the applicability of BLI technology to the Airbus A320. The proposed configuration replaces the Auxiliary Power Unit (APU) with the APPU, a hydrogen powered gas turbine that apart from generating electrical power will be also used to drive a BLI open rotor at the end of the fuselage. Preliminary studies have shown that a 20 % reduction in CO_2 emissions may be possible.

One of the greatest challenges behind researching and designing BLI aircraft configurations comes from quantifying performance metrics such as drag, thrust and the propulsive power. The problem is caused by interference effects between the airframe and the propulsor. These effects however, are also responsible for the power saving benefit of BLI and modelling them accurately is therefore crucial.

The aim of this thesis will be to develop a computational model based on potential flow for computing the drag and the propulsive power of BLI configurations. In order to limit the scope of this thesis, the model will consider a propulsor and an axisymmetric fuselage only. A boundary layer model and several corrections will be implemented in in order to take the interference between the body and the propulsor into account. Once validated, the method could become a useful tool for research and preliminary design of propulsive fuselage concepts. Potential uses of the model could include design space exploration, preliminary optimization of the fuselage geometry or the correction of wind tunnel experimental data.

The structure of this thesis will be as follows: A literature review on the topic of BLI will be presented in chapter 2 followed by a definition of the research objective in chapter 3. The next three chapters will focus on a detailed explanation of the steps taken to develop and validate the computational model. The Body of Revolution (BOR) model will be discussed in chapter 4, the actuator disc model in chapter 5 and chapter 6 will focus on combining the two models together. The entire computational model will be then validated in chapter 7, which will be followed by a model capability demonstration presented in chapter 8. Finally, conclusions and recommendations regarding this work will be made in chapter 9.

---

[1]Advanced Propulsion and Power Unit, accessed 21 January 2022, `https://www.tudelft.nl/lr/appu`

2

Literature review

Prior to starting this thesis, a literature review was conducted in the field of BLI. The main objective of this literature review was to gain a general overview of the topic, the past and ongoing research and the current status of the technology. Ultimately, this was used as a baseline for the formulation of the topic of this thesis, that builds on the existing body of knowledge and is relevant to the ongoing research at Delft University of Technology.

In this chapter, a summary of the literature study will be provided in order to familiarize the reader with the basic concepts and show the importance of the work done in this thesis. The structure of this chapter will be as follows: First, the topic of BLI will be introduced in section 2.1. The problems related to evaluating the performance of BLI configurations will be then discussed in section 2.2. Finally, an overview of existing and proposed BLI configurations will be provided in section 2.3.

2.1. Introduction to boundary layer ingestion

Mathematically, the benefit of BLI was explained by Arntz [7] as follows: The thrust force produced by a propulsor is proportional to the velocity increase over the propulsor, however the power consumption of the propulsor is proportional to the difference of the velocities squared. This means that for a given thrust, the required mechanical power increases with the inlet velocity and therefore by placing the propulsor within the slow moving wake, the same thrust can be produced with lower power.

Some of the first investigations into the application BLI for air propulsion were carried out by McLemore [8] on an airship model in a wind tunnel. The study has shown that BLI stern mounted propellers can achieve much higher propulsive efficiencies than propellers mounted to the side of the airship hull, outside of the boundary layer. Another observation that was made is that the presence of the propulsor has an effect on the drag of the airship. Because it is located near the trailing edge of the body, the flow over the tail cone is accelerated, which results in an increase in drag. The increase in propulsive efficiency was however found to be greater than the increase in the drag of the body. As a result the study concluded that the BLI airship configuration should therefore have a greater range and endurance.

2.2. Quantifying performance of BLI configurations

As was shown by the study of McLemore [8], the thrust of a propulsor and the drag of the body are not independent for BLI configurations. The drag of the body is influenced by the presence of the propulsor and the thrust of the propulsor is influenced by the presence of the body.

Problems with evaluating thrust and drag

The first problem created by this dependency is the fact that computationally evaluating drag and thrust becomes more difficult. For a non-BLI configuration, it is often acceptable to evaluate the thrust of the propulsor and the drag of the body in isolation and assume that they remain the same when they are combined. This cannot be done for BLI configurations and some sort of iteration between the thrust and drag models is required.

Furthermore, Trefftz plane analysis also cannot be used for BLI configurations. For non-BLI configurations it is possible to separate stream tubes into ones that have been affected by the body (hence

carry information about drag) and once that have been affected by the propulsor (hence carry information about the thrust). When BLI takes place, this is no longer possible as some stream tubes that have been effected by the body also pass through the propulsor and therefore only carry information about the net force. This problem can be understood by looking at the simple sketch shown in Figure 2.1, that was presented in the work of Arntz [7].
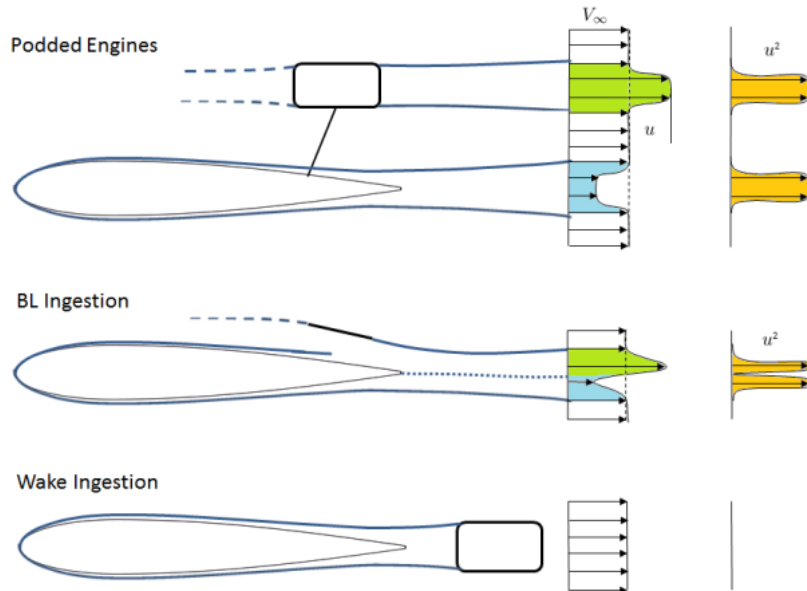

Figure 2.1: A sketch explaining the effect of BLI and wake ingestion on the velocity measured across the Trefftz plane. [7]

Looking at the idealized wake ingesting configuration, we can see that the entirety of the wake is ingested by the propulsor, which perfectly accelerates all of the flow back to the freestream velocity. Using Trefftz plane analysis, we would therefore find that the thrust and drag are both equal to zero, which is certainly not the case. Looking at the BLI configuration, we see that the velocity increase created by the propulsor overlaps with the velocity deficit created by the body and therefore it is not possible to separate them.

Measuring the thrust and drag experimentally also becomes more difficult for BLI configurations. When BLI is not taking place, the drag of the body and the thrust of the propulsor can be measured in isolation[1]. For BLI however this cannot be done and a separate load cell must be used to measure the thrust of the propulsor when it is installed on the body.

Power instead of drag
The second problem stemming from the thrust and drag being dependent on each other in BLI configurations is the fact that minimizing drag is no longer a good aircraft design objective. As was discussed previously, introducing a BLI propulsor increases the drag of the body, but this is overcome by the increase in propulsive efficiency. The design point minimizing power consumption therefore does not coincide with the one that minimizes drag. As a result, a BLI configuration has to be optimized directly for power consumption instead.

A metric that is often used for quantifying the benefit gained from BLI is the Power Saving Coefficient (PSC). Introduced by Smith [2], it is the fraction of power saved by switching from non-BLI to BLI propulsion on a particular airframe. The PSC is given by Equation 2.1, where P is the shaft power required to operate the BLI aircraft in equilibrium and P_{ref} is the power required to operate the reference configuration. As an example, the PSC of an aircraft with a pusher propeller can be evaluated by comparing it to a fictional configuration where the propeller is placed away from the airframe such that there is no interaction between the two.

---

[1]For non-BLI configurations, there is also always going to be some interference between the propulsor and the body. It can however be assumed to be much lower and neglecting it will therefore have a much less impact on the results.

$$\text{PSC} = \frac{P_{\text{ref}} - P}{P_{\text{ref}}} \tag{2.1}$$

2.2.1. Momentum, power and exergy balance methods

In practice, a variety of techniques are used for quantifying the performance of BLI aircraft and can be categorized as either momentum integral methods, energy integral methods or exergy integral methods.

Momentum integral schemes are based on formulating a momentum equilibrium in order to compute drag and thrust. This is often difficult for BLI configurations as some streamtubes are affected by both the propulsor and the airframe and hence carry only information about the net force. As a result, momentum integral methods often make large assumptions and neglect some of the interaction effects between the airframe and the propulsor. They are often used despite their lower accuracy, as they are relatively inexpensive from a computational perspective compared to the other methods. [9]

The first energy integral method was presented by Drela [10] and was considered a significant breakthroughs in performance bookkeeping for BLI configurations. The Power Balance Method (PBM) allows the propulsive power of the aircraft to be evaluated by creating a power balance over the control volume S, as shown in Figure 2.2.
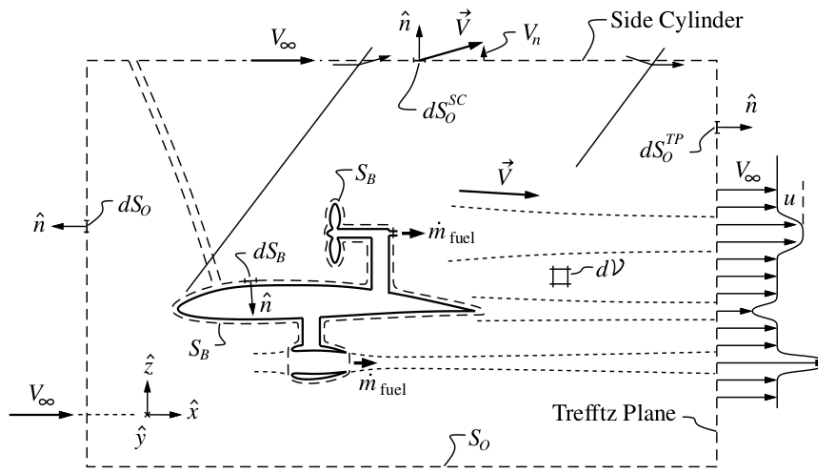

Figure 2.2: The control volume around an arbitrary propelled aerodynamic body used by the PBM. [10]

The sinks and sources of power into and out of the control volume, are equated as is shown in Equation 2.2. The power sources are on the left and the power outflows on the right hand side of the equation.

$$P_S + P_V + P_K = \dot{\mathcal{E}} + \Phi \tag{2.2}$$

The term P_S represents the net propulsor shaft power, which is computed by integrating the force multiplied by velocity over all moving surfaces. This term, for example, takes into account the power supplied by a propeller. The term P_V is the volumetric power from fluid expanding against the atmospheric pressure. This is only significant when heat is added into the system, for example, from a turbojet engine. Finally, the term P_K is the net propulsor mechanical energy inflow rate. This term is used if the propulsor is considered to be outside of the control volume, like the one underneath the body in Figure 2.2.

On the right hand side of the equation are the outflows of power from the control volume. The term $\dot{\mathcal{E}}$ is the net mechanical energy outflow through the Trefftz plane and the side boundaries and the term Φ is the dissipation of kinetic energy into heat withon the control volume.

The PBM makes it possible to unambiguously calculate the BLI benefit from a flow field around an aircraft computed using Computational Fluid Dynamics (CFD) or form detailed wind tunnel measurements. The disadvantage of this method is that a detailed flow field is required which makes the method less suitable for conceptual design or design optimizations.

The third kind of methods for evaluating the performance of BLI configurations are the exergy balance methods, the first of which was introduced by Arntz [7]. The method combines a momentum balance with the first and second laws of thermodynamics. Exergy, the quantity preserved by this method is the part of energy that is theoretically convertible into useful work. An advantage of this method over the PBM is that in addition to the mechanical power, it is also capable of taking thermal energy into account. The method does however also require a resolved flow field as input, just like the PBM.

2.3. Overview of existing and proposed aircraft

A handful of aircraft with BLI propulsion were designed in the 20th century, however the maximization of efficiency was not a part of the main design considerations [6]. An early example of such an aircraft is the Douglas XB-42, which is shown in Figure 2.3. Other examples include the RFB Fantrainer, the LearAvia LearFan 2100 and the Grob GF 200.

Figure 2.3: An early example of an aircraft utilizing BLI was the Douglas XB-42, which conducted its first flight in 1944. Picture taken from Wikimedia Commons[2].

In the 21st century as fuel prices increased and the concern for environmental impact of aviation started to grow, BLI propulsion slowly started to become more interesting. Several BLI configurations of transport aircraft have been proposed over the past 20 years. A summary of the most notable developments will now be presented in chronological order.

The Blended Wing Body concept
The applicability of BLI to the National Aeronautics and Space Administration (NASA) Blended Wing Body concept was analyzed by Kawai [11] in 2006. The configuration is shown in Figure 2.4 and features turbofan engines that ingest the thick boundary layer that forms over the top of the body. The study concluded that a fuel saving of up to 10 % may be achieved when using BLI engines instead of podded engines. Some disadvantages were highlighted, such as lower inlet pressure recovery and flow distortion which can reduce the efficiency of a turbofan engine.

The D8 configuration
One of the first developments in the field of BLI that received considerable attention was arguably the D8 configuration that was first conceived in 2010 by Greitzer [12], as a part of the NASA N+3 program. Shown in Figure 2.5, the D8 configuration features a wide "double-bubble" fuselage, a twin pi-tail and is meant to serve as an airliner for the 180 passenger, 3000 nm range market with an Entry Into Service (EIS) year of 2035. The engines are mounted near the rear stagnation point of the fuselage, flush with the top surface and ingest around 40 % of the fuselage boundary layer. The fuselage also serves as a diffuser and a flow aligner, hence smaller nacelles are required which reduces drag and weight. [13]

A design optimization with the aim of minimizing fuel burn of the D8 was presented by Drela [14] and was followed by wind tunnel experiments of a 1:11 scale powered model by presented by Uranga [13].

---

[2]Wikimedia Commons, accessed 3 June 2023, `https://commons.wikimedia.org/wiki/File:XB-42.jpg`

Figure 2.4: A render of the Blended Wing Body concept with boundary layer ingesting turbofan engines. [11]

Figure 2.5: A model of the D8 configuration in the NASA Langley's wind tunnel. [13]

Experimental results showed a BLI benefit of around 6 % when comparing the boundary layer ingesting configuration to an alternative with pylon mounted engines. Validation of the results was performed by Uranga [15] by employing the PBM and the BLI benefit was quantified to be 8.6 +- 1.8 %. It was also predicted that the configuration should achieve a 36 % fuel burn reduction compared to a traditional tube and wing aircraft design.

Project DisPURSAL

Funded by the European Comission, Distributed Propulsion and Ultra-high By-Pass Rotor Study at Aircraft Level (DisPURSAL) was a project that started in 2013 and lasted for two years. The aim of the project was to investigate the fuel saving potential of distributed propulsion for the purpose of medium to long range aircraft for EIS year 2035. Two concepts were considered within the study, both of which are shown in Figure 2.6. The first was a traditional tube and wing configuration with an additional BLI turbofan engine mounted in the tail section of the fuselage. The second was a hybrid wing body concept with two turbofan engines, each powering two additional ducted fans through mechanical transmission. All fans were mounted on the top surface with the aim of ingesting the boundary layer of the body. [16]
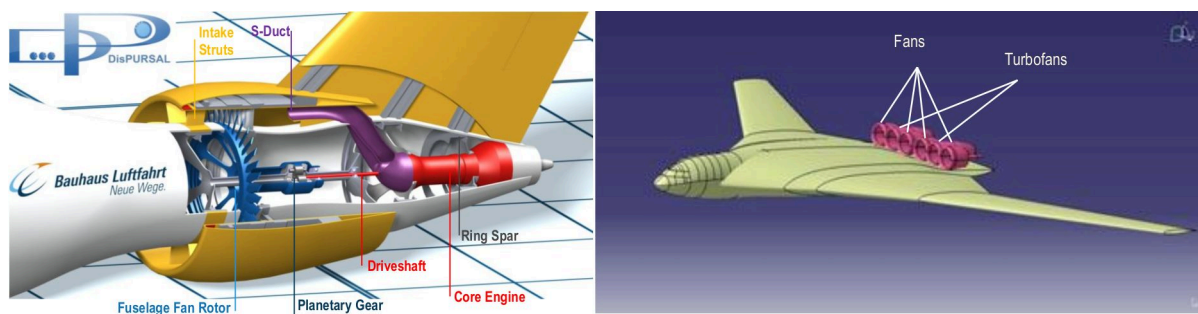

Figure 2.6: The tube and wing configuration (left) and the hybrid wing body (right) considered within the DisPURSAL study. [16]

The concepts were analyzed with an integral momentum thrust and drag bookkeeping scheme described by Seitz [17]. Compared to a projected 2035 traditional configuration reference aircraft, a fuel saving of around 9-14 % was estimated for the tube and wing configuration and 8 % for the hybrid wing body. The disadvantages of these configurations were found to be increased system complexity and a stronger coupling between the aerodynamic characteristics and the thrust setting. Additionally, fan inlet distortion was identified as a concern for both concepts. A challenge found with the tube and wing configuration is the transmission of loads from the empennage across the fuselage fan. [4]

The NOVA configuration

As a part of work conducted at the French National Aerospace Research Centre (ONERA), in 2016 Wiart [18] presented four Nextgen ONERA Versatile Aircraft (NOVA) configurations. The configurations were proposed for an EIS year 2025 and were sized for a range of around 5600 km and a capacity of 180 passengers. One of the four configurations made use of BLI semi-buried turbofan engines in the aft fuselage, that ingest around 40 % of the fuselage boundary layer. The PSC was calculated from Reynolds-Averaged Navier-Stokes (RANS) simulations where the fan was modelled as an actuator disc. A PSC of 5 % was estimated at cruise conditions.

Figure 2.7: An artistic representation of the NOVA configuration with BLI propulsion. [18]

The STARC-ABL concept

In another 2016 study, Welstead [5] presented the Single-Aisle Turboelectric Aircraft with an Aft Boundary-Layer Propulsor (STARC-ABL), which is shown in Figure 2.8. The configuration is powered by two under wing engines and power is transmitted electrically to a BLI fan mounted to the end of the fuselage. The configuration was developed by NASA as a fist look into turbo-electric propulsion, to see if a BLI benefit can be achieved that overcomes the losses introduced by power conversion. The concept was sized to a mission profile of a Boeing 737/Airbus A320 and designed for EIS year of 2035.
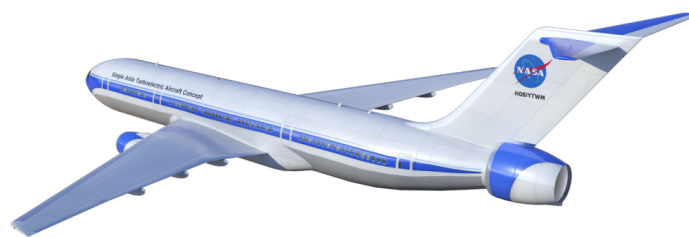
Figure 2.8: An artistic representation of the STARC-ABL configuration proposed by NASA. [19]

In order to perform design optimizations, the performance was estimated using a simple method that involved predicting the boundary layer properties by interpolating existing CFD results for flow over fuselage. Interestingly, the propulsion system weight of the turbo-electric concept was found to be lower than that of the reference system. This was explained by the reduced diameter of the turbofans engines and the higher efficiency of the fuselage fan. Improvements of 15 % and 12 % were observed in the thrust specific fuel consumption and the mission fuel burn respectively, compared to a reference configuration without the fuselage fan.

Project CENTRELINE

Successor to DisPURSAL, Concept validation study for fuselage wake-filling propulsion integration (CENTRELINE) was a 42 month project that concluded in 2020. The aim was to investigate a tube and body configuration with a fuselage fan, turbo-electrically driven by two under wing turbofan engines. Similar to STARC-ABL concept, the CENTRELINE configuration is shown in Figure 2.9. The staring point of the design was based on the Airbus A330 and an EIS year of 2035 was assumed. [6] An aero-shaping optimization of the design was performed by Seitz [3] using two dimensional RANS simulations. A momentum control volume approach was used to quantify the forces acting on components. The resulting design was then validated using three-dimensional CFD simulations.

Figure 2.9: An artistic representation of the CENTRELINE concept. [6]

Wind tunnel tests of the configuration were carried out at Delft University of Technology by Della Corte [20]. Particle image velocimetry measurements have shown that the fuselage fan alters the behavior of the flow both upstream and downstream. Acceleration of the flowfield both upstream and downstream of the fan results in a reduction of the boundary layer thickness. Further,a reduction in pressure over the backward facing surface creates additional pressure drag. By assessing the flowfield using the PBM, it was also shown that the rate of kinetic energy deposition upstream of the fan increases with the power setting due to the accelerated flow. The experimental measurements also uncovered that swirl introduced by the rotor causes flow separation over the aft cone, which results in additional drag. The angular velocity of the spinning flow increases with reducing diameter of the aft cone until it cannot resist the centrifugal force and separates.

The conclusions of the project were that a PSC of 8.5 % might be achievable under ideal power transmission conditions and the total fuel burn benefit from BLI was estimated to be around 4.7 % when the configuration was compared to a similarly advanced non-BLI configuration.

3

Problem Definition

The main focus of this chapter is to formulate the objective of the thesis and research questions that are to be answered. First a knowledge gap will be identified in section 3.1 based on the literature study. The research questions and objective will then be formulated in section 3.2. Finally, the proposed methodology for conducting the research will be presented in section 3.3.

3.1. Knowledge gap and thesis topic formulation

As outlined in the previous chapter, numerous studies have analyzed BLI aircraft configurations over the past few decades. Many of them have shown that BLI is a promising technology in achieving significant fuel burn reductions. What most of these studies have in common is the focus on a near future application with an EIS year 2035. For such near future application, ingestion of the boundary layer by a single propulsor attached to the end of the fuselage is seen as the most promising concept. This concept is particularly attractive because a relatively large power saving can likely be achieved with making the least changes to proven aircraft designs.

It was also observed that most of the studies had to rely on simplified methods that neglect important interaction effects between the propulsor and the body for performance evaluation during the early design phases. This trend was also observed by Habermann [9], who explained that more powerful methods such as the power balance and exergy balance methods which can predict these interactions are computationally expensive and hence unsuitable for optimizations and design space exploration. Shown in Figure 3.1, Habermann plotted performance bookkeeping methods used up to date based on their applicability to concept phase and their universality.
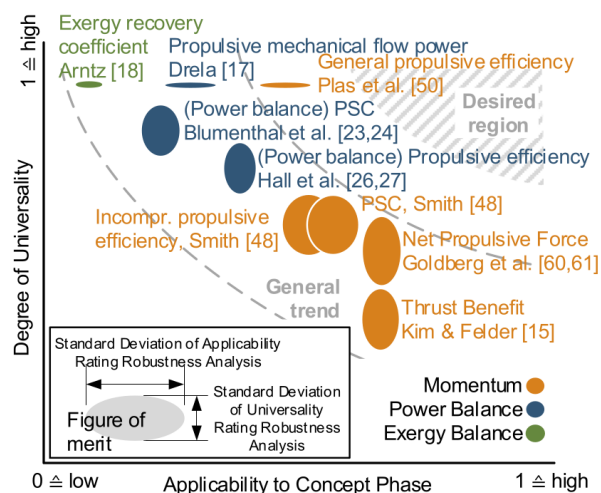

Figure 3.1: The applicability and universality of performance bookkeeping schemes. The image and the references within it come from the study of Habermann [9].

9

The degree of applicability to concept phase and universality of the various methods was determined based on many different considerations. In the simplest sense though, applicability to concept phase represents how computationally cheap the method is and universality represents how accurate it is when applied to BLI configurations. As can be seen, most methods are either universal or applicable to conceptual phase, however none of the methods lie in the "desired region".

Based on these observations, it is evident that there is a lack method with the following characteristics:

- Computationally inexpensive
- Takes into account the effect of the propulsor on the airframe
- Takes into account the effect of the airframe on the propulsor
- Allows the evaluation of drag, thrust and power consumption

A study performed by Kriebel [21] provided a great deal of inspiration in conceptualizing a method that could fulfill these criteria. Kriebel investigated an underwater hull with a stern mounted ducted propeller and used potential flow to evaluate the net forces acting on the hull, the duct and the propeller. Given the limited computing capabilities in 1964, the approach used was very simplistic. The body was represented by a source-sink distribution and multiple vortex cylinders stemming from the aft cone were used to model the thick boundary layer. The ducted propeller was represented using a single vortex tube stemming from the trailing edge of the duct and the duct its self was represented using a distribution of vortex rings. The system was solved iteratively in order to approximately satisfy basic boundary conditions.

Following a literature study on modelling techniques, three ways in which the accuracy of Kriebel's method could be improved have been identified. First of all, the propulsor could be modelled as an actuator disc using, for example the method described by Van Kuik [22]. This method works by distributing vortex rings along the slipstream and solving their strengths and radii such that the slipstream is force free and lies along a streamline. The second point of improvement concerns the determination of boundary layer properties. While Kriebel relied on experimental measurements, being able to compute the boundary layer properties would make it possible to simulate arbitrary shapes without the need of wind tunnel testing. Further, it would also open up the possibility to iterate between the potential flow solution and the boundary layer model as is often done by potential flow solvers such as X-Foil [23].

As was observed by Patel [24], several problems exist with applying boundary layer models to the flow over the aft cone of a BOR. The boundary layer over the aft cone undergoes rapid expansion and many of the assumptions used for modelling of thin boundary layers fall apart. The pressure across the boundary layer is no longer constant and wall-normal velocity is no longer negligible. Further, the turbulence levels within the boundary layer are lower than what two-dimensional models would predict. These observations were also confirmed by the more recent studies of Della Corte [25] and Blantrapu [26]. For these reasons it is necessary to use a thick axisymmetric boundary layer model, developed for the flow around BORs, such as the one proposed by Patel [27]. While this model still makes some simplifications, such as assuming that the flow is parallel to the surface, Patel has demonstrated that it is capable of providing good estimates of the boundary layer development over the aft cone of a BOR.

The third point of improvement is with respect to the modelling of of the boundary layer within the potential flow model. In the work of Kriebel this was done using vortex cylinders stemming from the aft cone, the strengths of which were tuned such that the boundary layer momentum deficit matched that of experimental measurements. This modelling procedure could be improved by using an equivalent body approach, in which the displacing effect of the boundary layer is achieved within potential flow by placing the surface of the body at the displacement thickness of the boundary layer. This approach would allow the boundary layer thickness to vary along the length of the body as predicted by the boundary layer model.

3.2. Research questions and objective

Based on the discussions of the previous section, the following overarching research question was established:

- To what extent can potential flow coupled with a boundary layer model be used to predict the drag, thrust and power of a propulsive fuselage concept.

In order to help guide the work, a set of sub questions was also established. Regarding a propulsive fuselage configuration modelled using potential flow and a thick axisymmetric boundary layer model:

- With what accuracy can the model predict the development of the boundary layer over the body?
- What simplifications can and cannot be made when computing the surface pressure distribution?

    – What is the effect of neglecting pressure variations across a boundary layer profile over the aft cone of the BOR?
    – Is it reasonable to define the boundary layer profile as perpendicular to the surface?

- To what accuracy can the model predict the drag of the body? What is the effect on neglecting the development of the boundary layer wake?
- What are the best practices for creating such a computational model?

    – What is the most suitable way of discretizing the geometry?
    – What iterative procedure works the best for combining the various parts of the model?

Given these research questions, the objective of this thesis was defined as follows:

To analyze the possibility of potential flow modeling coupled with a boundary layer model for analyzing propulsive fuselage concepts by means of developing a computational model and validating it using experimental results.

3.3. Methodology and assumptions

In order to execute the thesis proposed and answer the research questions, the model as described in the previous sections will be constructed in several stages. Progressive validation the the model will be conducted at each stage of development to quantify the effect of every addition to the model. This will ensure that each element of the model is functioning as intended and is making the model more accurate altogether. The results of the model will be compared to both experimental and other computational results. The first step will be the construction of a potential flow model of a BOR. This model will be then combined with the boundary layer model to form an equivalent body model. The actuator disc model will be developed in parallel and finally merged with the equivalent body model.

The entire computational model will be constructed in Python from scratch. This programming language was chosen as it is flexible and simple to use. While other programming languages could be more computationally efficient, this study aims at the development of a proof of concept, which may involve the testing of a variety of different approaches. The ease of implementation was therefore prioritized over computational speed.

Throughout this thesis, the following general assumptions will be used, even when not stated explicitly:

- The geometry and the flow around it are assumed to be axisymmetric.
- The Mach number is assumed to be zero. As a result, the flow is considered to be incompressible.
- The point of boundary layer transition is presumed to be known.
- Potential flow is assumed outside of the boundary layer.
- The propulsor is assumed to be an infinitely thin actuator disc that provides a sudden uniform increase in total pressure.

The axial symmetry assumption results in a quasi three dimensional model. This is because the geometry and flow are prescribed to remain constant over one of the dimensions. Note that this is not the same as two dimensional model. Even when inviscid, the flow around a symmetric airfoil is different to the flow around a BOR which is created by revolving the same airfoil.

For the construction of the computational model, use will be made of two coordinate systems, as shown in Figure 3.2. The $X - R$ coordinate system is the main, global system, where R represents the radius in cylindrical coordinates. Unless stated otherwise, the trailing edge of the BOR and the actuator disc will be assumed to lie on the origin, where $X = 0$.

The $x - y$ coordinate system is a secondary system bound to the BOR and is mainly used within the boundary layer model. The x axis starts at the leading edge of the BOR, follows the surface and ends at the trailing edge. The y coordinate is always normal to the surface of the BOR. Because of the axial symmetry, it is generally not possible to specify an azimuthal angle ψ in either of the two coordinate systems, although it may appear in the derivation of formulas.
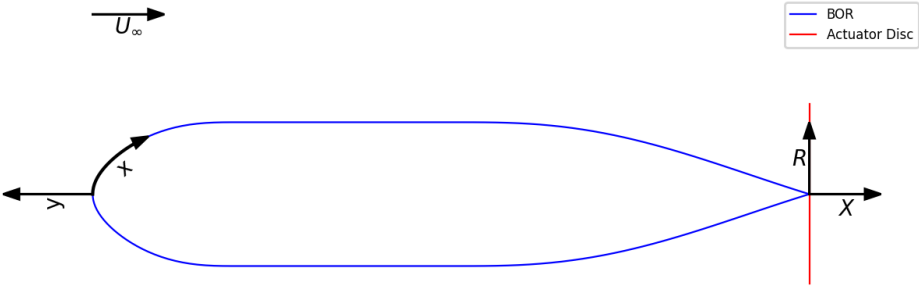
Figure 3.2: The global $X - R$ coordinate systems and the secondary $x - y$ system used by the boundary layer model.

4

The body of revolution model

The axisymmetric flow around the BOR is modelled using the equivalent body approach, where a potential flow model is coupled with a boundary layer model. The method is analogous to the modelling of flow around a two dimensional airfoil by software such as X-Foil [23]. Similar computations have already been performed, for example by the Engineering Sciences Data Unit (ESDU) [28].

The idea behind this modelling strategy is as follows: A potential flow model is used to compute the velocity distribution along the boundary layer edge. Using this as input, a boundary layer model is used to compute the development of the boundary layer along the surface of the BOR. In order to take the presence of the boundary layer into account within the potential flow model, the surface of the BOR is moved to the displacement thickness of the boundary layer to form an equivalent body. Because the boundary layer overall and displacement thicknesses are initially unknown, they are assumed to be zero in the first iteration and the two models are ran in turns until convergence is achieved.

The structure of this chapter is as follows: The potential flow and the boundary layer models are first written and validated side by side and are described in sections 4.1 and 4.2 respectively. section 4.3 then describes how the two are merged together to form an equivalent body model. The computation of surface pressure and the drag of the body is then discussed in section 4.4. Finally, the validation of the equivalent body model is performed in section 4.5.

4.1. The Potential flow model

The BOR potential flow model is based on the work of Von Karman [29] and works by placing a distributing n line segment sources along the axis of symmetry and m control points[1] along the surface of the body. An example is shown in Figure 4.1. The strengths of the sources are solved for, such that the velocity components normal to the body surface are zero at the locations of the control points.

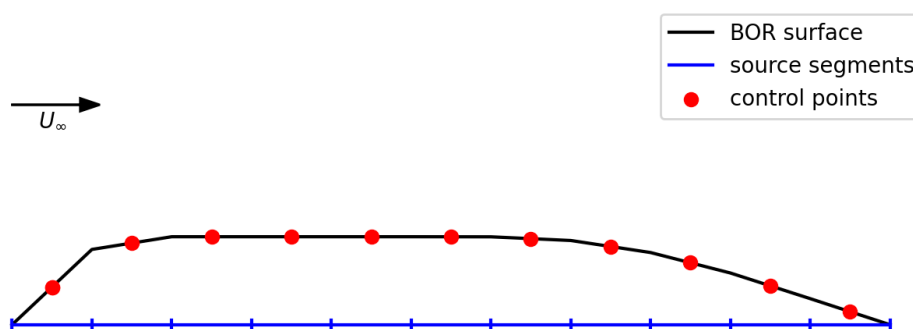**Figure 4.1:** Example of a distribution of 12 source segments and 12 control points along a body of revolution.

---

[1]In reality they are not points but rings, but for simplicity they will be referred to as "control points" throughout this thesis.

The X and R velocity components $U_{X,ij}$ and $U_{R,ij}$ induced by a source segment i at the location of a control point j are given by Equations 4.1 and 4.2 [29]. Here, Q_i and l_i are the strength and length of the source segment i and ρ'_{ij}, ρ''_{ij}, $\Delta X'_{ij}$, $\Delta X''_{ij}$ and R_j are all distances shown in Figure 4.2. Both of these equations can be rewritten as a constant k multiplied by Q_i.

$$U_{X,ij} = \frac{Q_i}{4\pi l_i R_j} \left(\frac{R_j}{\rho''_{ij}} - \frac{R_j}{\rho'_{ij}} \right) = k_{X,ij} Q_i \tag{4.1}$$

$$U_{R,ij} = -\frac{Q_i}{4\pi l_i R_j} \left(\frac{\Delta X''_{ij}}{\rho''_{ij}} - \frac{\Delta X'_{ij}}{\rho'_{ij}} \right) = k_{R,ij} Q_i \tag{4.2}$$
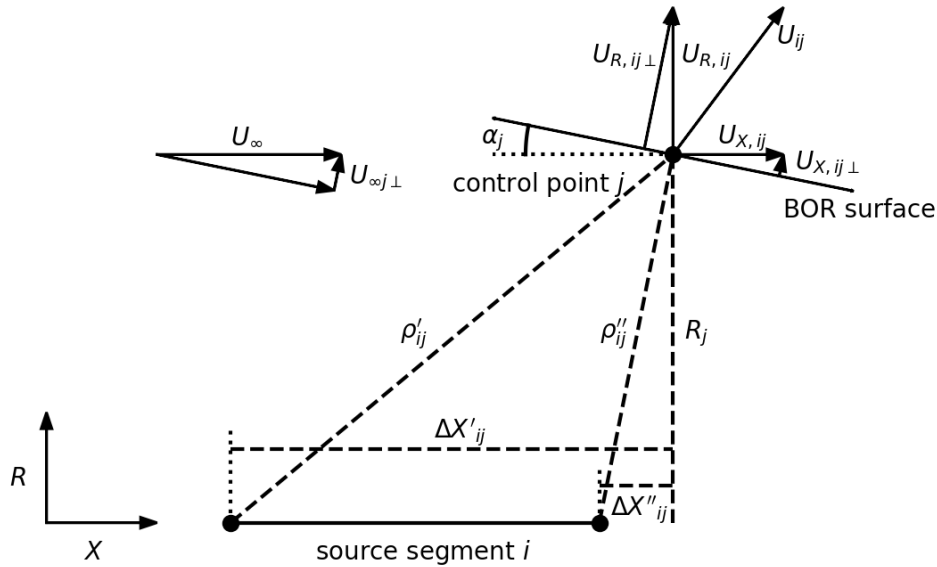

Figure 4.2: Schematic explaining the various variables required to compute the velocity induced by a source segment i and the freestream velocity U_∞ at a control point j in the direction normal to the body surface.

4.1.1. Solution procedure

With n source segments and m control points, a system of m equations with n unknowns can be formulated. Each equation j can be constructed by summing up the induced velocities of each of the source segments i as well as the freestream velocity U_∞ at the location of the control point j in the direction normal to the surface of the BOR and equating this sum to zero. This can be done by looking at Figure 4.2 and the result is shown in Equation 4.3, where the subscript $\perp$ represents the part of a velocity component normal to the BOR surface.

$$\sum_{i=1}^{n} (U_{X,ij\perp} + U_{R,ij\perp}) + U_{\infty j\perp} = 0 \tag{4.3}$$

Using the angle of the surface α_j at control point j, the equation can be written in terms of the velocity components $U_{X,ij}$ and $U_{R,ij}$, as is shown in Equation 4.4. Finally, Equations 4.1 and 4.2 are substituted in to form Equation 4.5. The entire system of equations can be then written in matrix form as is shown in Equation 4.6.

$$\sum_{i=1}^{n} (U_{X,ij} \sin \alpha_j + U_{R,ij} \cos \alpha_j) + U_\infty \sin \alpha_j = 0 \tag{4.4}$$

$$\sum_{i=1}^{n} (k_{X,ij} \sin \alpha_j + k_{R,ij} \cos \alpha_j) Q_i = -U_\infty \sin \alpha_j \tag{4.5}$$

$$\begin{bmatrix} a_{11} & a_{21} & \dots & a_{n1} \\ a_{12} & a_{22} & \dots & a_{n2} \\ \vdots & \vdots & \ddots & \vdots \\ a_{1m} & a_{2m} & \dots & a_{nm} \end{bmatrix} \begin{bmatrix} Q_1 \\ Q_2 \\ \vdots \\ Q_n \end{bmatrix} = \begin{bmatrix} b_1 \\ b_2 \\ \vdots \\ b_m \end{bmatrix} \qquad = \qquad \mathbf{AQ} = \mathbf{b} \tag{4.6}$$

$$\text{where} \qquad a_{ij} = k_{X,ij} \sin \alpha_j + k_{R,ij} \cos \alpha_j \qquad \text{and} \qquad b_j = -U_\infty \sin \alpha_j$$

Provided that $m = n$, the the set of equations can be solved simultaneously using matrix inversion, as is shown in Equation 4.7. Alternatively, if $m > n$, the system of equations is overdetermined and linear regression can be used to find a best fit solution.

$$\mathbf{AQ} = \mathbf{b} \qquad \rightarrow \qquad \mathbf{Q} = \mathbf{A}^{-1} \mathbf{b} \tag{4.7}$$

Once the source segment strengths Q_i are known, the velocity at any given point outside of the body can be computed. This is done by summing the freestream velocity and the velocity contributions of all of the source segments which were given by Equations 4.1 and 4.2, as shown in Equation 4.8. Under the assumption that the flow is incompressible, the pressure coefficient can then be determined using Equation 4.9.

$$U = \sqrt{U_X^2 + U_R^2} = \sqrt{\left(\sum_{i=1}^n (k_{X,i} Q_i) + U_\infty \right)^2 + \left(\sum_{i=1}^n (k_{R,i} Q_i) \right)^2} \tag{4.8}$$

$$C_P = 1 - \left(\frac{U}{U_\infty} \right) \tag{4.9}$$

4.1.2. Model limitations

As was pointed out by Oberkampf [30], two conditions need to be met before the flow around a BOR can be modelled using this method:

1. The slope of the surface of the body must be continuous
2. The body must be relatively slender

While the first condition is well defined, the second one is vague. In practice it was found that the thicker the body becomes, the more difficult it is to obtain a realistic solution. As a result, two things should be checked: The occurrence of ripples in the pressure distribution and the location of stagnation points. A stagnation point should always be found at the leading edge and the trailing edge. In practice however, it is not possible to evaluate the velocity at the axis of symmetry, due to the radius in the denominator of Equations 4.1 and 4.2. It is therefore sufficient to see that the velocity is approaching zero. When using the equivalent body approach, a stagnation point is not expected to occur at the trailing edge.

4.1.3. Model discretization

A good discretization of the body geometry is also crucial for obtaining an accurate solution. The variables that need to be considered are the number of source segments n, the number of control points m and their distribution along the BOR.

The density of the discretization has an obvious impact on the accuracy of the solution. A denser discretization allows for a better resolution and a more accurate solution is therefore expected. In this particular case though, a second consideration has to be made, which has an even larger impact on the accuracy of the solution. The linear system of equations that needs to be solved often tends to be ill-conditioned. Oberkampf [30] already pointed out that this tends to be a problem when modelling BORs using source segments in potential flow.

A linear system is said to be ill-conditioned when it has a high condition number. The result of that is that a small change in input produces a large change in output. When the condition number is too high, numerical error can be magnified to the point where the solution obtained becomes useless. The condition number of matrix $\mathbf{A}$ is defined using Equation 4.10, where $\|\mathbf{A}\|$ is the norm of the matrix $\mathbf{A}$,

which can be computed as shown in Equation 4.11. Similarly, $\|\mathbf{A}^{-1}\|$ is the norm of the inverse of matrix $\mathbf{A}$.

$$\kappa(\mathbf{A}) = \|\mathbf{A}\|\|\mathbf{A}^{-1}\| \tag{4.10}$$

$$\|\mathbf{A}\| = \sqrt{\sum a_{ij}} \tag{4.11}$$

In practice, the effect of the condition number can also be monitored by checking the pressure coefficient at the leading edge, which should be equal to one. The pressure coefficient was observed to progressively diverge from this value as the problem gets increasingly ill-conditioned.

One of the first things that was observed to increase the condition number was the presence of a blunt leading edge or a blunt trailing edge. An effective way of dealing with this problem was however also found: As opposed to starting the source segment distribution right from the blunt leading or trailing edge, a small gap should be left between the edge of the body and the first (or last) source segment. A gap of a length of 1 to 5 times the length of the first source segment was found to work well, but should be adjusted for each body geometry for optimal results.

Taking this into account, the BOR surface is discretized into m panels, where each panel is a segment of a cone. The edges of the cone segments are specified by a list of $m + 1$ coordinates. The distribution of X coordinates can be linear, but a cosine distribution is preferred, as this allows the leading and trailing edges to be better defined. The cosine distribution is defined using Equation 4.12, where θ is a linear distribution of $m + 1$ points ranging from 0 to π and L is the length of the body. The first and last X coordinates define the leading and trailing edges respectively.

$$X = \left(\frac{1}{2} - \frac{1}{2}\cos\theta\right)L - L \tag{4.12}$$

At each X coordinate, the R coordinate is computed using a function that describes the geometry of the BOR. If the function is unknown and the body geometry is only specified by a list of coordinates, cubic spline interpolation is used to compute the radius at the desired X coordinates. To ensure a smooth surface contour, cubic spline interpolation is preferred over linear interpolation. Alternatively, the provided list of coordinates can be used directly. However, this limits the freedom of choosing the X coordinate distribution and the number of points and is therefore only possible if the given distribution is close to the desired one.

Once the coordinates describing the surface of the BOR are defined, the control points are distributed along the surface. A control point is placed in the center between each consecutive pair of the previously defined coordinate points. Additionally, the body surface angle at each control point is also computed based on the two neighboring coordinate points.

The final step of the discretization is to determine the X coordinates and the lengths l of the source segments. Since the source segments must lie on the axis of symmetry, their location can be described by the x-coordinate of the panel center. In order for the flow field to be as smooth as possible, it makes sense to use the same kind of X coordinate spacing as was used to define the outer BOR geometry. This way, the ratio of control points to source segments is also maintained locally. A scaling function is therefore used on Equation 4.12 to take the leading edge and trailing edge gaps ΔX_{LE} and ΔX_{TE} into account, which results in Equation 4.13. This time, θ is a linear distribution of $n + 1$ points ranging from 0 to π. The resulting distribution of points mark the edges of the source segments.

$$X = \left[\left(\frac{1}{2} - \frac{1}{2}\cos\theta\right)L - L\right]\frac{L - \Delta X_{LE} - \Delta X_{TE}}{l} - \Delta X_{TE} \tag{4.13}$$

Choosing m and n correctly is important from several points of view. Increasing these two parameters increases the resolution of the discretization and a more accurate solution should therefore be obtained. However, increasing m and n also increases the computational cost and a trade-off therefore has to be made between accuracy and computational time. Further, the problem still becomes increasingly ill-conditioned with the increasing m and n. For the example of modelling a sphere it becomes impossible to get a realistic solution once $m = n > 25$. It was found however, that this problem can be solved by simply increasing the number of control points m such that $m > n$. The system of equations is then solved using linear regression to find a best fit solution. Using $100 \leq m \leq 200$, which

is considered to be a good compromise between accuracy and computational cost, it was found that a ratio of 10 control points to 9 source segments keeps the solution sufficiently stable.

A sketch showing the principles of discretization that have been discussed in this section is shown in Figure 4.3. The source segments and control points are distribution using a cosine spacing along the X axis. Because the body has a blunt leading edge, a small gap was left between the edge of the body and the point where the source segment distribution starts. In order to stabilize the solution, the number of control points is larger than the number of source segments.
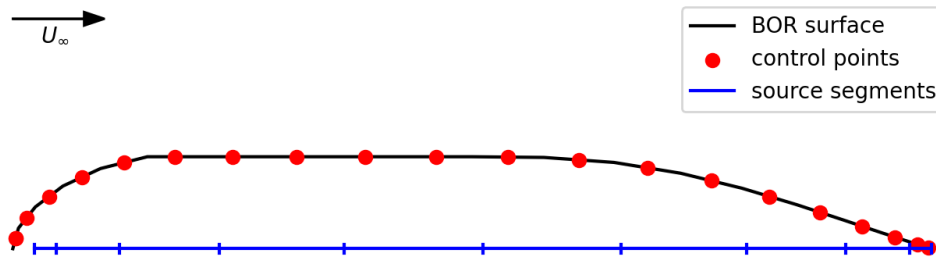

Figure 4.3: A sketch showing the discretization of the BOR based on the principles discussed in this section. Note that the number of control points and source segments is low for illustration purposes. In practice, at least 100 source segments should be used. The ratio of control points to source segments has also been exaggerated.

Additionally, an alternative way of dealing with high condition numbers of the linear system was also investigated. The condition number can be reduced by using Thikonov regularization [31] while keeping $m = n$. This method works by adding the identity matrix multiplied by a small regularization constant to the matrix **A**. While Thikonov regularization was also found to work, it introduces regularization error. Solving an overdetermined linear system using least square regression is therefore preferred.

4.1.4. Validation
The validation of the BOR potential flow model was performed by computing the pressure distribution around two BORs, both modelled using 180 source segments and 200 control points. The first body is a slender streamline BOR. Shown in Figure 4.4, the results are compared with those of Kaplan [32], who computed the pressure distribution around the same BOR by solving the Laplace's equation using a power series expansion. As ban be seen, the computed results agree with the validation data very well.
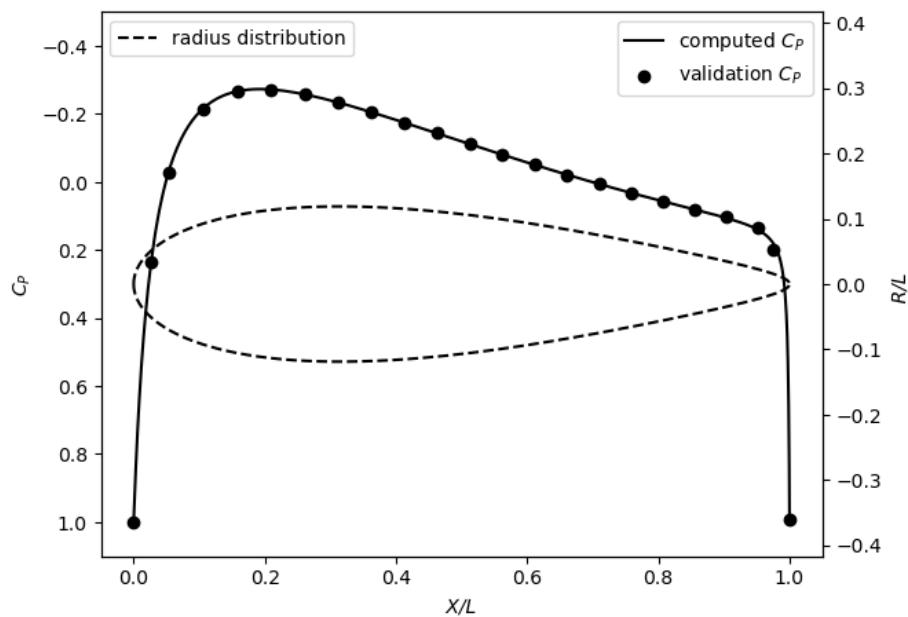

Figure 4.4: Comparison of the computed pressure distribution around a BOR with the results of Kapalan [32].

The second body that was investigated is a sphere and the computed pressure distribution is compared to the analytical solution in Figure 4.5. Equation 4.14, which was derived by Muhammad [33], gives the flow velocity along the surface of a sphere in potential flow. Here, θ is the angle between the point on the surface of the sphere and the X axis, hence, $\sin\theta = R/R_s$, where R_s is the radius of the sphere. As can be seen, the computed pressure distribution agrees very well with the validation results in this case as well.
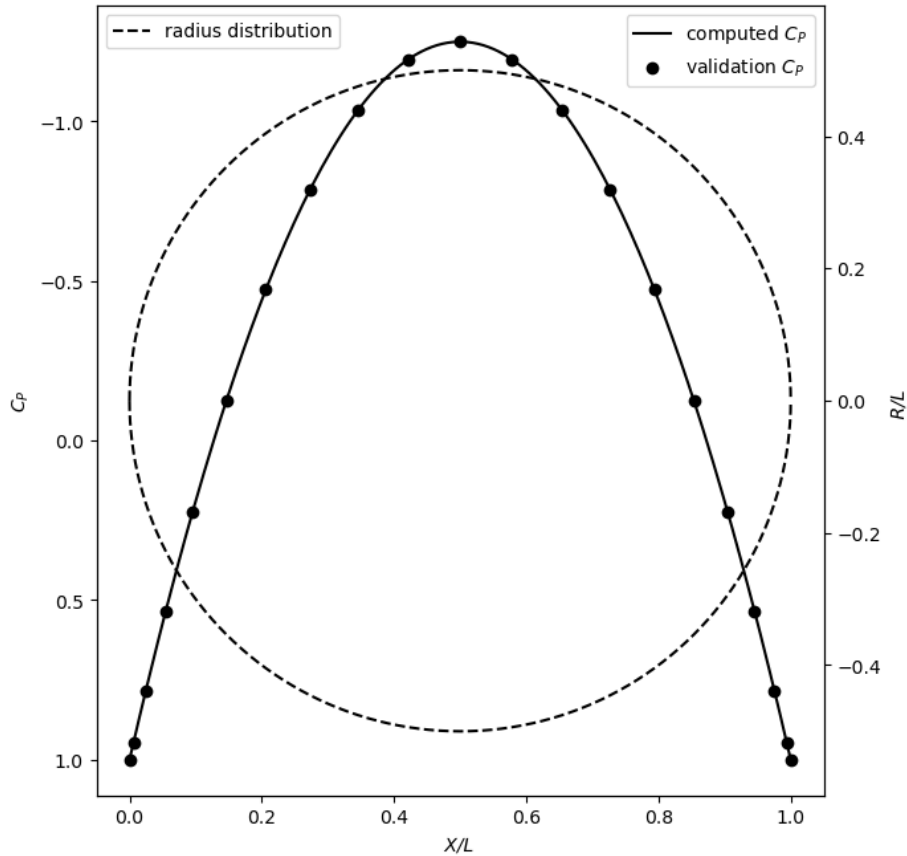

Figure 4.5: Comparison of the computed pressure distribution around a sphere with the exact solution.

$$U = 1.5 U_\infty \sin\theta \tag{4.14}$$

4.2. Boundary layer models

The boundary layer is computed using a laminar and a turbulent boundary layer model, with the BOR geometry and the flow velocity at the boundary layer edge U_e as input. Since the boundary thickness is initially unknown, the surface velocity distribution is used as input in the first iteration.

4.2.1. The axisymmetric boundary layer

Among the most important parameters describing a boundary layer are the boundary layer thickness, the displacement thickness and the momentum thickness. Defining them for axisymmetric flow is however, more challenging than for the two dimensional case and several definitions exist. A summary of the various definitions will therefore be provided. [34]

The boundary layer thickness δ is usually defined as the distance normal to the surface, where the the local velocity $U = 0.995 U_\infty$. For a thick boundary layer, this definition is however not suitable, as the static pressure across may not be constant. The alternative definition of δ that is used for thick boundary layers is the location where the total pressure is equal to 0.99 times the freestream value.

For cases when the static pressure does not vary across the boundary layer, this definition reduces to the one mentioned previously.

For axisymmetric flow, the displacement thickness δ_1 and the momentum thickness δ_2 are often defined as shown in Equations 4.15 and 4.16. While these definitions are not physical, they enable the momentum equation to be written in a much simpler way.

$$\delta_1 = \int_0^\delta \left(1 - \frac{U}{U_e}\right) \frac{R}{R_0} dy \tag{4.15}$$

$$\delta_2 = \int_0^\delta \frac{U}{U_e} \left(1 - \frac{U}{U_e}\right) \frac{R}{R_0} dy \tag{4.16}$$

The standard planar definitions given by Equations 4.17 and 4.18 are also used within this axisymmetric boundary layer model, as converting to them allows the use of standard two dimensional velocity distribution models.

$$\bar{\delta}_1 = \int_0^\delta \left(1 - \frac{U}{U_e}\right) dy \tag{4.17}$$

$$\bar{\delta}_2 = \int_0^\delta \frac{U}{U_e} \left(1 - \frac{U}{U_e}\right) dy \tag{4.18}$$

The definition of the physical displacement thickness δ_1^*, is the distance by which the streamlines outside of the boundary layer are displaced due to the presence of it. On the other hand, the physical momentum thickness δ_2^* is closely related to the drag of the body. It represents the thickness of a layer of inviscid flow around the body, whose momentum is equal to the momentum deficit of the boundary layer. The physical quantities δ_1^* and δ_2^* can be computed by solving Equations 4.19 and 4.20.

$$\delta_1 = \delta_1^* \left(1 + \frac{1}{2} \frac{\delta_1^*}{R_0} \cos \phi\right) \tag{4.19}$$

$$\delta_2 = \delta_2^* \left(1 + \frac{1}{2} \frac{\delta_2^*}{R_0} \cos \phi\right) \tag{4.20}$$

4.2.2. Boundary layer discretization

Since the boundary layer models work by numerically integrating various equations along the BOR, it is necessary to define a step size, or locations that will mark the edge of each step. The BOR has already been discretized into m cone segment panels. However, with m in the range of 100 to 200, this discretization is too sparse for the boundary layer models to provide a converged solution[2]. Making use of the existing discretization, each panel is split into a number of segments N_{BL}. The coordinates defining this denser discretization are computed using cubic spline interpolation in order to make sure that the angle of the body surface changes continuously. For the calculations performed throughout this thesis, an $N_{BL} = 10$ was used. The boundary layer transition is defined to occur after the first step which crosses the prescribed transition point X_{tr}/L.

The method of evaluating U_e was also found to be important. At each step of the boundary layer integration, the flow velocity needs to be evaluated at the boundary layer thickness measured perpendicular to the surface of the BOR. The easiest way of doing this, is to compute the coordinates of this location at each step and use the potential flow solution to compute the corresponding U_e. While this method was found to work most of the time, it occasionally caused instabilities in the combined equivalent body model.

In the potential flow model, the impermeable surface condition is only satisfied at the control points. While the flow is likely to be near parallel to the body contour at all locations (provided that the surface is smooth, streamlined and well discretized) small ripples in the velocity distribution may be present in between control points. In the areas where the boundary layer is thin, these ripples may even be found at the boundary layer edge, where U_e is being evaluated. Because of the iterative nature of the

---

[2]A solution that no longer changes to the desired number of significant figures. During this work, a solution is considered to be sufficiently converged when the first 4 numbers stop changing.

equivalent body approach, the ripples in the velocity distribution were occasionally observed to grow and caused the boundary layer thickness to diverge.

To solve this problem, the velocity is only evaluated at the locations directly above the control points. Interpolation is then used to estimate the velocity in between. Since there are already $N_{BL}/2$ integration steps before the first control point, U_e at the leading edge is assumed to be zero for an additional interpolation point. For the last $N_{BL}/2$ steps that are behind the last control point, U_e is computed by extrapolation using the last two control points. An added benefit of this approach is a decrease in computational cost, as evaluating the velocity at many different locations using the potential flow model is relatively expensive.

4.2.3. The laminar boundary layer model

The development of the laminar boundary layer until the prescribed transition point is computed using the laminar boundary layer model that was proposed by Rott [35]. Since the boundary layer is assumed to be thin, no distinction is made between the planar, axisymmetric and actual displacement and momentum thicknesses. The momentum thickness δ_2 is integrated using Equation 4.21, where ν is the kinematic viscosity, $a = 0.47$, $b = 6.28$ and U_e is the velocity at the edge of the boundary layer. The integration starts from the stagnation point where $x = 0$ and continues along the surface of the body.

$$\delta_2^2 = a\nu R^{-2}U_e^{-b} \int_0^x R^2 U_e^{b-1} dx \tag{4.21}$$

The growth parameter G is defined as a linear relationship using Equation 4.22, from which follows that for $b = 6.28$ the shape parameter H is constant and equal to 1.14.

$$G = a + bm = 2l + 2(H + 2)m \tag{4.22}$$

The wall shear stress τ is given by Equation 4.23, where $\mu = \nu\rho$ is the dynamic viscosity and from Equation 4.22 follows that $l = a/2$.

$$\tau = \frac{\mu U_e l}{\delta_2} \tag{4.23}$$

4.2.4. The turbulent boundary layer model

Past the prescribed transition point, the development of the boundary layer is computed using the thick turbulent axisymmetric boundary layer model proposed by Patel [27]. The model is based on an approximate form of the momentum integral equation, a skin friction relation deduced from a two-parameter boundary layer profile shape and a modified version of the entrainment equation proposed by Head [36]. The model functions by integrating these parameters over the surface of the body and in each integration step a total of 14 equations have to be solved iteratively.

The model is suitable for situations when the boundary layer thickness is not small with respect to the transverse radius of curvature of the surface. On the other hand, it is assumed that the boundary layer thickness is much smaller than the longitudinal radius of curvature of the surface. Patel has demonstrated that the model is capable of predicting the development of the boundary layer over the aft cone of a fuselage like body with reasonable accuracy.

Integration of the turbulent boundary layer starts at the prescribed transition location and is initialized using the momentum thickness δ_2 and the shape parameter H, both predicted by the laminar boundary layer model. The outputs of the model are the boundary layer thickness δ, the displacement and momentum thicknesses δ_1 and δ_2, the shape parameter H and the skin friction coefficient C_f. The model uses a one parameter velocity profile and the velocity U can be computed at any point within the boundary layer using Equation 4.24.

$$\frac{U}{U_e} = \left(\frac{y}{\delta}\right)^{\frac{1}{2}(\bar{H}-1)} \tag{4.24}$$

In order to check that the model was implemented correctly, computations were compared with the results published by Patel [27]. Because the model was implemented without any modifications, the results are included in Appendix A.

4.3. The equivalent body model

The Potential flow model and the boundary layer models are combined using the equivalent body approach. An equivalent body is formed by extending the surface of the BOR by the displacement thickness of the boundary layer, in the direction normal to the BOR surface. By solving the potential flow field around the equivalent body, the displacing effect of the boundary layer due to the loss of momentum is taken into account. As a result, the flow velocity can be accurately evaluated at the boundary layer edge and outside of the boundary layer using potential flow [37]. On the other hand, the flow velocity within the boundary layer is given by the boundary layer model.

In practice, the equivalent body is formed by simply moving the BOR control points. After displacing them, the flow angle condition also needs to be adjusted, as the flow needs to be parallel to the equivalent body. The angle at each control point is assumed to be the angle of the line connecting the upstream and downstream control points. At the last control point the angle of the line connecting the last and the second last control point is used instead. The flow angle of the first control point is assumed to remain unchanged as the displacement thickness over the leading edge is negligibly thin. The iterative procedure for solving the equivalent body problem can be summarized as follows:

The equivalent body iterative procedure
Initialization:

- Assume that the boundary layer thickness is zero

Iteration (repeat until δ_1 converges):

1. Compute the source segment strengths of the potential flow model by solving Equation 4.6
2. Evaluate U_e, the velocity distribution along the boundary layer edge using potential flow
3. Using U_e as input, compute the boundary layer properties along the surface of the BOR
4. Adjust the equivalent body by repositioning the control points using the new displacement thickness

The equivalent body model was observed to converge quickly, especially when compared to the actuator disc model that will be discussed later. Doing ten iterations was found to be more than sufficient for obtaining a solution that is converged to six or more significant figures. More attention was not given to the stopping criteria of this iterative procedure, as it will later be combined with the actuator disc model.

During the first iteration when U_e is assumed to be the velocity distribution along the surface of the body, pressure recovery occurs near the trailing edge. This causes a rapid decrease in velocity and the predicted boundary layer thickness may start to diverge. In order to establish initial convergence, the growth of the boundary layer is therefore limited. In practice a condition is imposed that if the R coordinate of the boundary layer edge starts to increase over the aft cone, it is forced to remain constant downstream of this point during the first iteration.

4.3.1. Intermediate validation

At this stage of the work, the basic functioning of the equivalent body model can be validated by comparing predicted boundary layer properties to other computational and experimental results.

First of all, results will be compared to the computational data from the ESDU item 79020 [28]. In this work, the boundary layer was also predicted using an equivalent body model that combines potential flow with a boundary layer model. Three bodies with distinctly different aft cone geometries were selected. The functions describing the body geometries can be found in the ESDU item [38].

As can be seen in Figures 4.6 to 4.8, the computed overall, displacement and momentum thicknesses agree fairly well with the computational data, with the ESDU thicknesses being consistently slightly higher. Potential reason for the discrepancies observed can be the fact that the ESDU used a different boundary layer model to obtain their results. Error was likely also introduced when reading the validation data from graphs. The small deviations in the momentum thickness that can be observed at the trailing edge of the bodies are the result of a division by radius which takes place when solving Equations 4.19 and 4.20.

Validation was also performed by comparing computed results with CFD and experimental results measured by Della Corte [25] at Delft University of Technology. The results are presented in Figure 4.9. Fair agreement can be observed in this comparison as well.
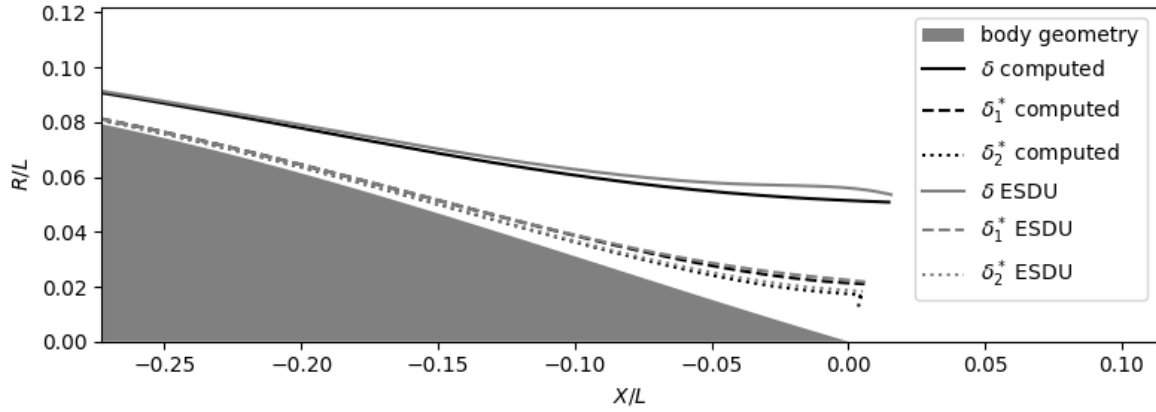
Figure 4.6: ESDU body 1 with a linear aft cone geometry. Comparison of computed boundary layer data with that obtained by ESDU.

Figure 4.7: ESDU body 4 with a convex aft cone geometry. Comparison of computed boundary layer data with that obtained by ESDU.

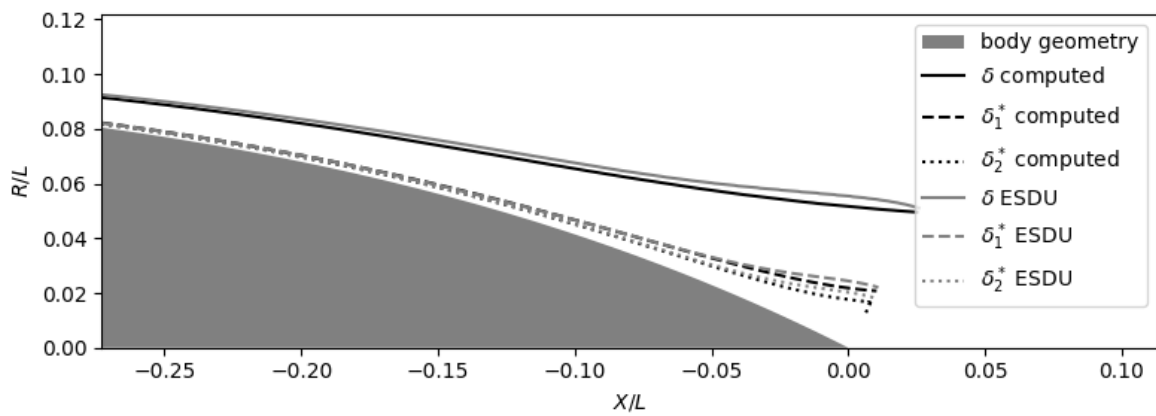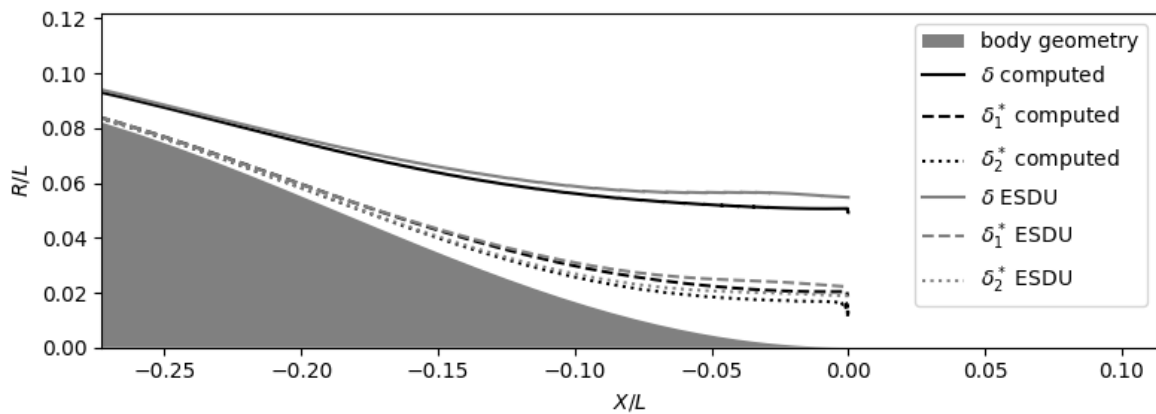**Figure 4.8:** ESDU body 5 with a concave aft cone geometry. Comparison of computed boundary layer data with that obtained by ESDU.

4.4. Surface pressure and drag computation

Although the assumption of constant static pressure within the boundary layer holds true for most lifting surfaces, experimental results have shown that this assumption is not valid for a thick axisymmetric
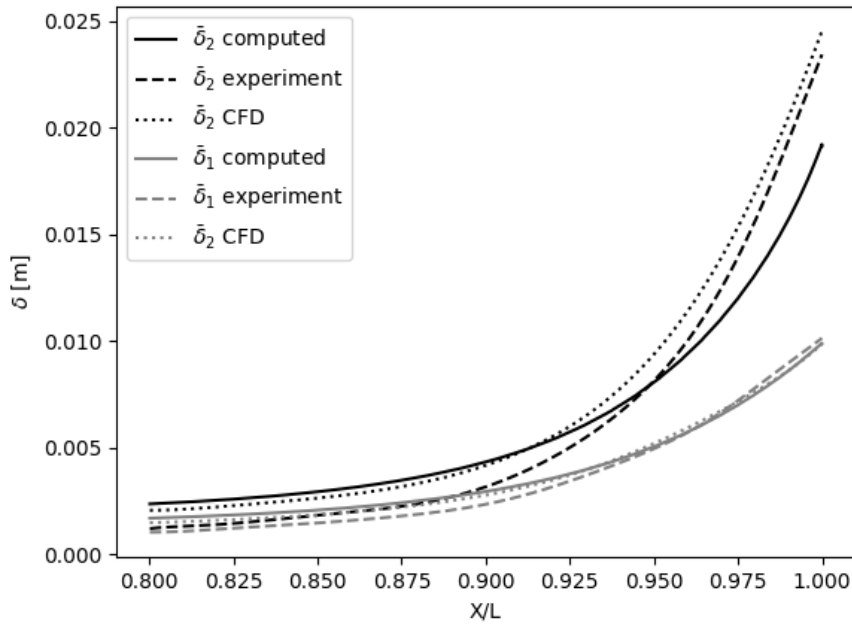
Figure 4.9: Comparison of computed boundary layer data with experimental and CFD results of Della Corte [25]

boundary layer in the region of the tail cone of a BOR [24]. As was noted by Korttkov [39], when a boundary layer travels along a longitudinally curved surface, it must experience a centripetal force. As a result a pressure difference must exist between the surface and the edge of the boundary layer and when the boundary layer becomes thick this pressure difference can no longer be neglected. Following this observation, a derivation was made to quantify this difference in pressure.

Suppose an infinitesimal volume of fluid with dimensions dx and dy that spans an azimuthal angle arc $d\psi$ around the axis of symmetry is located within the boundary layer at the coordinates (x, y), as shown in Figure 4.10. Because of its small size, the volume is assumed to be a cuboid and its mass m is equal to the air density ρ multiplied by its volume, as is shown in Equation 4.25.
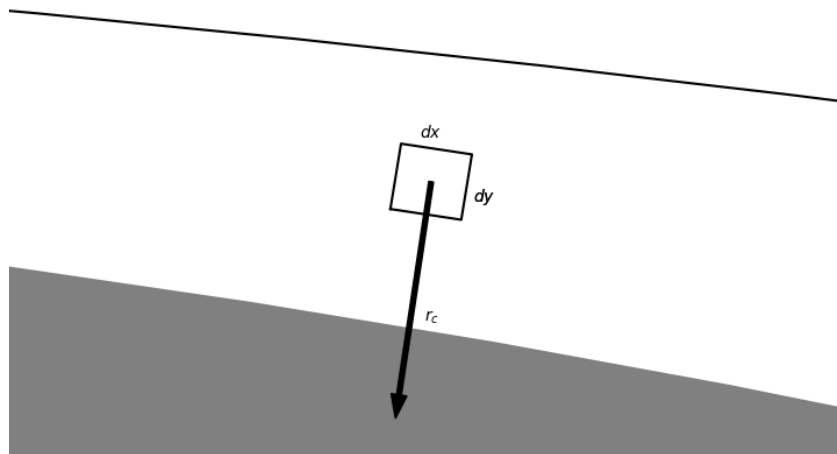

Figure 4.10: The infinitesimal volume of fluid used in the derivations represented in two dimensions, not to scale. The BOR is shown as a gray solid and the boundary layer edge is marked with a black line.

$$m = \rho \cdot dx \cdot dy \cdot Rd\psi \qquad (4.25)$$

The centripetal force F_c experienced by the fluid volume is given by the well known expression from classical mechanics shown in Equation 4.26, where U is the fluid velocity and r_c is the radius of curvature. Meanwhile, the centripetal force must also equal to the infinitesimal difference in pressure across the fluid volume $d\Delta p$ multiplied by its cross sectional area in the direction normal to the radius of curvature, as shown in Equation 4.27.

$$F_c = \frac{mU^2}{r_c} = \frac{\rho \cdot dx \cdot dy \cdot Rd\psi \cdot U^2}{r_c} \tag{4.26}$$

$$F_c = d\Delta p \cdot dx \cdot Rd\psi \tag{4.27}$$

Combining Equations 4.26 and 4.27 and solving for the difference in pressure dp results in Equation 4.28. The total pressure difference across the boundary layer Δp can then be obtained by integrating both sides of the equation as shown in Equation 4.29. Note that both U and r_c are functions of x and y. While the local flow velocity U can be easily defined using Equation 4.24, defining r_c is slightly more challenging.

$$d\Delta p = \frac{\rho \cdot dy \cdot U^2}{r_c} \tag{4.28}$$

$$\Delta p = \int_0^\delta \frac{\rho U^2}{r_c} dy \tag{4.29}$$

Computing the radius of curvature r_c based on neighboring points that define the curved surface can be done with the help of Figure 4.11. The first step is to define the half was points between the points that define the surface. An arc of a circle is then placed between the half way points such that it is tangent to the surface at both of its ends. The radius of curvature can then be computed using Equation 4.30, where d is the distance between the half way points and $\Delta\alpha$ is the difference in angle of the consecutive surface panel segments.
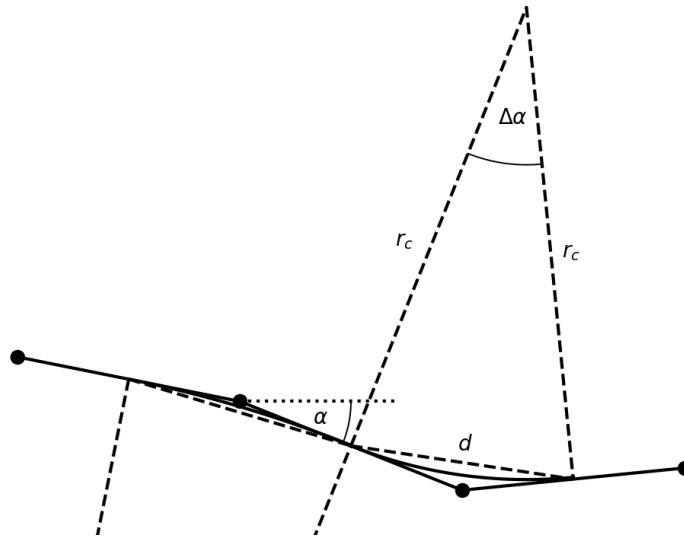
$$r_c = \frac{d/2}{\sin(\Delta\alpha/2)} \tag{4.30}$$

Figure 4.11: Sketch showing the geometry construction required for computing the radius of curvature r_c.

4.4.1. Surface pressure based on the surface curvature correction

The most straight forward way to define the local radius of curvature of the flow r_c, is by neglecting the growth of the boundary layer and assuming that the flow uniformly curves together with the BOR. This means that the center of curvature for all y at a given x coordinate coincides with the center of curvature of the surface. As a result the radius of curvature becomes defined as $r_c = r_{c,s} + y$, where $r_{c,s}$ is the radius of curvature of the surface.

4.4.2. Surface pressure based on the flow curvature correction

A more rigorous way of defining r_c, is by computing the streamlines of the flow within the boundary layer using mass flow conservation. This allows r_c to be defined locally at any height above the surface.

Starting from the trailing edge, the boundary layer is discretized along the y axis into N_{st} uniformly distributed stream tubes. Throughout this thesis an $N_{st} = 50$ was used, unless stated otherwise. Using the boundary layer velocity profile, the mass flow of each stream tube $\dot{m}_{i_{st}}$ is computed using Equation 4.31.

$$\dot{m}_{i_{st}} = \rho A_{i_{st}} U_{i_{st}} \tag{4.31}$$

The stream tube cross sectional area $A_{i_{st}}$ is the area of a cone segment and is therefore computed using Equation 4.34. The flow velocity $U_{i_{st}}$ through the cross section is assumed to be constant and is evaluated at the average y coordinate using Equation 4.24. In order to avoid iteration, the flow angle is not considered when computing the mass flow. This is considered acceptable as the flow angle is neglected within the boundary layer model itself.

Once the mass flow of the stream tubes is known, their development can be computed in the upstream direction. The radii of the stream tubes at each upstream location are computed using the local velocity profile, such that the mass flow of each stream tube is conserved. In order to save computational time, the streamlines are evaluated at a lower resolution, at the x coordinates of the BOR control points.

The problem that arises when when computing the streamtube development is that the mass flow is computed by integrating the velocity profile, and y, the place at which the integration needs to stop is the unknown quantity. In order to solve this problem efficiently and without iteration, an interpolation function is defined at each upstream location. This function gives the y coordinate as a function of the cumulative mass flow from $y = 0$. The interpolation function is defined by evaluating the mass flow between N_{st} equidistantly spaced points between the body surface and the boundary layer edge. Use is made of the same procedure that was initially used for evaluating the mass flow of the stream tubes at the trailing edge. Starting from the surface, the radii of the stream tubes are then then computed using their cumulative mass flow. Moving upstream, the process is stopped once the point where $X/L \leq -0.5$ is reached. Upstream of this point the boundary layer is assumed to be thin and applying the pressure correction is therefore unnecessary.

An example of the streamlines computed using this method is shown in Figure 4.12. As can be seen the curvature of the streamlines near the trailing edge is very different to the curvature of the surface. While the surface in this region is turning towards the axis of symmetry, most of the flow is turning away from it. This highlights the need to compute the radius of curvature of the flow locally. Flow entrainment into the boundary layer can also be observed, as the outermost streamlines at the trailing edge gradually exit the boundary layer when moving upstream.

4.4.3. The flow orthogonal integration path

When deriving Equation 4.29 for evaluating the difference in pressure across the boundary layer it was assumed that the centripetal force acting on a fluid volume is acting in the direction normal to the surface. However, in reality, the centripetal force acts in the direction of the radius of curvature, which is always perpendicular to the local streamlines. Looking at the streamlines near the trailing edge of the body in Figure 4.12, it is evident that the flow is far from parallel to the body surface.

In order to deal with this problem and eliminate any inaccuracies that may result from it, the integration path must be changed. Instead of integrating along a straight line perpendicular to the surface, the integration should be carried out along a curved path perpendicular to the streamlines. An example comparing the new and old integration paths is shown in Figure 4.13.
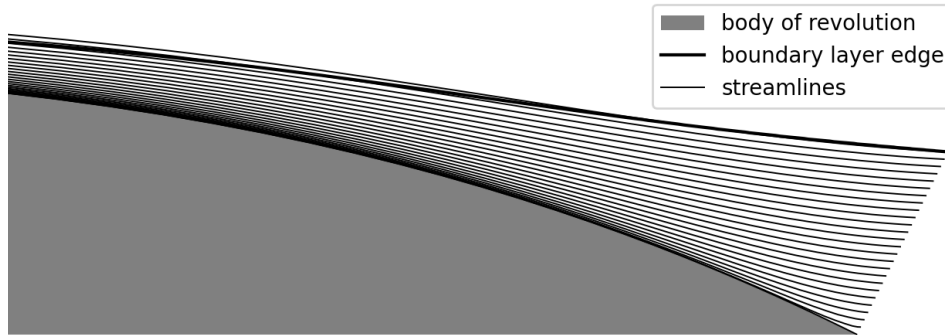
Figure 4.12: An example of streamlines within the boundary layer computed using $N_{st} = 50$, but showing only every second streamline for clarity.
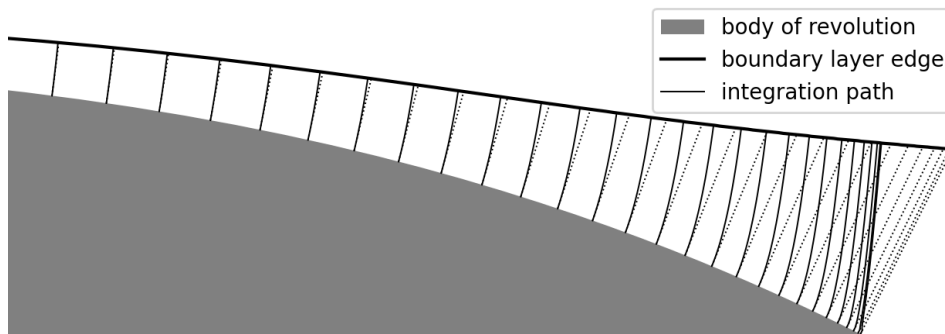

Figure 4.13: An example of an integration path perpendicular to the flow. The integration path perpendicular to the surface is shown with the dotted line.

After changing the integration path, the surface pressure is now also computed using the boundary layer edge pressure at another location. The difference in pressure across the boundary layer is now given by Equation 4.32, where s is the new integration path starting from the surface of the body. The integration stops when the edge of the boundary layer is reached.

$$\Delta p = \int_0^S \frac{\rho U^2}{r_c} ds \qquad (4.32)$$

Performing this integration does however come with a problem and that is the fact that U, r_c and the flow angle α which is required for computing the integration path itself, are only defined at a grid of discrete locations (the points that define the stream tubes). Two dimensional linear interpolation is therefore used to evaluate all of the required parameters at any point within the boundary layer. The linear interpolation uses the three data points that define the smallest possible triangle around the point of interest.

4.4.4. Drag computation

Because the flow is assumed to be incompressible and axially symmetric, the compressibility drag and the induced drag are neglected. The drag of the body is therefore made up of only two components, the viscous drag and the pressure drag.

The viscous drag is computed by numerically integrating the wall shear stress τ computed using the boundary layer models along the surface of the body in the direction parallel to the flow using Equation 4.33. In this case, the subscript i denotes consecutive cone segment surface panels of the boundary layer discretization with each panel having the surface area A_i. As τ acts in the direction parallel to the body surface, the expression is multiplied by the cosine of the surface angle α_i. The surface area of a cone segment is given by Equation 4.34, with l_i being the length along the surface and r_1 and r_2 being the edge radii. Since the wall shear stress is only defined at the edges of each panel, τ_i is assumed to be the average of the wall shear stress at the edges of each panel.

$$D_v = \sum_{i=1}^{mN_{BL}} \tau_i A_i \cos \alpha_i \tag{4.33}$$

$$A_i = \pi l_i (r_1 + r_2) \tag{4.34}$$

The pressure drag is computed in a similar way, this time the surface pressure p_s is numerically integrated along the surface of the body in the direction parallel to the flow using Equation 4.35. This time the expression is multiplied by the sine of the surface angle α_i, as static pressure acts in the direction normal to the surface. The minus sign comes from the fact that α_i was defined clockwise positive. Because the static pressure along the surface is evaluated at a lower resolution, linear interpolation or extrapolation is used to determine the surface pressure at the denser boundary layer surface discretization.

$$D_p = \sum_{i=1}^{mN_B L} -p_{s,i} A_i \sin \alpha_i \tag{4.35}$$

The drag of the BOR can be non denationalized by turning it into a drag coefficient C_D. The drag coefficient of a BOR is given by Equation 4.36, where R_b is the maximum radius of the body.

$$C_D = \frac{2D}{\rho U_\infty^2 \pi R_b^2} \tag{4.36}$$

4.5. Validation of the BOR mode

In order to check that the equivalent body model is working as intended, validation will be performed using both CFD and experimental results. The effect of computing the surface pressure using the different methods described in section 4.4 will also be analyzed. To avoid long descriptions, the methods will from now on be referred as following, where the first word designates the curvature used for computing the correction and the second word designates the integration path.

- **Uncorrected-surface:** Surface pressure is assumed to be equal to the boundary layer edge pressure, taking the path normal to the surface.
- **Uncorrected-flow:** Surface pressure is assumed to be equal to the boundary layer edge pressure, taking the path normal to the local flow.
- **Surface-surface:** Corrected pressure based on surface curvature, integrated in the direction perpendicular to the surface.
- **Flow-surface:** Corrected pressure based on local flow curvature, integrated in the direction perpendicular to the surface.
- **Flow-flow:** Corrected pressure based on local flow curvature, integrated in the direction perpendicular to the local flow.

While a surface-flow correction would be possible as well, doing so makes little sense. When the integration is performed the direction normal to the flow, it is no more difficult to apply the correction based on local flow curvature as well. The same can be said about the uncorrected-flow method, but this one is considered interesting for investigating the isolated effect of changing the integration path only. On the other hand, the flow-surface method is interesting because correcting with respect to the flow direction adds a lot of accuracy but is still considerably easier to implement than the flow-flow method.

4.5.1. Analysis and validation using CFD data

Validation of the equivalent body model is performed by comparing the computed drag coefficient of the body shown in Figure 4.14 with the results obtained by Lv [40]. The reason for choosing this set of data is that powered configurations were also simulated using an actuator disc placed at the trailing edge of the body. This will come in useful for validating the entire model later during this work.

The non-dimensional parameters defining the flow condition are summarized in Table 4.1. Due to the limitations of the equivalent body model, compressibility effects are not taken into account. However,
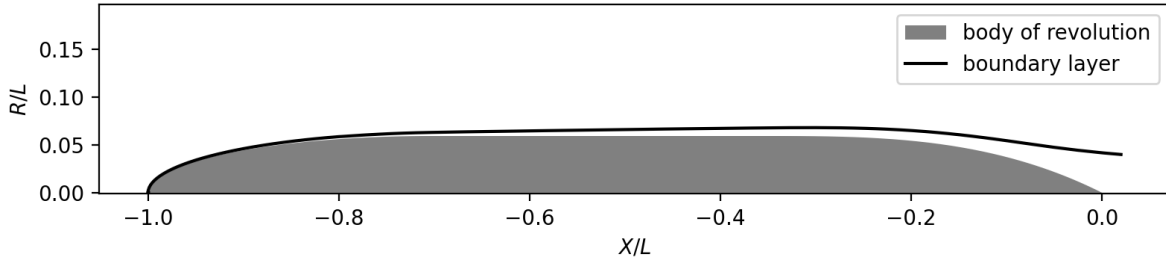
Figure 4.14: The BOR geometry used in the simulations performed by Lv [40]. The boundary layer edge was plotted according to the results of the equivalent body model.

this should not cause large discrepancies as the Mach number used by Lv is quite low. Aditionally, since the location of the boundary layer transition in the work of Lv is unknown, it was set to occur at X_{trans}/L = 0.2. The effects of making this assumption are also assumed to be minimal. The model settings used for obtaining the results presented in this section are listed in Table 4.2.

Table 4.1: Non-dimensional parameters describing the flow condition.

	CFD	present work
Re	2.37×10^6	
M	0.08	0
X_{trans}/L	unknown	0.2

Table 4.2: Model settings used for computing the results used for validation.

number of sources	90
number of control points	100
number of boundary layer elements	1000
number of stream tubes	50

Before proceeding to the comparison of results with the ones obtained by Lv, the suitability of the various methods for computing surface pressure was analyzed. The pressure coefficient distribution around the BOR was evaluated and the results are presented in Figure 4.15.

The first observation that can be made from Figure 4.15 left is that correcting the pressure using any of the methods only makes a noticeable difference in the tail cone region, where the boundary layer is thick. Over the rest of the body, the effect of a pressure correction is negligible. Secondly it can be observed that using the surface-surface method, which is based on the surface curvature of the body, the predicted C_P is always lower. This makes sense as the body is convex over the entire tail cone and lower pressure on the surface is therefore required to overcome the adverse pressure gradient.

Next, it can be observed that the flow-surface and flow-flow methods result in a similar correction to the surface-surface method over the first half over tail cone. On the other hand, the results differ drastically over the second half and the correcting effect even changes direction. This can be understood by looking at Figure 4.12. As can be seen, the flow curves together with the body surface initially, but starts to gradually curve away from it over the second half of the tail cone.

The last observation that can be made is that changing the integration path across the boundary layer does not make a significant difference in the surface pressure for this particular geometry. The difference between the flow-surface and flow-flow methods is barely noticeable, except in the trailing edge. To analyze the isolated effect of changing the integration path, the uncorrected-surface and uncorrected-flow methods are compared in the trailing edge region in Figure 4.15 right. As can be seen, correcting the integration path results in the pressure distribution being stretched to the right. This makes sense as the pressure at the edge of the boundary layer is being sampled further upstream, as can be seen from Figure 4.13, which shows the corresponding integration paths. Unfortunately, the computed C_P distributions cannot be compared with the work of Lv, as those were not published.
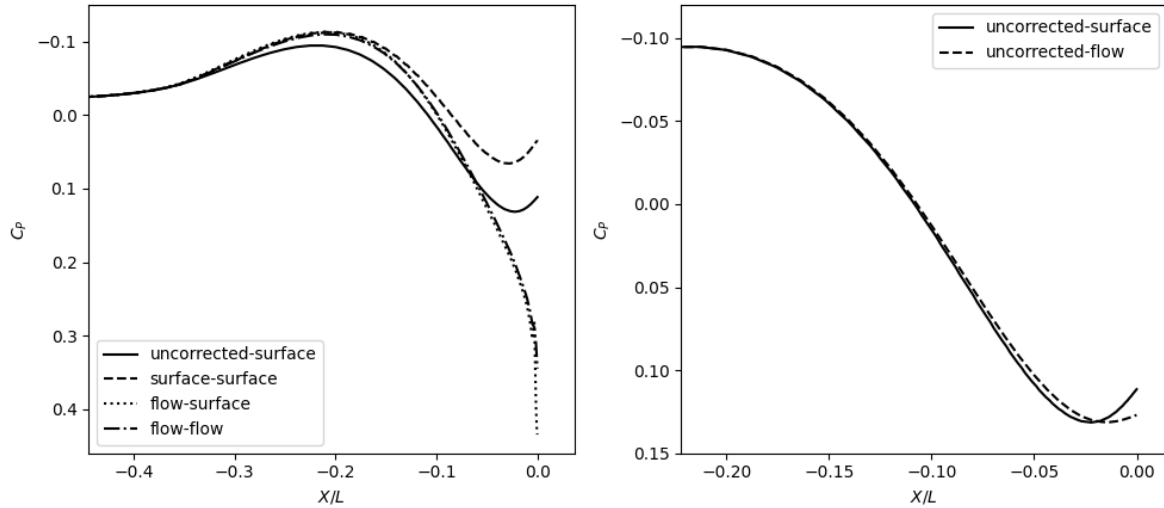
Figure 4.15: Pressure coefficient over the surface of the tail cone computed using four different methods. Because of the small difference between the uncorrected-surface and the uncorrected flow methods, they are compared separately in the figure on right, which is enlarged to show the trailing edge region only. The rest of the methods are compared in the figure on the left.

Proceeding to validation using the results of Lv, the pressure drag coefficient C_{D_p} and the viscous drag coefficient C_{D_v} were computed using the various methods and are compared with the CFD results in Table 4.3.

Table 4.3: Drag coefficients of the BOR computed using the various pressure correcting methods compared to the CFD results of Lv [40]. The ΔC_{D_p}, ΔC_{D_v} and ΔC_{D_t} give the percentage difference of the respective variables to the ones computed using CFD.

	C_{D_p}	ΔC_{D_p}	C_{D_v}	ΔC_{D_v}	C_{D_t}	ΔC_{D_t}
CFD	0.0292		0.1213		0.1505	
uncorrected-surface	0.0097	-66.7 %	0.1034	-14.8 %	0.1132	-24.8 %
uncorrected-flow	0.0125	-57.2 %	0.1034	-14.8 %	0.1159	-23.0 %
surface-surface	0.0398	36.3 %	0.1034	-14.8 %	0.1432	-4.9 %
flow-surface	0.0150	-48.6 %	0.1034	-14.8 %	0.1184	-21.3 %
flow-flow	0.0172	-41.1 %	0.1034	-14.8 %	0.1207	-19.8 %

As can be seen, the viscous drag coefficient, C_{D_v} is not effected by applying pressure corrections and an error of -14.8 % is observed. On the other hand, the pressure drag coefficient C_{D_p}, varies drastically between the different pressure computing methods. The pressure drag computed using the uncorrected pressure distribution is significantly underestimated. On the other hand, applying the surface-surface method results in an overestimate of C_{D_p}. Both of these findings are expected based on the previous discussions. Computing pressure using the flow-surface and flow-flow methods results in a C_{D_p} prediction in between the uncorrected and the results obtained using the surface-surface method.

Unfortunately, as can be seen from Table 4.3, the results from this work do not agree very well with the CFD results of Lv, especially the prediction of the pressure drag. However, since the CFD results have also not been validated, it is not possible to determine the cause of the observed discrepancies. Several observations can however be made from the analysis that was carried out in this section:

- The pressure distributions computed using the various methods are qualitatively in line with what is expected based on the theory behind each method.
- The computed drag coefficients are qualitatively in line with what is expected based on the pressure distributions.
- Because of the large difference in pressure drag computed using the different methods, it can be concluded that taking the pressure variations across the boundary layer into account is important and the flow-flow method should in theory provide the best results.

4.5.2. Analysis and validation using experimental data

In order to further validate the computational model, results were also compared with experimental data that was gathered by van Sluis [41]. The experiment was carried out in the Low Turbulence Tunnel (LTT) facility at Delft University of Technology. A BOR with a length of 1.83 m was tested in a flow velocity of 60 m/s, with and without a propeller located near the trailing edge.

The net force acting on the body was measured and the static pressure distribution was sampled along the surface of the tail cone. Additionally, the static and total pressures p_s and p_t were measured along a path normal to the surface. The geometry of the body was constructed using ESDU curvature formulations and is shown in Figure 4.16. The surface normal path along which the pressures were measured is also indicated.
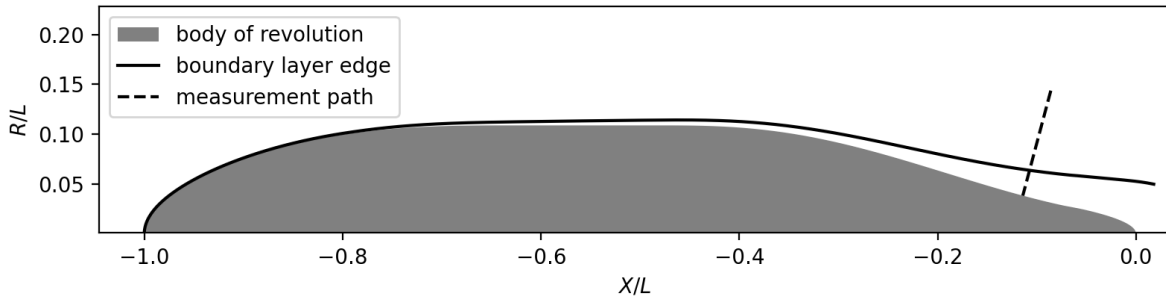

Figure 4.16: BOR geometry and the measurement path used in the experiment performed by van Sluis [41]. The boundary layer edge was plotted according to the results of the equivalent body model.

Experimental and computational setup

Because the experimental results have been obtained from a wind tunnel and the blockage of the physical BOR model is known to be high, it was decided to also include the wind tunnel walls in the computational model in order to make a fair comparison. Since modelling the wind tunnel walls is largely based on the same principles used for modelling the actuator disc, this feature was implemented as an extension to the actuator disc model and will be discussed later during this work in section 6.3. The non-dimensional parameters defining the flow condition are summarized in Table 4.4, where A_b/A_t is the frontal cross sectional area of the body divided by the cross sectional area of the wind tunnel test section. While the computational model assumes incompressible flow, the Mach number M at which the experiments were performed is less than 0.2. Any discrepancy caused by the compressibility of air should therefore be minimal.

Table 4.4: Non-dimensional parameters describing the flow condition.

|	experiment	computation
Re	7.42×10^6	
M	0.175	0
X_{trans}/L	0.2	
A_t/A_b	16.6	

Using the specified conditions, the unpowered configuration was modelled both in open air and within the wind tunnel walls using the settings listed in Table 4.5. The parameter L/L_t is the length of the body divided by the length of wind tunnel test section which is modelled as a uniform cylinder using N_t vortex rings and N_t control points.

Integration path analysis

Before proceeding to the comparison with experimental data, the effect of using the surface normal or flow normal integration path for computing the surface pressure will be discussed, as several new observations can be made on this particular geometry. As can be seen from Figure 4.17, the difference between the two integration paths becomes particularly large over the trailing edge, as it is blunt and the angle of the surface changes rapidly.

Table 4.5: Model settings used for computing the results presented in this section.

sources	135
control points	150
boundary layer elements	1500
boundary layer stream tubes	50
L_t/L	2.74
N_t	100
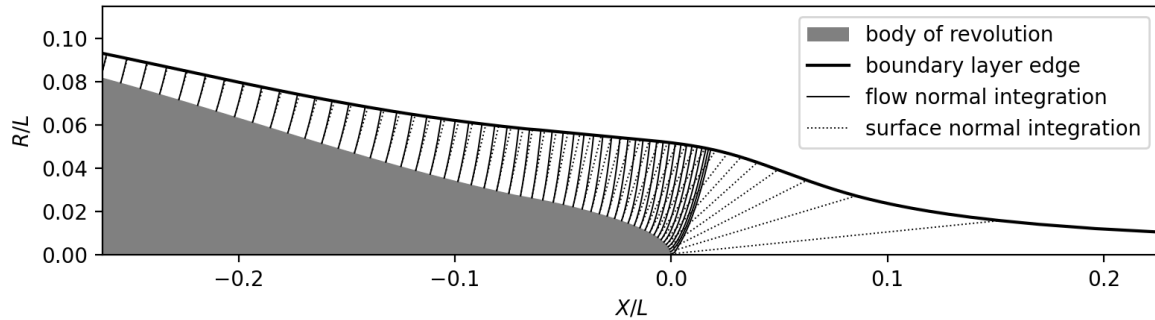
Figure 4.17: Comparison of the surface normal and flow normal integration paths around the BOR.

The boundary layer model also struggles to predict the boundary layer thickness and an unnatural contraction of the boundary layer is observed. Such unrealistic results can however be expected as the boundary layer model assumes that the flow is parallel to the surface, which is hardly the case over the blunt trailing edge. On the other hand, the flow normal integration path looks much more reasonable, despite the fact that it was computed based on the clearly inaccurate boundary layer predictions.

Based on these observations, it is therefore concluded that for a BOR with a blunt trailing edge, using the flow normal integration path is absolutely necessary for computing the surface pressure over the trailing edge and the drag of the body. While it should be kept in mind that flow separation is likely to occur over a blunt trailing edge, which means that the computed surface pressure can still be inaccurate, integrating along the flow normal direction is still seen as a much better option.

Comparison of pressure across the boundary layer
Moving on to the comparison between experimental and computational data, the total and static pressures were computed along the same path shown in Figure 4.16, along which the pressures were measured experimentally. Within the boundary layer, the static pressure was first evaluated using the uncorrected-surface, surface-surface and the flow-surface methods. The corresponding total pressures were then computed by simply adding the local dynamic pressure based on the velocity predicted by the boundary layer profile. Outside of the boundary layer, the total pressure was assumed to remain constant and the static pressure was computed based on the local flow velocity.

In this particular case, the flow-flow method was not used as it would require a complicated interpolation scheme for evaluating the pressure at an arbitrary point within the boundary layer. On the other hand, computing the static pressure above the surface using the other methods was easily implementable as the measurements were conveniently taken along a path perpendicular to the surface. Despite what was discussed previously, the measurements path is located further upstream where the where the flow direction is close to parallel with the surface of the body. The effect of integrating in the direction normal to the surface should therefore be minimal.

The pressures measured across the boundary layer profile are first compared with the computational results of a body in free air (without the wind tunnel walls) in Figure 4.18.

Together with actual measurements, a corrected data set is also shown. This corrected data set was provided by Van Sluis and the magnitude of the correction was computed using a third party panel code. The correction applied is supposed to subtract the effect of the wind tunnel walls from the experimental results and the corrected data should therefore agree with computational results of a body in free air. From Figure 4.18 we see that this is indeed the case and the agreement between the corrected
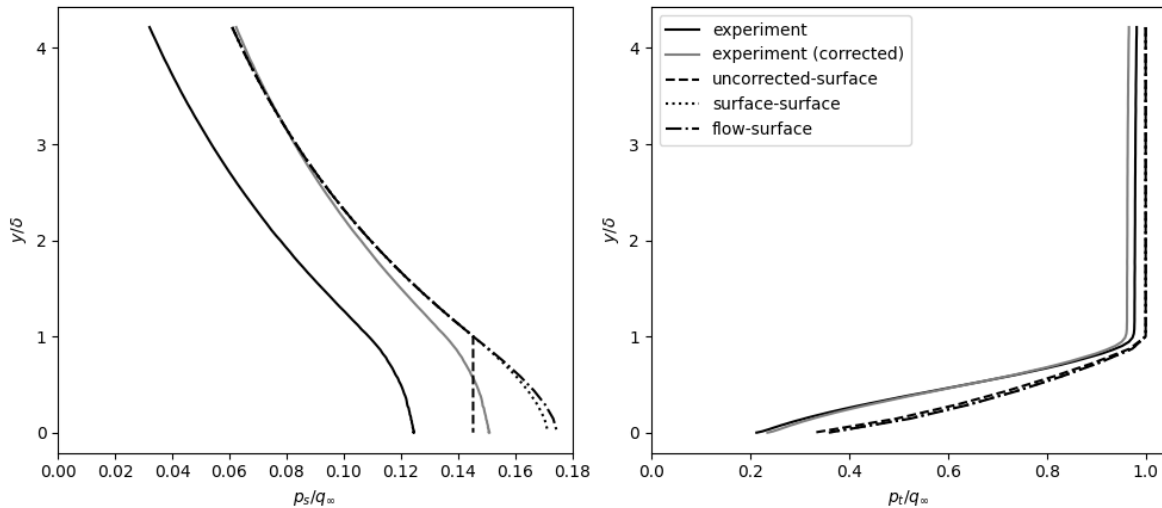
Figure 4.18: Corrected and uncorrected static and total pressure measured along the path shown in Figure 4.16 compared with computational results of a **body in free air**.

experimental and the computed results is indeed quite good.

The effect of the measurement correction appears to be a close to uniform increase in static pressure. This makes sense as the wind tunnel walls restrict the flow from expanding outwards as it moves around the body. As a result it is forced to accelerate in order to conserve mass flow, which means that a lower in static pressure is observed in the experimental results.

A second comparison is made in Figure 4.19, where the uncorrected experimental data is presented together with results computed for a body inside a wind tunnel.
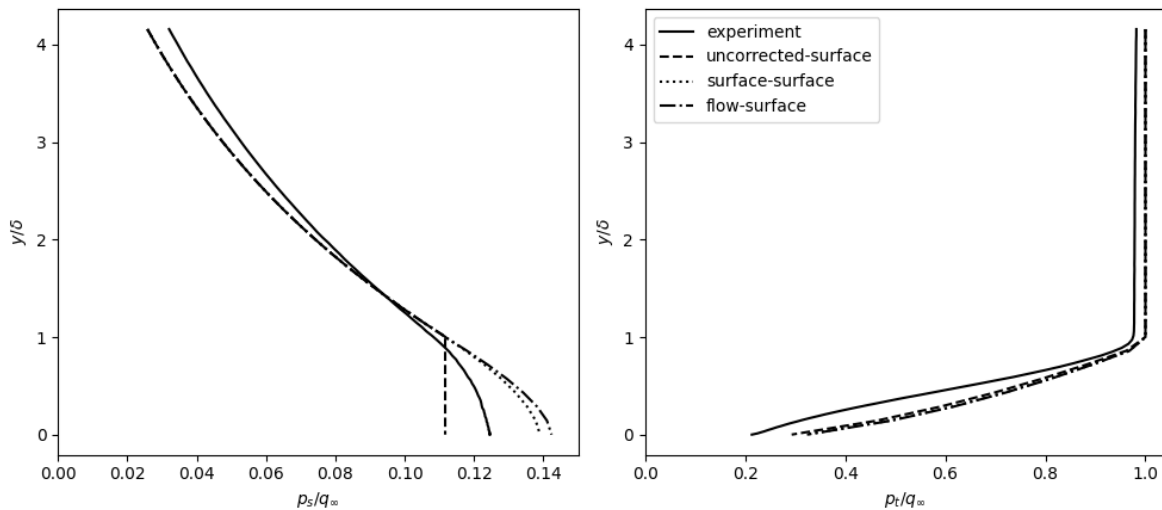

Figure 4.19: Uncorrected static and total pressure measured along the path shown in Figure 4.16 compared with computational results of a **body inside the wind tunnel**.

As can be seen, a similar agreement is observed in this comparison as well, which suggests that modelling of the wind tunnel walls was implemented correctly. After taking a closer look, including the wind tunnel walls in the computational model does seem to create a slightly larger difference in pressure than what is predicted by the correction applied to the experimental results. This can be explained by the fact that the computational model also takes the boundary layer into account in the form of an equivalent body. On the other hand, the effect of the boundary layer was neglected when the experimental results were corrected. This also means that the agreement between the experimental

and computational data should be better in Figure 4.19. This does seem to be the case, at least based on the maximum error magnitude.

Next, the effect of the various pressure correction methods will be discussed. As can be seen, using the uncorrected-surface method results in a constant static pressure across the boundary layer profile, which is expected, as that is the underling assumption behind this method. On the other hand, the static pressure computed using the surface-surface and the flow-surface methods varies widely across the profile. In this case, both of the methods result in a similar pressure distribution. This can be explained by the fact that the the boundary layer thickness is not excessively large with respect to the local body radius. The flow within the boundary layer therefore, in general, follows the curvature of the surface.

Another observation that can be made is that the static pressure gradient does not change abruptly over the boundary layer edge, when the pressure is corrected using either of the methods. This is a positive sign that suggests that the methods were implemented correctly.

While the general shape of static pressure profiles computed using the surface-surface and flow-surface methods is similar to the experimental results, a noticeable error is present, especially within the boundary layer itself. Because of the large amount of assumptions and simplifications that the computational model makes, tracing the cause of this error is not easy. One of the likely causes of this error, is the boundary layer model itself. From the total pressure plots we can see that even though the boundary layer thickness agrees well, the shape of the boundary layer profile appears to be quite different. While the computational model predicts a fuller boundary layer profile with a steep velocity gradient at the surface, the experimental results show a greater velocity deficit near the surface indicating a higher shape factor. This has direct consequences on the pressure computation using the surface-surface and the flow-surface methods, as the pressure is computed based on centripetal force, which is a function of the velocity within the boundary layer. Additionally, the shape factor has also direct influence on the viscous drag and the displacement thickness, which means that the external flow is also influences.

Looking at Figure 4.19 right, a difference in the computed and measured total pressure at the surface can be observed. This is in fact expected, as during the experiment, it was not possible to measure pressure directly at the surface, due to the thickness of the probe. The lowest measurement was therefore made slightly above the surface. Because the model is attached to a balance, it has some freedom to move and the exact distance to the wall is therefore unknown. The graphs were therefore manually adjusted to start at the surface.

Another reason which likely does not cause large errors but is also worth mentioning, is the fact that the boundary layer development over the wind tunnel walls is not considered.

Comparison of pressure along the surface

The second data set of experimental results containing the surface pressure measured along the tail cone of the body is compared with computational results in Figure 4.19.

As can be seen, the agreement between the calculations and experiment is quite good. The error in pressure coefficient at the location where the measurements in the surface normal direction were made is around 0.02, which is the same as in Figure 4.20. The error between the experiment and computation appears to be quite systematic and roughly equal to this value over the entire tail cone.

One thing that is rather eye catching and should be explained, is what happens with the pressure distribution over the trailing edge in Figure 4.20. The abrupt variations in surface pressure are in fact caused by poor discretization of the geometry. The BOR is made of two physical components: The body itself, and a the spinner of a propeller with removable blades which forms the trailing edge section. While both of these objects are smooth and appear to have been described by mathematical functions, it seems like the geometries were stitched together using a third function. As can be seen from Figure 4.21, which shown the first derivative of the body radius, this resulted in two locations where the surface curvature changes abruptly. In reality the spikes in pressure predicted by the computational model would not occur, as they would be damped out by the compressibility of air.

Comparison of the drag of the body

Finally, a comparison of experimentally measured and computed drag coefficient is made in Table 4.6. Once again, the corrected experimental results are compared with computations for a body in free air and the uncorrected experimental results are compared with computations of the body inside the wind tunnel.
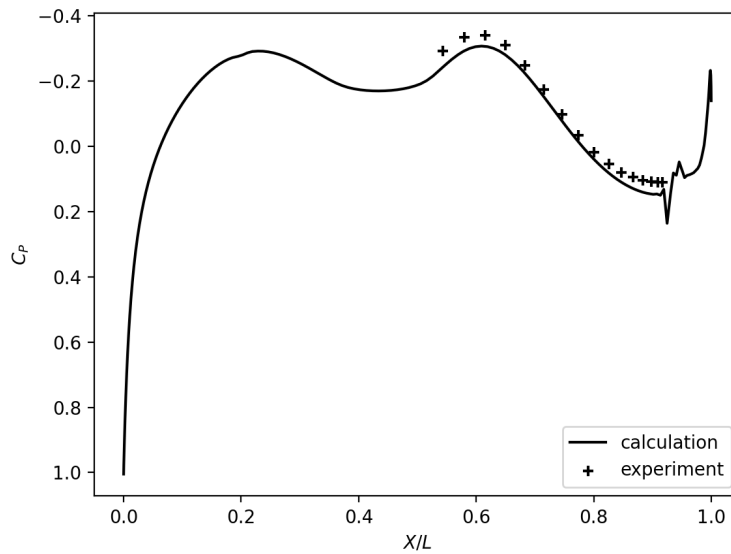
Figure 4.20: Uncorrected pressure coefficient measured along the surface of the body compared with computational results obtained using the flow-flow method for the body inside the wind tunnel.
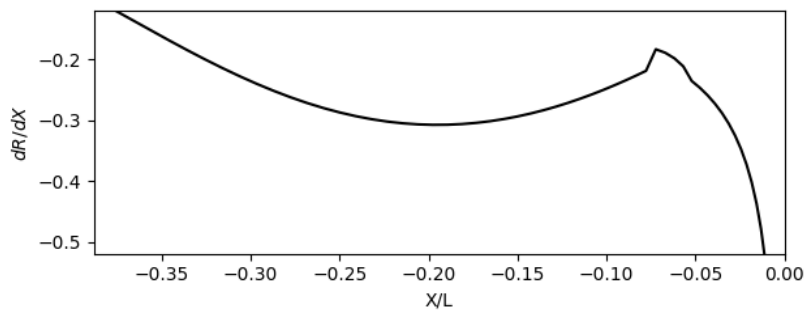

Figure 4.21: The first derivative of the body radius in the tail cone region of the BOR shown in Figure 4.16.

Table 4.6: The drag coefficients of the body in free air and wind tunnel. Comparison of experimental and computational results based on the surface pressure calculated using the flow-flow method.

	C_{D_p}	C_{D_v}	C_{D_t}	Error C_{D_t}
	body in open air			
experiment (corrected)			0.05513	
computation	0.01553	0.04078	0.05630	2.1 %
	body in wind tunnel			
experiment (uncorrected)			0.06020	
computation	0.01779	0.04296	0.06075	0.9 %

As can be seen the agreement is in both cases very good, with the second comparison being slightly better. This suggests that the entire computational model up to this point was implemented correctly, including the capability to model the wind tunnel walls. The fact that better agreement is seen in the second comparison is also in line with expectations. As was discussed, this can be explained by the fact that the effect of the BOR boundary layer was not taken into account when the experimental results were corrected.

The actuator disc model

Given the aim of constructing a low-fidelity computationally inexpensive model, it was decided to model the propulsor as an actuator disc, an infinitely thin surface that creates a sudden increase in total pressure Δp. The potential flow model described in the paper of Van Kuik [22] was used as a basis (more information regarding it can also be found in his book [42]). The model works for both energy adding and energy extracting actuator discs. In the work of Van Kuik, computational results were demonstrated to agree well with experiment. During the implementation of the model, issues with the stability of the convergence scheme were encountered. As a result a new convergence scheme had to be developed.

The structure of this chapter is as follows: The model of Van Kuik is first described in section 5.1 and is followed by a discussion of the adjustments made to it in section 5.2. The propulsive power computation of the actuator disc in then considered in section 5.3. Finally, the adjusted model is validated in section 5.4.

5.1. The model of Van Kuik

The actuator disc is modelled in potential flow by placing a distribution of N_v discrete vortex rings along the slipstream of the propulsor. The first vortex ring is placed at the outer edge of the actuator disc and the distribution extends downstream until a prescribed point X_{wake}. Past this point the slipstream is assumed to be fully contracted and is modelled using a semi-infinite vortex tube of constant radius R_{wake}.

Two boundary conditions are prescribed to the actuator disc slipstream. The first one being that the velocity component normal to the slipstream surface must be zero and the second one is that the slipstream surface must be force free. The two sets of unknown variables are the strengths and the radii of each vortex ring i and must be solved for such that the boundary conditions are satisfied. The two input variables of the model are the thrust and the radius of the fully contracted slipstream. The equations giving the velocity induced by a vortex ring can be found in Appendix B.

The model is initialized by distributing the vortex rings according to the spacing function given by Equation 5.1, where $c_1 = 2.72$ and $c_2 = 0.7$.

$$X_i = X_{\text{wake}} \left(1 - \cos\left(\frac{i\pi}{c_1 N_v} \right) \right)^{c_2} \tag{5.1}$$

This function is used to obtain a higher density of vortex rings near the actuator disc, which is the area of interest. Initially, the radius of all the vortex rings is assumed to be equal to prescribed downstream slipstream radius. Given the prescribed thrust of the actuator disc, the increase in total pressure Δp is defined as the thrust divided by the area of the disc. The vortex strength γ of the semi-infinite vortex tube starting from X_{wake} can be computed using Equation 5.2 [42].

$$\gamma = \sqrt{2\Delta p + U_\infty^2} - U_\infty \tag{5.2}$$

The solution procedure proposed for computing the vortex strengths and radii works by iteratively adjusting both of the parameters based on the error in the two boundary conditions. The vortex strengths

Γ_i are adjusted using the local difference in pressure across the slipstream and the radii of the vortex rings R_i are adjusted using the stream function and the normal velocity across the slipstream. The first of which is used to achieve convergence and the second is used for fine tuning. In this convergence scheme the pressure difference, stream function and the normal velocity are all evaluated at the center of the vortex rings using a kernel radius to compute the contribution of the vortex on itself. More details regarding this model can be found in the work of Van Kuik [22].

5.2. The adjusted actuator disc model

While implementing the actuator disc model, the convergence scheme proposed by Van Kuik was found to be unsuitable, the main problem being with the iterative procedure used for adjusting the vortex ring radii. While the first iterative procedure based on the stream function was found to be stable, it is unsuitable because evaluating the stream function is not possible for source segments which are used within the BOR model. As a result it would not be possible to combine the BOR and the actuator disc potential flow models together. On the other hand, the second iterative procedure which is based on the normal velocity across the slipstream could be combined with the BOR model, however it was found to be marginally stable and sensitive to any disturbance. This is likely also the reason why Van Kuik advised to only use it for fine tuning.

Another problem which further complicates the use of this convergence scheme is the fact that a kernel radius must be used when evaluating the velocity induced by a vortex onto itself. This poses a problem as this self-induced velocity largely depends on the vortex kernel radius, which is an unknown variable. While Van Kuik tuned the kernel radius for the best results, this value was optimized for one particular discretization of the actuator disc and hence remains unknown for arbitrary discretizations.

5.2.1. The new iterative procedure

After trying many different things to improve the stability of the iterative procedure based on the normal velocity, an alternative convergence scheme was conceived that does not suffer from the above mentioned issues.

First of all, it was decided to not evaluate the velocity at the vortex cores, but instead at control points placed at the half way points between vortices. This eliminates the need to use the kernel radius and the problems related to using it. A schematic showing the resulting actuator disc discretization is shown in Figure 5.1. Secondly, the stability problem of the convergence scheme was fixed by not solving the vortex strengths iteratively, but instead constructing and solving a linear system in each iteration such that the normal velocity condition is always satisfied. Iteration is therefore only used to solve for the slipstream radius.
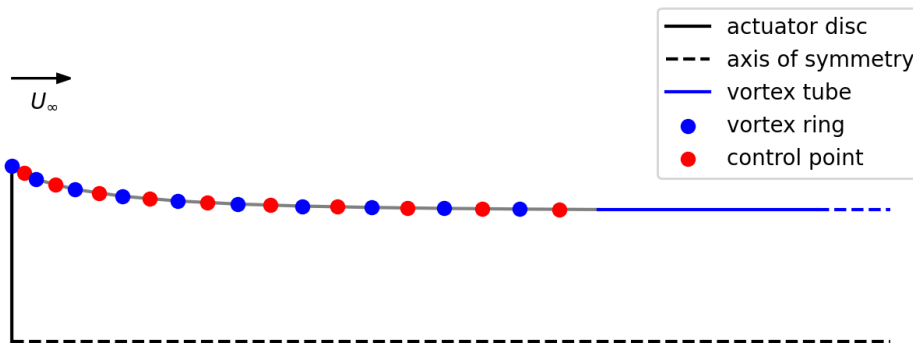

Figure 5.1: Example of an actuator disc model constructed using 10 vortex rings and 10 control points.

The linear system of equations for solving the vortex strengths is similar to the one used within the BOR model and can be formulated using Figure 5.2. The equations for computing the velocity components $U_{X,ij}$ and $U_{R,ij}$ induced by vortex ring i at the location of control point j as well as the equations for computing the velocity components $U_{X,tj}$ and $U_{R,tj}$ induced by the vortex tube at the location of control point j can be found in Appendix B. For each control point an equation is written by summing up all the velocity contributions in the direction normal to the slipstream surface and equating them to zero. This results in Equation 5.3, where the subscript $\perp$ denotes the components of the velocity

components perpendicular to the slipstream surface. Writing an equation for each control point, a linear system of N_v equations with N_v unknown parameters is obtained, where Γ_i are the unknowns.
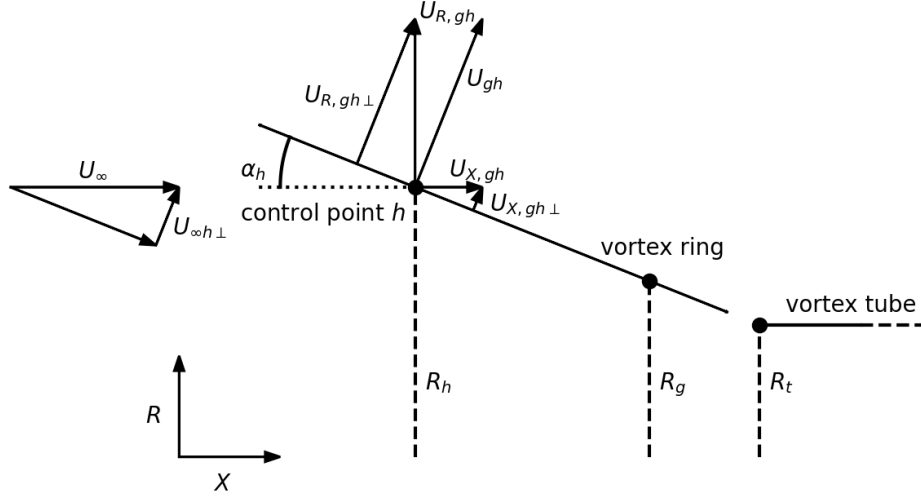

Figure 5.2: Schematic explaining the various variables required to compute the velocity induced by a vortex ring g and the freestream velocity U_∞ at a control point h in the direction normal to the slipstream.

$$\sum_{i=1}^{N_v} \left(U_{X,ij\perp} + U_{R,ij\perp}\right) + U_{X,th\perp} + U_{R,th\perp} + U_{\infty h\perp} = 0 \tag{5.3}$$

Using the angle of the slipstream surface α_j at control point j, the equation can be written in terms of the velocity components $U_{X,ij}$ and $U_{R,ij}$, as is shown in Equation 5.4. Writing the velocity components as the vortex strength Γ_i multiplied by a constant k allows Γ_i to be factored out, which results in Equation 5.5. The entire system of equations can be then written in matrix form as is shown in Equation 5.6 and the unknown vortex strengths Γ_i can be determined by solving the linear system using matrix inversion.

$$\sum_{i=1}^{N_v} \left(U_{X,ij} \sin\alpha_j + U_{R,ij} \cos\alpha_j\right) + U_{X,tj} \sin\alpha_h + U_{R,tj} \cos\alpha_j + U_\infty \sin\alpha_j = 0 \tag{5.4}$$

$$\sum_{i=1}^{N_v} \left(k_{X,ij} \sin\alpha_j + k_{R,ij} \cos\alpha_j\right) \Gamma_i = -U_{X,tj} \sin\alpha_j - U_{R,tj} \cos\alpha_j - U_\infty \sin\alpha_j \tag{5.5}$$

$$\begin{bmatrix} c_{11} & c_{21} & \dots & c_{N_v 1} \\ c_{12} & c_{22} & \dots & c_{N_v 2} \\ \vdots & \vdots & \ddots & \vdots \\ c_{1N_v} & c_{2N_v} & \dots & c_{N_v N_v} \end{bmatrix} \begin{bmatrix} \Gamma_1 \\ \Gamma_2 \\ \vdots \\ \Gamma_{N_v} \end{bmatrix} = \begin{bmatrix} d_1 \\ d_2 \\ \vdots \\ d_{N_v} \end{bmatrix} \tag{5.6}$$

where $\quad c_{ij} = k_{X,ij} \sin\alpha_j + k_{R,ij} \cos\alpha_j \quad$ and $\quad d_j = -U_{X,tj} \sin\alpha_j - U_{R,tj} \cos\alpha_j - U_\infty \sin\alpha_j$

Using this procedure, the vortex strengths can be solved for in order to satisfy the no flow across the slipstream condition for a given slipstream shape. The radii of slipstream however still need to be solved iteratively in order to satisfy the second boundary condition which states that the slipstream surface must be force free. In order to avoid problems with the kernel radius, this condition is also prescribed at the control point locations. Use was made of Equation 5.7 where U_s is the local velocity at the slipstream surface and γ_s is the local vorticity per unit length which is defined as the vortex strength divided by the distance between two adjacent vortices. Equation 5.7 was proposed by Van Kuik and was said to hold when the static pressure difference across the slipstream is zero.

$$2U_s\gamma_s = C_T U_\infty \tag{5.7}$$

Substituting the definition of thrust coefficient C_T given by Equation 5.8 into Equation 5.7 results in Equation 5.9. This relation can be turned into an iterative procedure for adjusting the radius of the slipstream as is shown in Equation 5.10. Here, Δp is the prescribed total pressure increase provided by the actuator disc and $U_{sheet}\gamma_{sheet}$ is the predicted total pressure increase based on the local flow properties. Once all of the boundary conditions are met, these two values should be equal. The radius adjustment is also proportional to the size of the slipstream, hence the presence of the term R. A damping constant d is also used and must be tuned for the best results. While other iterative procedures may also work, this one was found to be stable and reliable.

$$C_T = 2\frac{\Delta p}{U_\infty^2} \tag{5.8}$$

$$\Delta p = U_{sheet}\gamma_{sheet} \tag{5.9}$$

$$\Delta R = R(U_{sheet}\gamma_{sheet} - \Delta p)d \tag{5.10}$$

In practice, U_{sheet} and γ_{sheet} are evaluated at the control points and the values are used to adjust the radius of the nearest upstream vortex. The control points are then repositioned to once again to lie at the center between two vortices in each iteration. Using this procedure, the radius of the semi-infinite vortex tube stays constant and the radius of the actuator disc changes, which is opposite to what is desired. In order to fix this problem, the entire slipstream geometry is scaled in each iteration in both the X and the R directions equally. As a result the actuator disc radius remains constant throughout the iteration process and the semi-infinite vortex tube radius and downstream position are scaled linearly.

The quantity for measuring the degree of convergence was defined as ϵ, the average pressure error magnitude over all of the control points using Equation 5.11. A summary of the iterative procedure for solving the actuator disc problem can be found below.

$$\epsilon = \frac{1}{N_v}\sum_{j=0}^{N_v}|U_j\gamma_j - \Delta p| \tag{5.11}$$

The actuator disc iterative procedure
Initialization:

- Assume that the radius of the actuator disc slipstream is constant and equal to the actuator disc radius
- Compute the strength of the vortex tube based on the prescribed thrust

Iteration (repeat until ϵ converges):

1. Compute the vortex strengths by solving Equation 5.6 in order to satisfy the no flow across slipstream condition
2. Adjust the radius of the vortex rings using Equation 5.10
3. Reposition the control points such that they lie along the slipstream
4. Scale the entire actuator disc slipstream such that the actuator disc radius remains constant

5.2.2. Convergence analysis
The typical convergence behavior of the iterative procedure is shown in Figure 5.3, where ϵ_0 is the error during the first iteration. As can be seen, the convergence is linear for the most part, except at the very beginning where it is initially faster and at the end when it is terminated due to the machine precision limit. Apart from this, Figure 5.3 also shows the importance of correctly choosing d. In general, increasing d also increases the convergence speed, however this is only true until a certain point. Once d is greater than a certain value, around 1.9×10^{-4} in this example, the solution starts to oscillate between iterations and convergence is no longer observed.
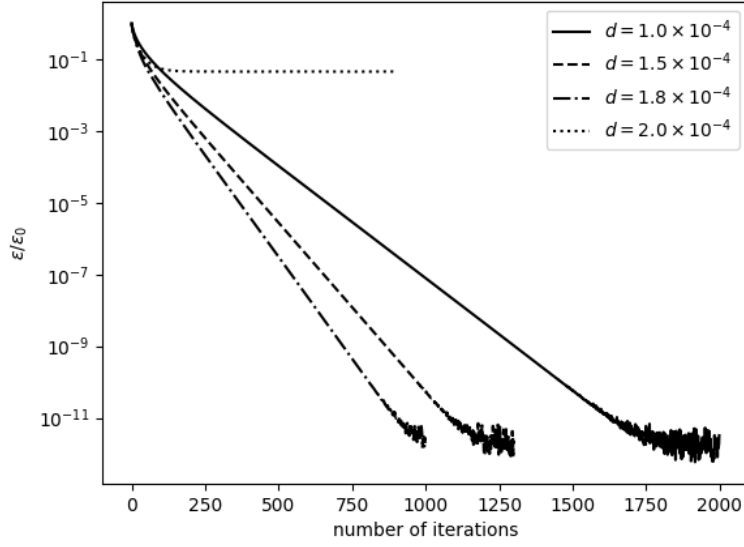
Figure 5.3: The convergence behavior of the iterative procedure with a damping constant $d = 5 \times 10^{-5}$ for an actuator disc modelled using 100 vortices and $X_{\text{wake}} = 30 R_{\text{wake}}$.

The convergence speed is also greatly influenced by the number of vortices N_v. One of the most computationally intensive tasks is evaluating all of the entries $c_{i,j}$ of the matrix in Equation 5.6. Because the number of the matrix entries is equal to N_v^2, the convergence speed was also found to approximately scale with N_v^2 for a given d. Additionally, the largest usable value of d was found to decrease with N_v. As a rule of thumb, when increasing N_v by a factor f, d has to be scaled by $1/f$ in order to maintain stability. Taking all of this into account, the optimal computational time of the actuator disc model scales roughly with N_v^3.

5.3. Power computation

In order to evaluate the BLI benefit of a propulsive fuselage configuration, the power consumption of the propulsor must be evaluated. While the PSC should be computed based on the shaft power, this is not possible with an actuator disc representation of the propulsor. A simplified approach is therefore to compute the propulsive power and assume that the efficiency of the propeller remains the same for both the non-BLI and the BLI configurations. The propulsive power P_p can be easily computed by multiplying the thrust by the velocity at the actuator disc plane. However, since the flow velocity is not constant across the actuator disc, this must be done by integrating pressure difference across the area of the actuator disc as is shown in Equation 5.12. Further, it is necessary to use the velocity component U_X, which is aligned with the direction of the thrust. In practice, Equation 5.12 needs to be integrated numerically.

$$P_p = \int_0^{R_{disc}} 2\pi R \Delta p U_X dx \tag{5.12}$$

As a recommendation for future work, the model could be combined with a Blade Element Theory (BET) model, which would allow the shaft power to be evaluated. Doing so, would however also require the actuator disc model to be expanded to allow for a non-uniform thrust distribution along the radial direction. This is possible and can be done by stacking multiple actuator discs with progressively smaller radii on top of each other. While modelling such a thrust distribution was tested and was found to work, the proper implementation of this feature was considered to be out of the scope of this work.

5.4. Validation of the actuator disc model

Validation of the actuator disc model was performed by comparing computational results with those presented in the work of Van Kuik [42]. An energy extracting actuator disc with a $C_T = 8/9$ was modelled using a varying number of vortices. Unfortunately, due to computational time, it was only possible to model the actuator disc with a maximum of 1000 vortices, while Van Kuik was able to model it using 9600 vortices, presumably using a more powerful machine.

The radius of the slipstream is compared in Figure 5.4. As can be seen, the agreement between the results improves with the increasing number of vortices, although the agreement in the region near actuator disc itself is already good when using 100 vortices only. The solution of the computational model proposed in this work does however appear to be converging to a slightly different result, as the slipstream radius for the 500 and 1000 vortex solutions only differs at the downstream end. The likely cause of this is the fact that the velocity in the present model is being evaluated a different location, as this is the only difference between the models in terms of boundary conditions.
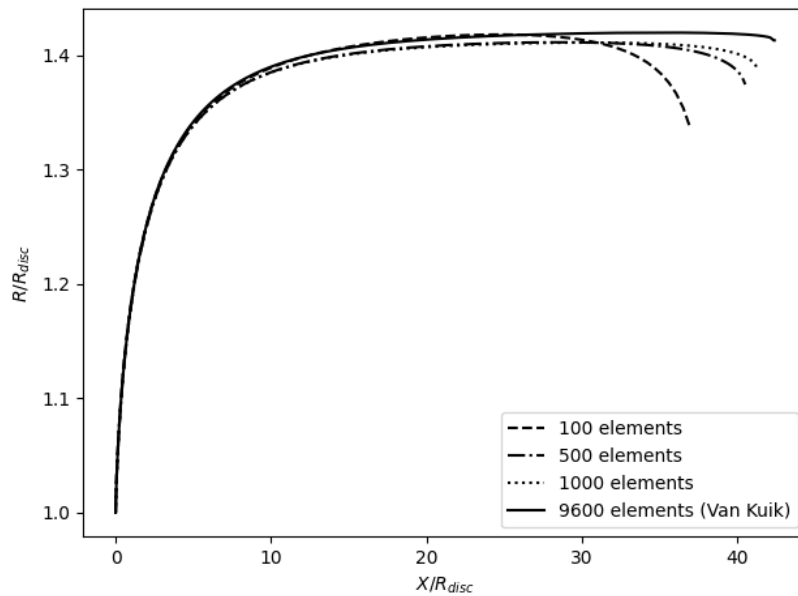

Figure 5.4: The slipstream radius of an energy extracting actuator disc modelled using increasing number of vortices. Computed results are compared to those of Van Kuik [22].

The velocity components at the actuator disc plane are compared in Figure 5.5. A similar improvement in accuracy with the increasing number of vortices is observed in this case as well. While the slipstream radius near the actuator disc agreed well, even when using 100 vortices, this is not the case for the flow velocity and significant deviations can be observed, especially near the edge of the actuator disc. These large deviations can be considered a result of discretization and can be explained by the fact that when using fewer vortices, the vortex strengths need to be higher. This means that the induced velocity is also greater when evaluated close to the vortex itself.
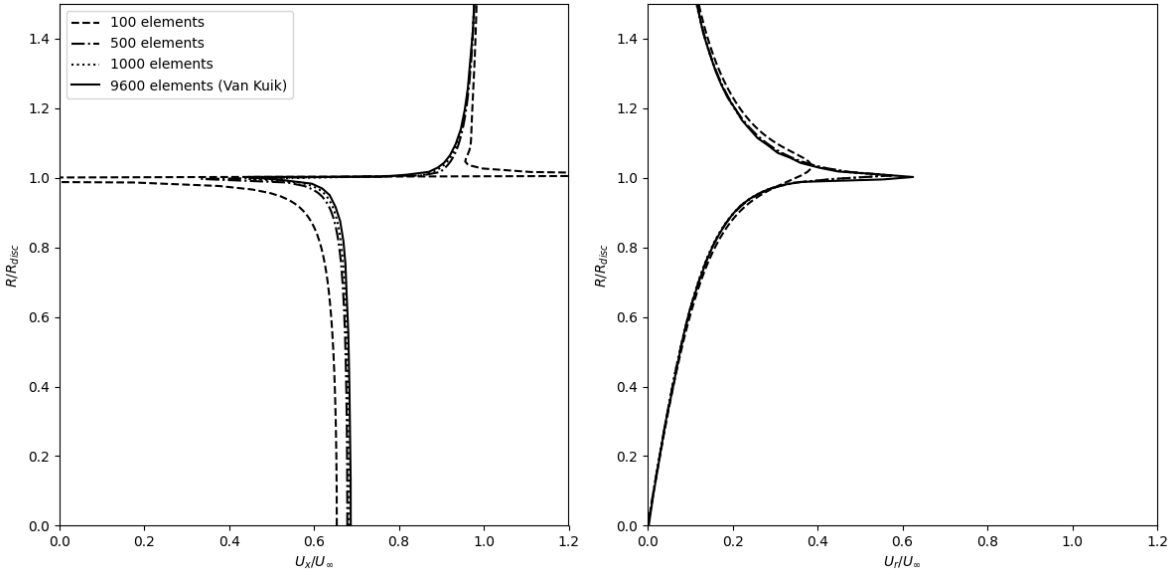
Figure 5.5: The velocity at the plane of an energy extracting actuator disc modelled using increasing number of vortices. Computed results are compared to those of Van Kuik [22].

6

The combined model

In the previous two chapters, the development of the equivalent body and the actuator disc models has been discussed. The focus of this chapter will be combining these two models such that a BOR with an actuator disc placed at the trailing can be modelled.

As a first step, combining the two models as they are will be discussed in section 6.1. After that the need of a boundary layer wake correction and the implementation of it will be treated in section 6.2. The model will be then extended to include the possibility of modelling a body inside a wind tunnel in section 6.3. Finally, section 6.4 will discuss the combined iterative procedure of the entire computational model.

6.1. Combined BOR and actuator disc model

Combining the equivalent body and the actuator disc models is relatively straight forward and can be done in two steps. Firstly, the two linear sets of equations can be combined for solving the potential flow around both of the objects. Secondly, the two iterative procedures for solving the boundary layer parameters and the actuator slipstream radius can also be combined into a single iterative procedure.

The result of combining the two linear systems results in the set of equations shown in matrix form in Equation 6.1. Here, the sub matrices that consist of the a and c terms remain the same as in the isolated models and so do the d terms as well. The additional e and f terms are used to take the interference between the actuator disc and the body of revolution into account.

$$\begin{bmatrix} a_{11} & a_{21} & \dots & a_{n1} & e_{11} & e_{21} & \dots & e_{N_v 1} \\ a_{12} & a_{22} & \dots & a_{n2} & e_{12} & e_{22} & \dots & e_{N_v 2} \\ \vdots & \vdots & \ddots & \vdots & \vdots & \vdots & \ddots & \vdots \\ a_{1m} & a_{2m} & \dots & a_{nm} & e_{1m} & e_{2m} & \dots & e_{N_v m} \\ f_{11} & f_{21} & \dots & f_{n1} & c_{11} & c_{21} & \dots & c_{N_v 1} \\ f_{12} & f_{22} & \dots & f_{n2} & c_{12} & c_{22} & \dots & c_{N_v 2} \\ \vdots & \vdots & \ddots & \vdots & \vdots & \vdots & \ddots & \vdots \\ f_{1N_v} & f_{2N_v} & \dots & f_{nN_v} & c_{1N_v} & c_{2N_v} & \dots & c_{N_v N_v} \end{bmatrix} \begin{bmatrix} Q_1 \\ Q_2 \\ \vdots \\ Q_n \\ \Gamma_1 \\ \Gamma_2 \\ \vdots \\ \Gamma_{N_v} \end{bmatrix} = \begin{bmatrix} b_1 \\ b_2 \\ \vdots \\ b_m \\ d_1 \\ d_2 \\ \vdots \\ d_{N_v} \end{bmatrix}$$

(6.1)

Each element e represents the contribution of a vortex ring to the velocity experienced at control point on the equivalent body and can be therefore constructed using Equations B.1 and B.2 by using the equivalent body control point coordinates. On the other hand, each element f represents the contribution of a source segment to the velocity experienced at control point in the actuator disc slipstream and can be therefore constructed using Equations 4.1 and 4.2 by using the actuator disc control point coordinates.

Additionally, the terms b also have to be adjusted. This is because the semi-infinite vortex tube also induces a velocity at the equivalent body control points, but its strength is not a variable (its strength is known, computed using the prescribed thrust). Its contribution therefore has to go on the right side of the equation and can be computed in the same way as for the d terms, but using the coordinates of the equivalent body control points.

In order to solve both of the models simultaneously, the iterative procedures for solving the boundary layer properties and the actuator disc slipstream radius also have to be combined. This is mostly a matter of executing the steps of both of the procedures in an order that makes sense and results in a stable algorithm. The iterative procedure will be described in detail in section 6.4.

6.2. The boundary layer wake correction

The previous section has explained the simplest way of combining the BOR and the actuator disc models. The problem with this approach however, is the fact that the boundary layer wake has not been taken into account. Neglecting the wake development was considered acceptable for the isolated body, but doing so has greater consequences for the combined model, as the wake is being ingested by the actuator disc. When the wake is not taken into account, the actuator disc experiences a higher inflow velocity and this means that the slipstream contraction is not modelled correctly. The reason behind this is the fact that faster flow has to be accelerated less to produce the same amount of thrust and based on mass flow conservation, it is known that less flow acceleration comes with less flow contraction. As a result, neglecting the wake results in the actuator disc slipstream contraction being underpredicted, which has an impact on the external flow and therefore also the drag of the body.

6.2.1. Overview

The most straight forward way to take the wake into account, is to simply split the wake into N_{st} stream tubes[1] and compute their development using the Bernoulli's equation and mass flow conservation. An example of such a wake discretization is shown in Figure 6.1. A shortcoming of this method is that it assumes that the flow is inviscid. This is however not the case due to the velocity gradients that exist within the wake. This means that this method is not able to predict the diffusion of velocity across the wake, but it should provide a first order estimate of the wake contraction induced by the actuator disc. This simplification is also in line with the actuator disc model which does not consider viscous effects that take place along the slipstream.
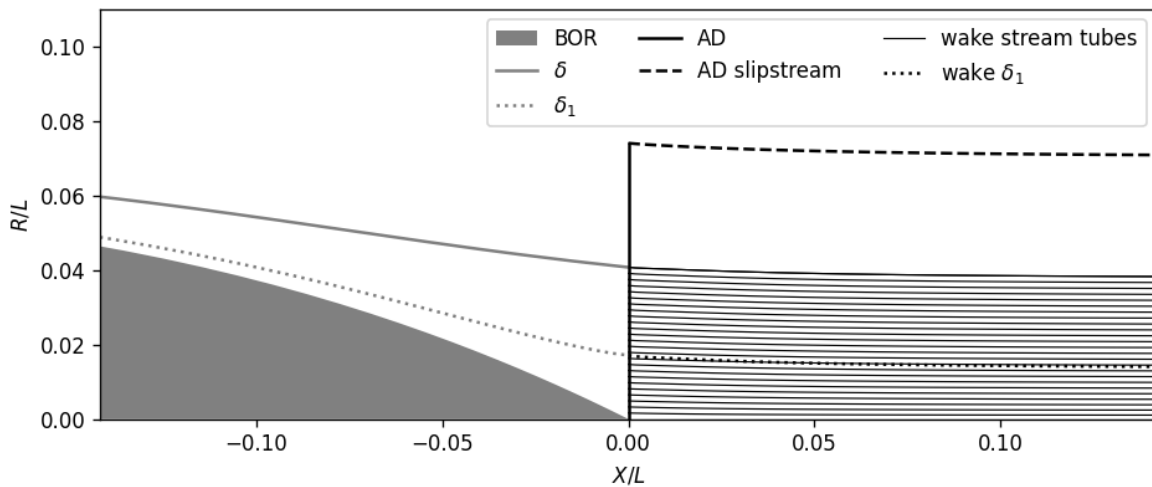

Figure 6.1: Example of a wake discretized into 25 stream tubes.

The wake is defined to start at the trailing edge and in order to keep things simple, its starting cross section is assumed to be perpendicular to the axis of symmetry, rather than perpendicular to the flow. The start of the stream tubes is defined such that the thickness of all stream tubes in the R direction is the same. In order to make the discretizatiom simpler, the actuator disc is now also constrained to be at the trailing edge and therefore the plane where the wake starts coincides with the actuator disc plane. Because the boundary layer is defined perpendicular to the surface of the body, a small area exists

---

[1]Note that N_{st} is also the number of stream tubes used for discretizing the boundary layer when computing the surface pressure. While a different number of stream tubes could be used, throughout this work they will be assumed to be the same, as this also makes the most sense from the perspective of a creating a good discretization.

where it overlaps with the wake. Avoiding this problem would however require using a flow orthogonal coordinate system for both the boundary layer and the wake. Downstream of the actuator disc, the radii of the stream tubes are defined at discrete locations, at the same X coordinates as the control points of the actuator disc slipstream. Using this distribution as opposed to another spacing along the X axis was found to have a positive impact on the convergence of entire the model.

6.2.2. Inflow properties

The first step computing the streamtube contraction is to compute the flow properties at the start of each stram tube, namely the velocity, the mass flow and the total pressure. The flow properties over a stream tube cross section at a given downstream location are considered to be constant and the area centroid is used as the representative location for computing them. The velocity at $X = 0$ can be easily computed as it is defined by the boundary layer profile. The only complication in computing it is the fact that the boundary layer is defined at discrete locations. Linear interpolation is therefore used to compute the velocity using the two neighboring boundary layer profiles at the start of each stream tube.

In order to compute the mass flow of the stream tubes, the flow angle needs to be known. At the start plane, this can be determined using the boundary layer stream tubes that were set up for computing the surface pressure correction in subsection 4.4.2. Provided that the same number of stream tubes were used for the boundary layer and the wake, their discretizations should be identical at $X = 0$ and the angle of the boundary layer stream tubes can be used directly to compute the flow angle at the start of the wake stream tubes.

The final quantities that needs to be computed at the start of the stream tubes are the total and static pressures p_t and p_s. The total pressure is always equal to the sum of the static and dynamic pressures p_t and p_s, as is shown in Equation 6.2. If the freestream static pressure is assumed to be zero, the total pressure becomes equal to the freestream dynamic pressure giving Equation 6.3. This means that the static pressure can be related to velocity at any point in the flow using Equation 6.4.

$$p_t = p_s + q = p_s + \frac{1}{2}\rho U^2 \tag{6.2}$$

$$p_t = \frac{1}{2}\rho U_\infty^2 \tag{6.3}$$

$$p_s = \frac{1}{2}\rho U_\infty^2 - \frac{1}{2}\rho U^2 \tag{6.4}$$

The actuator disc provides a sudden increase to the total pressure Δp. The static and total pressures within the actuator disc slipstream can therefore be computed using Equations 6.5 and 6.6.

$$p_t = p_s + q = \frac{1}{2}\rho U_\infty^2 + \Delta p \tag{6.5}$$

$$p_s = \frac{1}{2}\rho U_\infty^2 + \Delta p - \frac{1}{2}\rho U^2 \tag{6.6}$$

Within the boundary layer, a loss of total pressure occurs due to friction and as a result it is no longer conserved. Therefore, the total pressure at the start of the wake stream tubes has to be computed based on the static pressure using Equation 6.2. Given the simple nature of this correction, an assumption is made that the static pressure across this plane is constant and equal to the pressure at the edge of the wake. Assuming that the wake starts right behind the actuator disc, Equation 6.6 should be used to compute p_s.

6.2.3. Wake development

Once the inflow properties are known, the development of each stream tube can be computed at each downstream location. The radii of each stream tube are computed using mass flow and total pressure conservation. Because the viscous effects within the wake are not taken into account, the total pressure within a stream tube is conserved. At each downstream location, the static pressure is first computed at the edge of the wake using Equation 6.6 and is once again assumed to be constant across the wake. The radii of the stream tubes are then computed starting from the inside and working towards the edge

of the wake. The first step is to compute the velocity within each stream tube. This is done by simply rearranging Equation 6.3 for the velocity.

Once the velocity is known, the cross sectional area of a stream tube can be computed using mass flow conservation. Because the angle of the flow is unknown until the radius is determined, it is first assumed that the flow angle is zero and an estimate of the area is made. Because the process starts from the inner stream tube, the area can be used to compute the outer radius. Once this is known the flow angle can be computed as the average of the inner and outer streamtube walls between the current and the neighboring upstream location. After this a new estimate of the cross sectional area can be made. The radius of the stream tube was observed to converge very quickly and the process is therefore stopped after performing five iterations. While one could neglect the flow angle altogether, given how small it is looking at Figure 6.1, including it was found to have a notable impact on the stream tube contraction.

Once the development of the stream tubes is computed, the next step is to determine the displacement thickness of the wake so that the equivalent body can be expanded. The displaced mass flow $\dot{m}_{disp}$ is defined as the mass flow that would be present without a wake minus the actual mass flow that is present. In practice this is computed using Equation 6.7 where R_e is the wake edge radius, U_e is the velocity at the wake edge and $\dot{m}_w$ is the sum of the mass flows of all of the stream tubes. Once $\dot{m}_{disp}$ is known, Equation 6.8 is used to determine the radius of the area which it occupies, which is also known as the displacement thickness δ_1.

$$\dot{m}_{disp} = \rho \pi R_e^2 U_e - \dot{m}_w \tag{6.7}$$

$$\delta_1 = \sqrt{\frac{\dot{m}_{disp}}{\rho \pi U_e^2}} \tag{6.8}$$

The final step in implementing the wake correction is to expand the equivalent body downstream. This is simply done by adding control points and source segments to the equivalent body model. The control points are added at the displacement thickness of the wake, at the same X locations at which the wake is defined. A source segment is also added for each control point at the axis of symmetry. The start and end locations of each source source segment coincide with the X coordinates of the actuator disc vortex rings, or the start of the semi-infinite vortex tube in the case of the last source segment end. Because the control points and the source segments are simply added to the equivalent body, there is no need to change the way in which the potential flow linear system is formulated.

As was already mentioned, the boundary layer and the wake discretizations overlap in a small triangle. This becomes a problem because the distribution of control points that represent the boundary layer and the wake also begin to overlap. While in theory the boundary layer and the wake displacement thicknesses should coincide, in practice, the lines meet at the beginning of the wake and diverge slightly in the overlapping region. The reason for this discrepancy could be the fact that the boundary layer model takes viscous effects into account while the wake model does not. Another reason however, is also likely the fact that the two objects are defined in different coordinate systems and make different small angle approximations.

While the model is still capable of functioning even with this overlapping control point distribution, the condition number is increased as neighboring control points are prescribing a different flow angle. It is therefore considered better to remove the boundary layer control points from this region, as well as their corresponding source segments.

6.3. Wind tunnel modelling

As an extension to the model, it was decided to add the possibility of modelling a wind tunnel test section. When an aerodynamic body is tested in a wind tunnel, the flow around the body is confined by the tunnel walls. As a result, the acceleration of flow around the body is increased, which can lead to higher drag. Modelling the wind tunnel walls is therefore useful for making a fair comparison between experimental and computational data, which will be useful during the validation of this model. While correcting experimental data for blockage effects is possible, simple corrections often neglect the presence of the boundary layer. Modelling the wind tunnels walls instead, should therefore result in a better comparison.

Additionally, this feature will also make it possible to use this model as a means of correcting wind tunnel test results in a way that takes the boundary layer into account. The tested configuration can simply be modelled with and without the wind tunnel walls and the resulting interference effects can be evaluated and subtracted from the experimental data. One of the limitations of this approach though, is the fact that the entire computational model assumes axial symmetry. Non-cylindrical test sections therefore have to be modelled as a cylinder with the same cross sectional area. However, many wind tunnels, including the LTT at Delft University of Technology have a rectangular cross section with cham-fered edges, which helps minimize the effects of this simplification.

Adding the wind tunnel wall representation to the computational model is relatively easy and was done using the same method using which the actuator disc slipstream is represented in potential flow. This is possible since both the actuator disc slipstream and the wind tunnel walls are pipe-like shapes that do not allow flow through their surfaces. The wind tunnel test section was defined as a cylinder with radius R_t and length L_t centered around the location X_t. A distribution of N_t vortex rings and N_t control points was placed along its surface. The geometry of the object is uniform and there and there are no locations that are particularly challenging to model. As a result it was seen appropriate to space the vortex rings and control points evenly along the surface of the cylinder. As can be seen in Figure 6.2, the first vortex ring and the last control point are placed on the leading edge and trailing edge respectively.
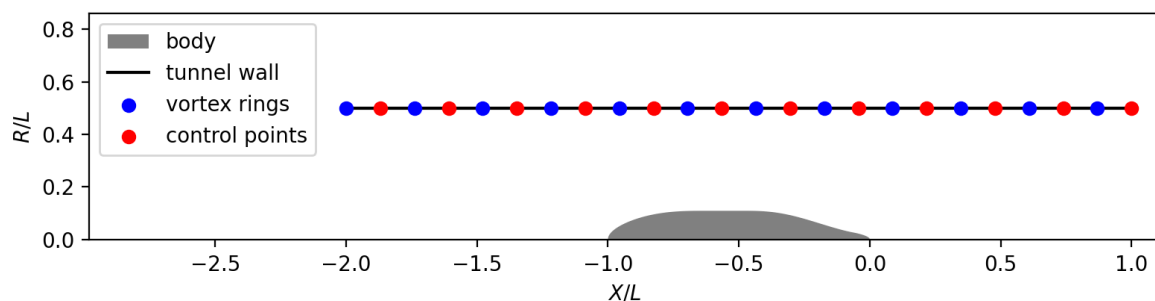

Figure 6.2: Example of a wind tunnel wall modelled using arbitrarily chosen values N_t = 12, $R_t = 0.5L$, $L_t = 3L$ and $X_t = -0.5L$.

Integrating the wind tunnel with the rest of the potential flow model is fairly straightforward. Since the walls are represented in the same way as the actuator disc slipstream, the way in which the linear system is constructed does not need to be modified. The flow angle at each control point is specified to be zero and the vortices and control points can simply be added to those of the actuator disc when constructing the linear system of equations.

6.4. Iterative procedure

Now that the basic aspects of combining the models together have been covered, the mater of creating a single iterative procedure can be discussed. While the combined potential flow model can be solved by linear regression in a single go, several variables need to be solved for iteratively. These include:

- The thickness of the equivalent body
- The radius of the actuator disc slipstream
- The thrust of the actuator disc (in case a net force condition is prescribed)

The procedure for solving all of these variables separately has already been discussed. It is now therefore only a matter of combining the individual algorithms into a single iterative procedure. While this in theory could be done in many ways, the one that was found to work the most reliably will now be described. The solution procedure will be split into three main parts, those being initialization, iteration and output processing.

6.4.1. Initialization

The initialization of the computational model considers all the steps that need to be done before the iterative solution procedure can start. This consists of defining the inputs and discretizing the geometry.

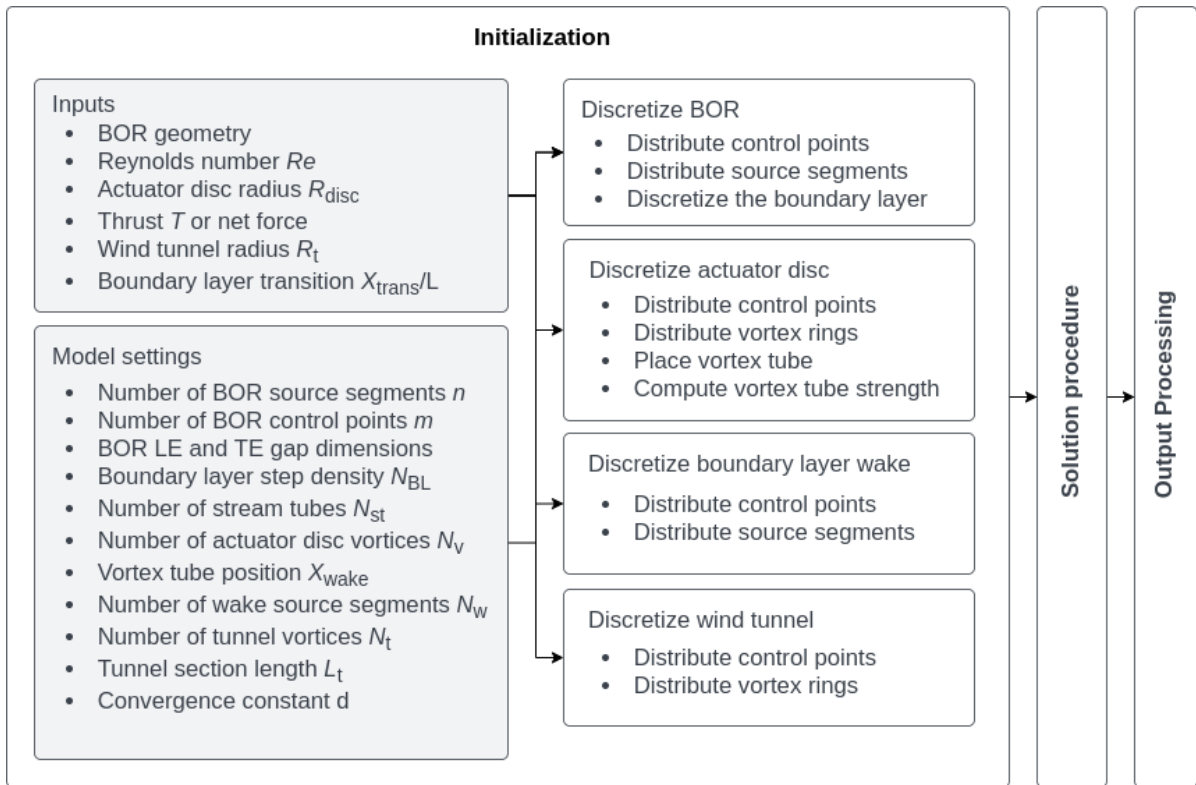A summary of the initialization is shown in a flowchart in Figure 6.3.

Figure 6.3: Flowchart of the initialization procedure of the computational model.

All input variables that describe the flow condition and the geometry of the body, the actuator disc and the wind tunnel are considered to be model inputs. On the other hand, all of the variables related to discretization and the solution procedure are considered to be model settings. While the model inputs define the problem that needs to be solved, the model settings define how the problem is solved and have an impact on the accuracy of the solution as well as the computational effort required.

In this work, use was made of object oriented programming in order to handle the large amount of variables that are used. During the initialization phase, a BOR, a boundary layer, an actuator disc a boundary layer wake and a wind tunnel object is created. The boundary layer object is created as a child of the BOR as it is dependent on its geometry. Each of the objects stores the respective discretization as well as any variables related to the object that are stored during the solution process. This includes, for example, the strengths of source segments or vortex rings, boundary layer properties, drag, thrust and information about the pressure or velocity at various locations. Additionally, all of the objects are the children of a parent "problem" object that stores all of the bodies as well the model settings and is used to execute the steps of the iterative procedure in an orderly manner.

6.4.2. Iterative procedure

Once the initialization is complete, the iterative solution procedure as shown in Figure 6.4 may start.

As can be seen, the iterative procedure is governed by a convergence criterion that is used to check whether the solution is sufficiently converged. Out of the three variables that are being solved iteratively, the radius of the actuator disc slipstream takes by far the longest to converge. The average error in pressure across the slipstream ϵ, as was defined by Equation 5.11 is therefore the only variable that needs to be checked. From experience it was found sufficient to terminate the iteration once $\epsilon/\epsilon_0 < 10^{-5}$, where ϵ_0 is the error at the start. Once the error drops by around 5 orders of magnitude, the output variables of the model should be converged to more than three significant figures.

Within the iteration loop, all of the steps required for iteratively solving the isolated models have been combined in an order that was found to work reliably. The first step however, has to be solving the combined linear system, as without it, executing the other steps is not possible. Once the linear
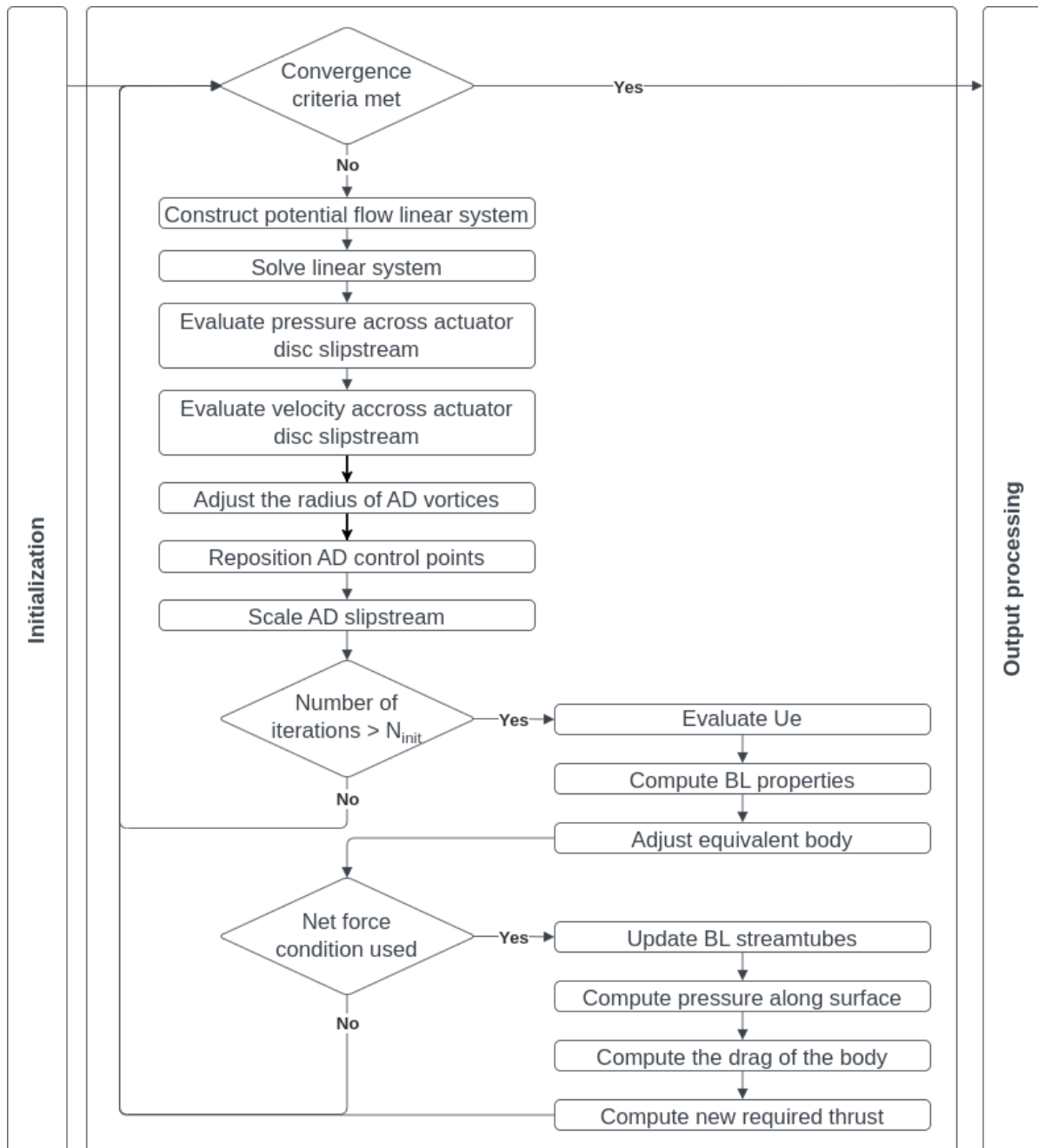
Figure 6.4: Flowchart of the iterative procedure of the computational model.

system is solved, the velocity within the potential flow region can be evaluated at any point. It is therefore possible to now evaluate the velocity and the pressure across the actuator disc slipstream which are the input variables for adjusting the actuator disc slipstream radius.

As can be seen from Figure 6.4, adjusting the actuator disc slipstream is the only thing that is done for the first N_{init} iterations. Occasionally, the procedure was found to diverge if all of the iterative steps were introduced all at once. Having this initialization period was found to prevent this from happening and an N_{init} of 10 was found to be sufficient.

Once the iterative procedure has been initialized, the velocity at the boundary layer edge can also be evaluated, which is used as input for the boundary layer model. Based on the displacement thickness of the boundary layer, the equivalent body can be adjusted. Finally, if the net force acting on the configuration is prescribed as opposed to the thrust of the actuator disc, the next set of steps needs

to be executed. This includes computing the boundary layer stream tubes, evaluating the surface pressure, the drag of the body and finally adjusting the prescribed thrust as necessary.

6.4.3. Output processing

Once the iterative solution procedure has been terminated, the "problem" object is saved and the desired results can be extracted. Some results are directly available and others can be derived with further processing. A summary of what results can be obtained is shown in Figure 6.5.
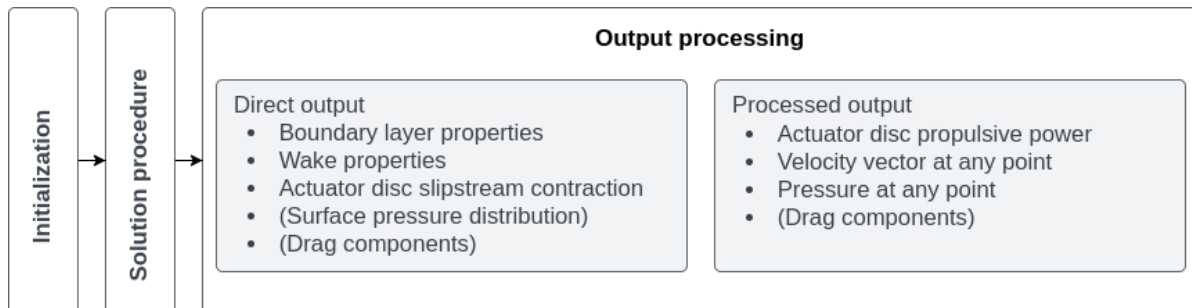

Figure 6.5: Flowchart of the output processing of the computational model.

The output that is directly available are the data that were computed during the last iteration of the solution procedure. The surface pressure and the drag of the body is available if the net force condition was prescribed, otherwise they have to be computed based on the potential flow and boundary layer solutions.

On the other hand, the power of the actuator disc has not been evaluated during the solution process and needs to be done additionally. If desired, the velocity and the pressure can also be evaluated anywhere in the flow field. Outside of the boundary layer this is done using potential flow. Within the boundary layer this has to be done by interpolating the two nearest boundary layer velocity profiles. The velocity within the wake was also computed during the wake correction at discrete locations, but this can also be interpolated to obtain the velocity and therefore also the pressure at any point within the wake.

<div align="right">

7

</div>

Model validation

Validation of the entire computational model will be discussed in this chapter, in order to demonstrate that everything has been properly implemented and is working as intended. This will also give an idea of the accuracy with which the model is capable of predicting the flow around a propulsive fuse-lage. Results obtained by the computational model will be compared to CFD results in section 7.1 and experimental results in section 7.2.

7.1. Validation and analysis using CFD results

Validation using CFD data is performed by modelling a powered configuration as shown in Figure 7.1 in equilibrium (thrust equals drag). Results are compared to those presented in the work of Lv [40], which was already used for validating the equivalent body model in subsection 4.5.1. The inputs characterizing the problem are presented in Table 7.1 and the modelling variables are summarized in Table 7.2.
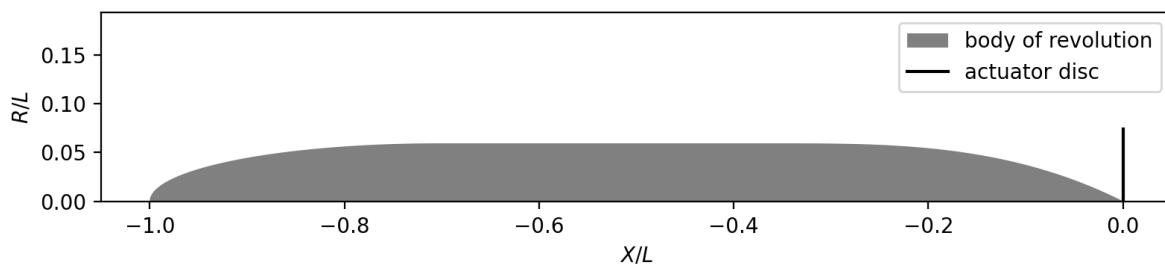

Figure 7.1: The geometry used by Lv [40] for CFD simulations.

**Table 7.1:** Non-dimensional parameters describing the flow condition.

	CFD	present work
Re	2.37×10^6	
M	0.08	0
R_{disc}/L	0.074	
T/D	1	
X_{trans}/L	unknown	0.2

7.1.1. Effect of the wake correction

Before proceeding to validation using the results of Lv, the modelling of this configuration will be used for analysing the effect of the boundary layer correction in order to show that it is working as intended. The configuration was therefore modelled with and without applying the wake correction and the actuator disc slipstream radius distribution is plotted in Figure 7.2.

Table 7.2: Model settings used for computing the results used for validation.

equivalent body	
sources	90
control points	100
removed elements	6
boundary layer elements	1000
boundary layer stream tubes	50
wake stream tubes	50
actuator disc	
vortices	100
X_{tube}/R_{disc}	15
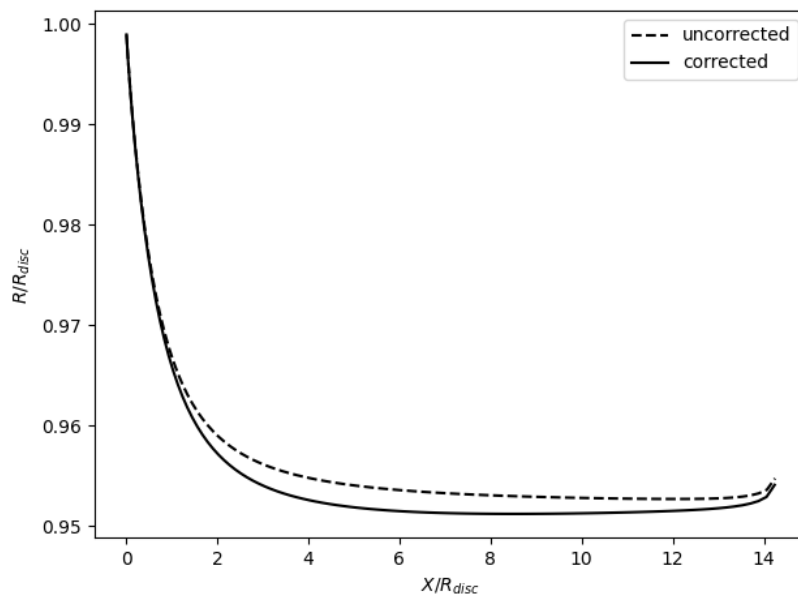
Figure 7.2: The effect of the wake correction on the actuator disc slipstream radius. The BOR shown in Figure 7.1 was modelled in equilibrium.

As can be seen, once the wake is taken into account, the contraction of the slipstream is increased, which is in line with expectations. Additionally, the drag coefficient has increased from 0.2660 to 0.2674 which represents an increase of around 0.5 %. Although the correction has a modest effect, it does contribute to the overall accuracy of the model.

7.1.2. Drag prediction of powered configurations

In order to analyze the capability of the combined computational model to predict the drag, the results for both the powered and clean configurations are compared to those obtained by Lv. The agreement between the computational results and this data set was unfortunately not satisfactory for the unpowered configuration. For the powered configuration, the error in terms of magnitude is slightly lower, but in general still significant, as can be seen from Table 7.3.

While the drag coefficients differ considerably in terms of magnitude, the same general trends are predicted by both models. The addition of the BLI propulsor causes a large increase in pressure drag and a much smaller increase in viscous drag due to the acceleration of air over the tail cone. While the increase in pressure drag coefficient predicted by the two models appears to be very different in terms of percentage, the absolute value by which they are increased is actually not that far off: 0.0092 for CFD and 0.0127 for the present model.

A possible cause that may enlarge the error for the powered configuration is the equilibrium condition that is prescribed. For example if the drag induced by the propulsor is computed larger than it

Table 7.3: The drag increase caused by BLI. Computed resulted are compared to the ones obtained by Lv [40] using CFD.

	Non-BLI		
	C_{D_p}	C_{D_v}	$C_{D_{tot}}$
CFD	0.0292	0.1213	0.1505
current model	0.0172	0.1034	0.1207
	BLI		
CFD	0.0384	0.1217	0.1601
current model	0.0299	0.1038	0.1337
	change in drag		
CFD	+31.7 %	+0.3 %	+6.3 %
current model	+74.1 %	+0.3 %	+ 10.7 %

should be, the equilibrium condition forces the thrust to increase, which further increases the induced drag. However, this does not help explain the large error that was already observed for the unpowered configuration.

Unfortunately, since the CFD results have not been compared to any other data, it is not possible to confirm the cause of the observed discrepancy.

7.2. Validation and analysis using experimental results

In this section, validation and analysis of the computational results will be performed using the experimental data set of van Sluis [41], which was already used for validating the equivalent body model in subsection 4.5.2. Now, use will be made of the results gathered for a powered configuration, which used the six-bladed TUD XPROP propeller placed near the trailing edge of the body. Within the computational model, the propeller is taken into account by placing an actuator disc at the quarter chord location of the propeller blades, as is shown in Figure 7.3.
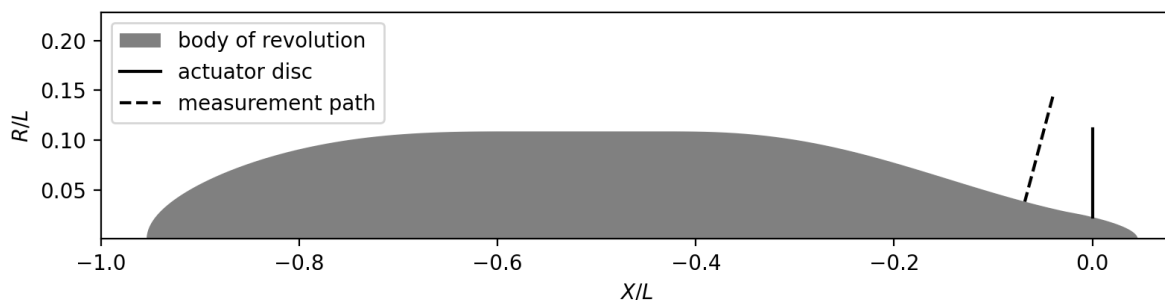
Figure 7.3: The BOR and actuator disc geometry plotted together with the measurement path used in the experiment performed by van Sluis [41].

Pressure measurements were taken along the surface of the tail cone and along the measurement path shown in Figure 7.3. The experiment was carried out at two advance rations of $J = 1.20$ and $J = 1.05$. The net force acting on the configuration at these advance ratios was measured to be 83 N and 132 N respectively. These values have been used as input for prescribing the thrust of the actuator disc. The rest of the non-dimensional parameters describing the setup and the flow condition are summarized in Table 7.4.

One of the problems with replicating the experiment using the computational model, is the fact that the propulsor is not placed at the trailing edge of the body. In fact, it is placed at 95 % of the body length from the leading edge. The condition that the actuator disc is placed at the trailing edge of the body was assumed during the construction of the model and allowed for a much simpler implementation of the boundary layer wake correction. The two options that therefore exist for modelling this configuration are to either place the actuator disc at the trailing edge or to place the actuator disc at its correct location and neglect the effect of the boundary layer wake.

After initial testing, it became clear that the second option is the better one as the agreement of

Table 7.4: Non-dimensional parameters describing the body and flow condition.

	experiment	computation
Re	7.42×10^6	
M	0.175	0
X_{trans}/L	0.2	
R_{disc}/R_b	1.02	
A_t/A_b	16.6	

results was much better in terms of trend. Choosing this option also made sense as the effect of the boundary layer wake correction was shown to be small in subsection 7.1.1, and the effect of moving the actuator disc was observed to be much larger. The model settings used for computing the flow around the powered configuration are summarized in Table 7.5. The condition for prescribing thrust was setup such that the net force acting on the body was always equal to that measured experimentally.

Table 7.5: Model settings used for computing the results presented in this section.

equivalent body	
sources	135
control points	150
boundary layer elements	1500
boundary layer stream tubes	50
actuator disc	
vortices	500
X_{tube}/R_{disc}	15
wind tunnel	
L_t/L	2.74
N_t	100

7.2.1. Effect of the wind tunnel walls

In order to further analyze the effect of the wind tunnel on the pressure distributions, and demonstrate the capability of the model, the powered configurations have been modelled in both free air and inside of the wind tunnel walls for the advance ratios of $J = 1.20$ and $J = 1.05$. The pressure distributions along the surface normal measurement path are presented in Figure 7.4 together with previously computed results for the unpowered configuration.

As can be seen, the modelling the wind tunnel walls seems to be working well also for the powered configuration. The effect of the walls is a decrease in static pressure, as they prevent the flow to expand, as it moves around the body and force it to accelerate instead.

7.2.2. Surface normal pressure distributions

The measured and computed pressure distributions along the surface normal measurement path are compared in Figures 7.5 and 7.6. The uncorrected experimental results are compared with the computational results of the body inside the wind tunnel. Once again, the pressure within the boundary layer has been evaluated using the three increasingly complex methods (uncorrected-surface, surface-surface and flow-surface). The flow-flow method has not been used in this case, due to the difficulty of implementation which was already discussed in Figure 4.5.2. It is expected though, that the difference in pressure predicted by the flow-surface and flow-flow methods would be minimal as the surface curvature in this region is not very large and the boundary layer thickness is not greater than the local radius of the body.

As can be seen, a rather large discrepancy is found between the measured and computed results. While the shape of the curves appears to match very closely, the computational model appears to underpredict the static pressure by a constant amount. The difference in static pressure $\Delta p_s/q_\infty$ is around 0.03 for $J = 1.20$ and 0.04 for $J = 1.05$.

Another important observation that can be made from both figures, but especially from Figure 7.6,
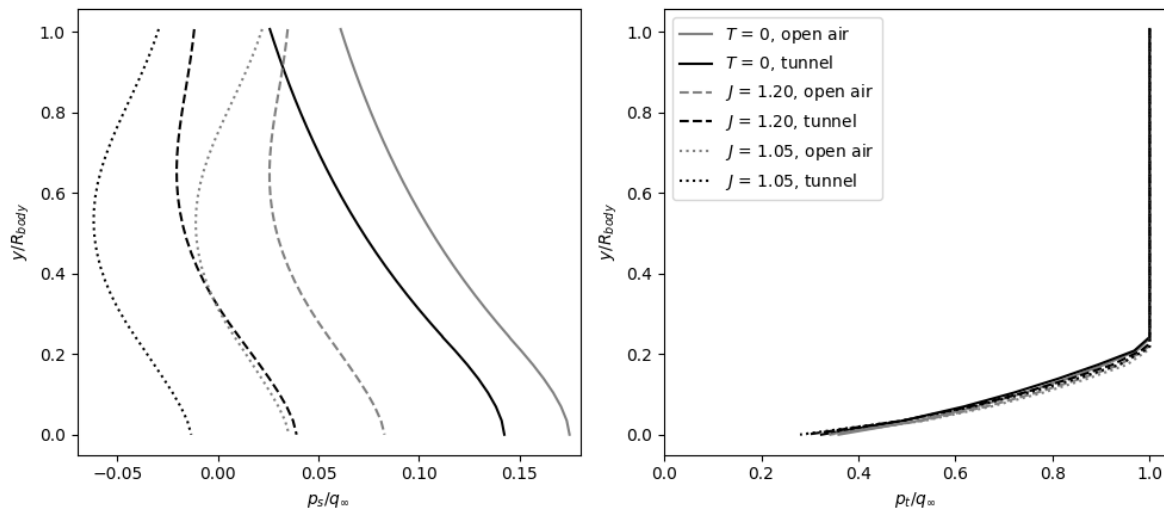
Figure 7.4: Effect of the wind tunnel walls on the static and total pressure computed along the surface normal measurement path. Static pressure within the boundary layer was computed using the flow-surface method.
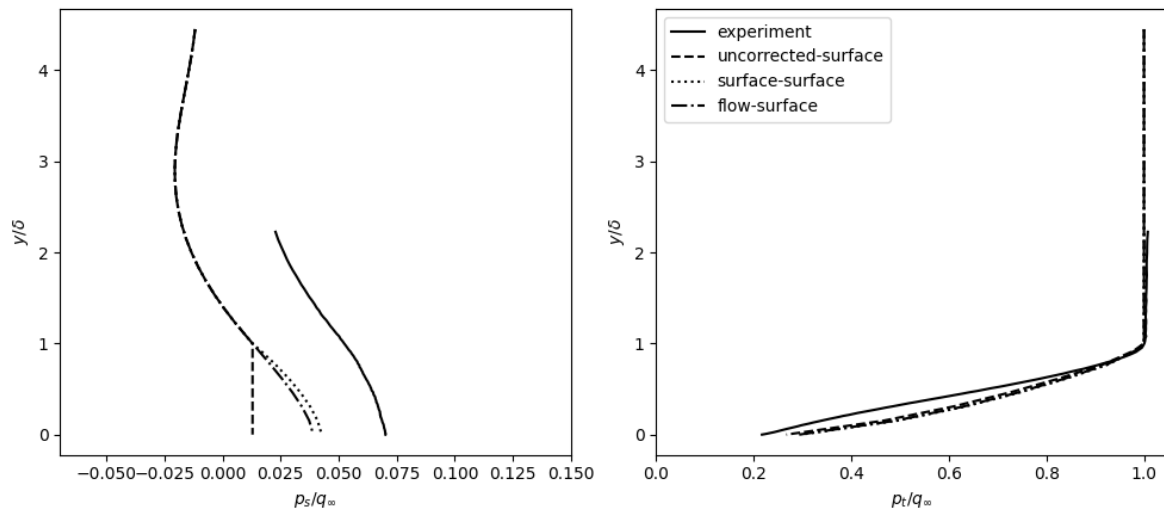

Figure 7.5: Comparison of the computed and measured static and total pressure pressures along the surface normal measurement path for a propeller advance ratio $J = 1.20$.

is that the shape of the static pressure curve is much better predicted when the pressure is computed based on local flow curvature (using the flow-surface method) than when it is computed based on the surface curvature (surface-surface). Additionally, we also see that in this case, the pressure gradient changes abruptly at the edge of the boundary layer when using the surface-surface method, but the transition is smooth when the flow-surface method is used.

The question remains as to why this was not the case for the unpowered configuration which was discussed in Figure 4.5.2. For the unpowered configuration, the shape of the pressure profile does not match nearly as well within the boundary layer and if anything, the surface-surface pressure computing method appears to produce better results.

A possible explanation for this observation is the fact that the propulsor creates a favourable pressure gradient over the tail cone. Without the propulsor, the boundary layer experiences an increase in static pressure, which is a more challenging condition for boundary layer models to work in reliably. The boundary layer predictions could therefore be more accurate for the powered configurations which would explain why the shape of the pressure profile is better predicted as well.
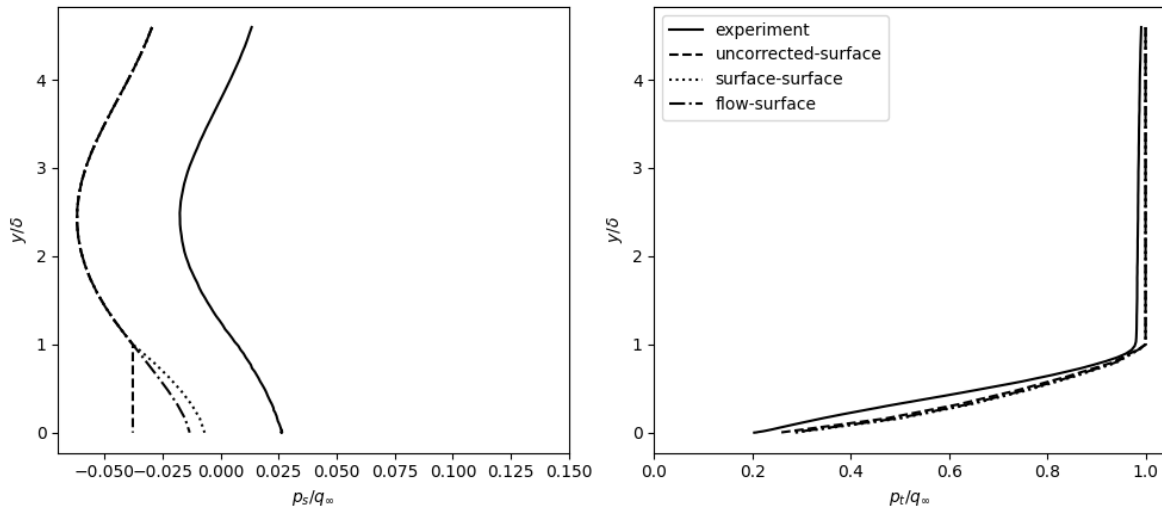
Figure 7.6: Comparison of the computed and measured static and total pressure pressures along the surface normal measurement path for a propeller advance ratio $J = 1.05$.

7.2.3. Surface pressure distributions

A comparison of experimentally measured and computed surface pressure distributions along the tail cone of the body are presented in Figure 7.7. Results for the unpowered configuration are also included for reference.
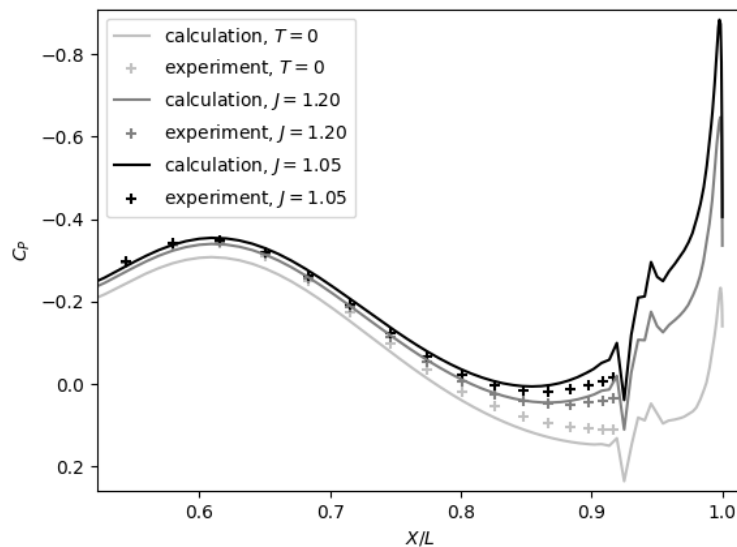

Figure 7.7: Uncorrected pressure coefficient measured along the surface of the body compared with computational results obtained using the flow-flow method for the powered and unpowered configurations inside the wind tunnel.

As can be seen, the agreement between the experiment and computation is in general good, but two main differences can be observed. The first difference is that the drop in the computed pressure coefficient near the trailing edge appears to be larger. While the shape of the curves appears to match very well until $X/L = 0.85$, after this point the measured and computed results start to deviate slightly.

One of the possible causes of this discrepancy could once again be the accuracy of the boundary layer model. Moving downstream over the tail cone, the thickness of the boundary layer grows and the radius of the body decreases. This means that the boundary layer becomes progressively harder to

model and a decrease in accuracy is therefore to be expected.

Another possible explanation is the fact that the propulsor is computationaly modelled as an actuator disc with uniform thrust loading. In reality this will not be the case as the thrust produced by a propeller tends to drop off both near the roots and the tips of the blades. While tip losses are responsible for the decrease of thrust near the tips, the loss of thrust near the root is caused by the lower tangential velocity of the blades. This helps explain the observed discrepancy, as producing less thrust near the surface of the body means that the stream tubes near the surface are accelerated less which results in a smaller pressure drop. The pressure along the surface is therefore expected to be higher in the experimentally measured results.

The second observation that can be made from Figure 7.7 is that the experimentally measured pressure distributions remain the same for the unpowered and both of the powered configurations until around $X/L = 0.65$, but this is not the case for the computational results. Because everything apart from the propeller setting should be identical in all three cases, it is expected that the pressure distributions should become more and more similar to each other with increasing distance from the propeller. The small offset constant offset in computed pressure that is clearly not present in the experimental results is therefore quite peculiar.

A likely explanation of the observed behavior is a difference in how freestream velocity is prescribed during the experiment and in the computational model. In the experimental setup, the velocity in the wind tunnel is measured in the test section, 500 mm upstream of the nose of the model. The power setting of the wind tunnel is then tuned based on this measured velocity.

On the other hand, in the computational model, the body and the wind tunnel (which is simply modelled as a tube around the body), are both placed in a uniform flow field of the prescribed velocity. This means that the velocity at the entrance to the wind tunnel is not prescribed and the presence of the actuator disc may influence it. When the actuator disc produces thrust, the static pressure in front of it is decreased. Since the flow is restricted by the wind tunnel walls, this effect is propagated all the way to the entrance of it. As a result, the effective freestream velocity in the wind tunnel is increased. Computing the velocity 500 mm in from of the body has shown that this is indeed the case and the velocity difference is large enough to explain the observed discrepancy. As a recommendation for future work, the iterative procedure of the computational model could be expanded to adjust the velocity underlying uniform flow field. This would make it possible to prescribe the freestream velocity at a given point in the flow field, which would allow for a fair comparison with experimental results.

An inaccurate velocity predicted by the model within the test section can help explain the discrepancy in pressure observed between experimental results in Figure 7.7 but also in Figures 7.5 and 7.6. It should however be noted, that the experimental results also contain some error. The two data sets of the pressure measured along the surface and the pressure measured normal to the surface contain a single point of overlap: The point on the surface where the surface normal measurement path starts. Comparing the two measurements made at this point reveals a difference ΔC_P of 0.021 for $J = 1.20$ and 0.013 for $J = 1.05$. In terms of order of magnitude, this error is the same as the error between the computational and experimental results shown in Figures 7.5 and 7.6. As a result, a systematic error made during the experiment also cannot be ruled out as a cause of the observed discrepancies.

7.2.4. Drag prediction of the powered configuration

Unfortunately the drag of the body was not measured during the experiment and therefore it is not possible to make a comparison. While the net force acting on the body was measured, this was used as input for the computational model and comparing it therefore also does not make sense (as it will be equal).

While measuring the drag of a powered configuration is considerably more difficult, separating the pressure and viscous drag is impossible. This highlights another use for this computational model. Not only can it be used to correct wind tunnel experimental data, as was discussed previously, in can also be used to estimate the drag of the body and its components based on the experimentally measured net force acting on the configuration. A comparison of the computed drag coefficients of the unpowered and powered configurations is presented in Table 7.6.

Table 7.6: Computed drag coefficients of the powered configuration with two different thrust settings compared with the unpowered configuration. The drag computation is based on the surface pressure distribution calculated using the flow-flow method. The quantity ΔC_d represents the increase in drag of the powered configuration compared to the unpowered one.

J	T/D	C_{d_p}	C_{d_v}	C_d	ΔC_d
	0	0.01593	0.04077	0.05670	
1.20	3.49	0.06196	0.04152	0.10349	+82.5 %
1.05	4.48	0.08627	0.04191	0.12819	+126 %

8
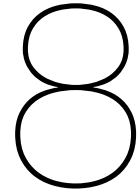
Model demonstration

In order to demonstrate the capability of the computational model, it was decided to model a full sized passenger aircraft featuring a BLI propulsor. The APPU aircraft configuration was chosen for this purpose as is it currently an ongoing project at Delft University of Technology. Since the current model is only capable of simulating an axisymmetric fuselage with a propulsor with constant disc loading, crude assumptions are made regarding the aircraft performance and geometry. The simplifications made are considered acceptable, as the calculations performed in this chapter are only meant to be a proof of concept. For more accurate results, the model should be combined with other computational tools, for example for estimating the aircraft mass, the aerodynamic forces acting on the wing and empennage and the performance of wing mounted engines.

The structure of this chapter will be as follows: The configuration and modelling variables will be first defined in section 8.1. The computational procedure and results will then be presented in section 8.2.

8.1. Problem definition

As a starting point, the aircraft fuselage had to be simplified into an axisymmetric BOR. In order to ensure that the geometry is smooth and easily reproducible, the body was defined using the equations presented by ESDU [38] for defining general BORs. The constants were manually adjusted in order to obtain a body that best resembles the fuselage of an Airbus A320. The resulting geometry is shown in Figure 8.1.

It was next decided to model the APPU aircraft at the cruise condition as passenger transport aircraft of this category typically burn the most fuel during this phase of flight. Minimizing the fuel consumption for this flight condition is therefore usually one of the key goals during aircraft design. The variables defining the APPU aircraft and the flight condition are presented in Table 8.1.

Table 8.1: The basic parameters needed for modelling the APPU aircraft configuration.

Flight condition (cruise)			
Altitude	FL370/11300 m	Air density	0.347 kg/m^3
Mach number	0.78	Velocity	230 m/s
BLI Propulsor			
T_{BLI}	7.5 kN	R_{disc}	1.2 m
Assumed quantities			
Aircraft mass	70 000 kg	X_t/L	0.2

The cruise altitude, the Mach number and the BLI propulsor thrust are estimates currently assumed by the APPU project. The rest of the variables were either derived or assumed. The mass of the aircraft is mission specific and varies during the flight itself. An aircraft mass of 70 000 kg was therefore chosen as a value representative during the early phase of cruise, based on the maximum take-off mass of an A320. This can be up to 79 400 kg for the A320 NEO depending on the exact variant [43].

In order to demonstrate the full capabilities of the model, the APPU aircraft will be compared to a reference configuration, in order to evaluate the PSC. While using the A320 as a reference would be
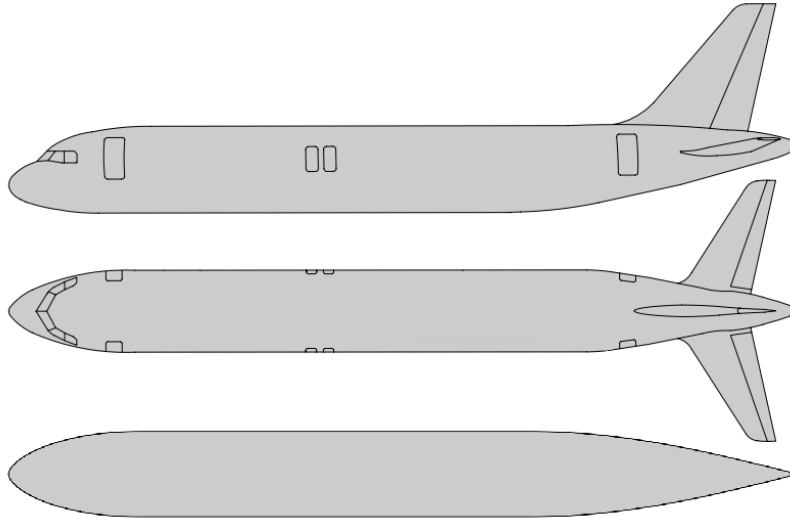
Figure 8.1: Side and top views of the Airbus A320 fuselage [43] together with the axisymmetric approximate representation used for modelling. The nose cone was modelled as an ESDU body 6 with length L_{nose}/L = 0.163 and constant $n = 0.6$. The tail cone was modelled as an ESDU body 9 with length L_{tail}/L = 0.333 and constant $A = 0.8$. [38] The body was scaled to the length and average diameter of the Airbus A320 fuselage, which are 37.57 m and 4.045 m respectively [43].

interesting from the perspective of aircraft development, for the purpose of demonstrating the computational model, it is seen as more appropriate to compare with a more closely related configuration. A reference configuration that is exactly the same, with the only difference being that the propeller is detached from the aircraft fuselage and placed in undisturbed flow. While this configuration is purely academic, as the propulsor is free floating, it will allow the isolated effect gained by immersing the propulsor into the boundary layer to be evaluated. For clarification, a sketch of the two configurations is shown in Figure 8.2.
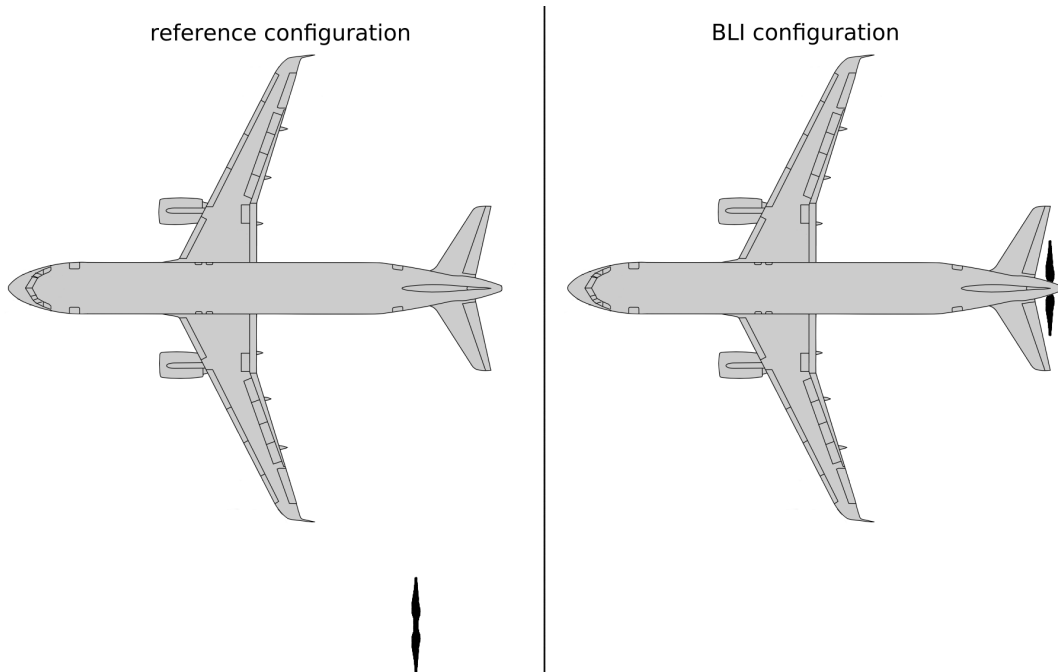

Figure 8.2: A sketch showing the reference and the BLI configurations. The BLI configuration has a propeller attached to the end of the fuselage. The rest of the thrust is provided by under wing engines. The academic reference configuration has a free floating propeller far enough from the aircraft, such that there is no interference between the propulsor and the body. The under wing engines are assumed to produce the same amount of thrust in both configurations. The sketch is not to scale and is based of a drawing provided by Airbus [43].

8.2. Procedure and results

Keeping in mind the goal of making a fair comparison and evaluating the PSC, the following approach was taken to model the two configurations:

1. The drag of the isolated fuselage was evaluated to be $D_{\text{fus, ref}}$ = 6.54 kN by modelling the body without the propulsor.
2. By assuming that the reference configuration has a lift to drag ratio of 17, the total aircraft drag and thrust were computed to be $D_{\text{AC, ref}}$ = $T_{\text{AC, ref}}$ = 40.39 kN based on the aircraft mass.
3. By assuming that the fuselage and the wing are the only major contributors to drag, the drag of the wing is computed by subtracting the fuselage drag from the total drag. A value of D_{wing} = 33.86 kN was obtained and is assumed to hold for both the reference and BLI configurations.
4. Given that the BLI propulsor propulsor produces a thrust of $T_{\text{prop, BLI}}$ = 7.5 kN, the BLI propulsive fuselage is modelled and its drag is evaluated to be $D_{\text{fus, BLI}}$ = 6.76 kN. The propulsive power of the BLI propulsor is computed to be $P_{\text{prop, BLI}}$ = 1.52 MW.
5. The total aircraft drag and thrust of the BLI configuration are then evaluated to be $D_{\text{AC, BLI}}$ = $T_{\text{AC, BLI}}$ = 40.62 kN by adding the wing and the fuselage drag together.
6. Knowing the total aircraft drag and the thrust of the BLI propulsor, the thrust of the wing mounted engines of the BLI configuration is computed to be T_{wing} = 33.12 kN.
7. Assuming that the wing mounted engines produce the same amount of thrust in both configurations, the propeller thrust of the reference configuration is computed to be $T_{\text{prop, ref}}$ = 7.28 kN.
8. The corresponding propulsive power of the propeller of the reference configuration was computed to be $P_{\text{prop, ref}}$ = 1.70 MW by modelling an isolated actuator disc without a body using the previously computed T_{prop}.

The results of the calculations are summarized in Table 8.2 and the computed boundary layer edge is plotted along the body geometry in Figure 8.3. As can be seen, the BLI propulsor produces a similar amount of thrust to the drag of the fuselage and the propulsor radius is similar to the boundary layer thickness. This shows that it is intended to work as a highly efficient wake filling propulsor. Comparing the fuselage drag of the two configurations, we see that by adding the BLI propulsor, the fuselage drag is increased by around 3.4 %. This increase can also be seen on the total aircraft drag. Because the drag of the wing is assumed to not be affected by the propeller, it remains unchanged.

Table 8.2: Summary of the propulsive power and drag and thrust compositions of the reference and BLI configurations.

parameter	units	reference	BLI
D_{fus}	kN	6.54	6.76
D_{wing}	kN	33.86	
D_{AC}	kN	40.39	40.62
T_{prop}	kN	7.28	7.50
T_{wing}	kN	33.12	
T_{AC}	kN	40.39	40.62
P_{prop}	MW	1.70	1.52

The thrust produced by the wing mounted engines was also constrained to stay the same. This was specifically done in order to take the increase in fuselage drag into account when computing the PSC. Looking at the propeller propulsive power of the two configurations, we see that despite the fact that the BLI propeller needs to produce more thrust, its power consumption is significantly lower, which is the desired outcome. The PSC can be computed using Equation 8.1.

$$\text{PSC} = \frac{P_{\text{ref}} - P_{\text{BLI}}}{P_{\text{ref}}} \tag{8.1}$$

By using the values of the propulsive power of the propeller $P_{\text{prop, ref}}$ and $P_{\text{prop, BLI}}$, the PSC of the BLI propulsor can be computed to be 10.9 %. This however, is not the PSC of the entire aircraft, as most of the power is in fact consumed by the under wing engines. By assuming that the under wing engines produce thrust with the same efficiency as the propeller of the reference configuration, which
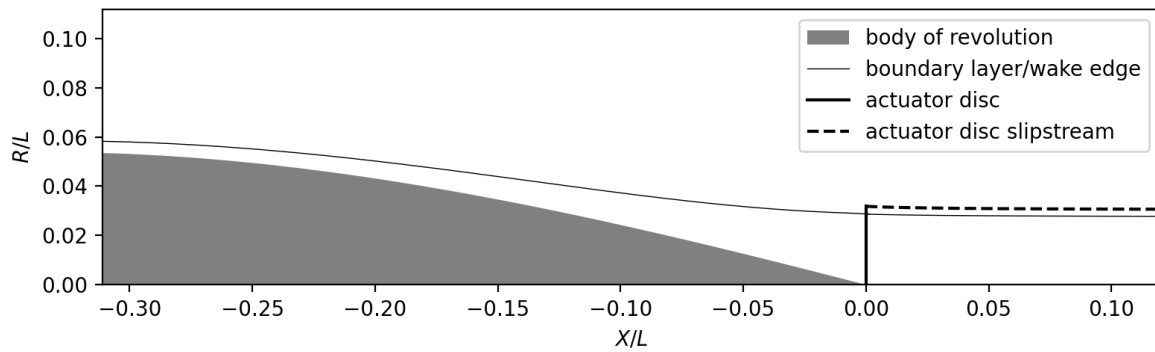
Figure 8.3: The boundary layer and wake plotted along the tail cone of the APPU fuselage.

operates at freestream conditions, their propulsive power can be estimated to be 7.75 MW. Using the total propulsive power, the PSC of the entire configuration then becomes around 2 %. This value however is likely still an overestimate, as the efficiency of turbofan engines is usually much lower than that of propellers due to their larger exhaust speed.

While the calculations performed are largely estimates, the capability of computing the PSC has been demonstrated. The model could therefore be used during conceptual or preliminary aircraft design. For example, the power saving potential of the APPU configuration with respect to the A320 could be obtained by using actual performance metrics of the A320 aircraft and mass estimation tools for evaluating the mass increase resulting from the BLI powertrain introduction.

9

Conclusions and Recommendations

As a part of this work, a computational model has been developed that combines several existing low fidelity computational tools in order to estimate the drag and power of a propulsive fuselage configuration producing a prescribed amount of thrust. The model was tested and critically evaluated and all aspects were shown to work as intended. The value of this work lies mainly in the lessons that were learned during the construction of the model and this work could serve as a basis for further development. Several areas that require further development were identified and recommendations will be made with respect to how the model can be improved and turned into a useful computational tool.

First, the most important modelling aspects will be discussed in section 9.1. The accuracy and the speed of the computational model will be then covered in section 9.2. The usability of the model will be treated in section 9.3 and finally, recommendations will be made in section 9.4.

9.1. Methodology and best practices

The first part of this work consisted of constructing an equivalent body model by combining a potential flow model of a BOR together with a laminar and a thick axisymmetric boundary layer model. Computational results have been shown to agree well with other computational as well as experimental results regarding the flow around an isolated body of revolution. The following best practices are considered the most important for creating a stable equivalent body model suitable for being combined with an actuator disc model:

BOR discretization:
- A cosine distribution is recommended for discretizing the body along the streamwise direction. This ensures proper functioning of the boundary layer model over the leading and trailing edges.
- In case the BOR has a blunt trailing or leading edge, a small gap should be left between such an edge and the start of the source segment distribution.
- The number of control points should be larger than the number of source segments. This results in a linear system that is overdetermined and can be solved using least square regression. This was found to be the most effective way of dealing with ill-conditioned linear systems.

Surface pressure computation:
- Pressure variations across the boundary layer were found to have a significant impact on the drag of the body. As a part of this thesis, several methods for computing the pressure along the surface of the body were explored and analyzed. Estimating the surface pressure using local flow curvature within the boundary layer was found to be necessary.
- Discretization of the boundary layer into stream tubes was found to be a robust way for estimating the local flow curvature within the boundary layer. The development of the stream tubes was computed using mass flow conservation based on boundary layer velocity profiles.
- In case the trailing edge of the body is blunt, the surface pressure should be computed by integrating the pressure correction along a path perpendicular to the local flow direction. In case

the surface curvature near the trailing edge is not large, integrating the pressure correction in the direction perpendicular to the surface is acceptable.

As a second step of this work, a potential flow actuator disc model was constructed. The model, which is based on a vortex ring distribution was modified, in order to make it suitable for integrating it with the equivalent body model. The results of the modified model were found to agree reasonably well with published results obtained by the original model. The following changes were made to the model and are considered essential:

Adjustments made to the actuator disc model
- The locations of control points at which velocity needs to be evaluated were changed such that velocity does not need to be evaluated at the locations of vortex rings. This improved the stability of the model, eliminated the need to use a vortex kernel radius and made the model easier to use with an arbitrary discretization.
- The convergence scheme of the actuator disc model was adjusted. In the original model, both the vortex strengths and radii are solved iteratively. In the new scheme that was proposed, only the vortex radii are solved iteratively and the vortex strengths are solved using a linear system. This eliminates the need to compute the stream function, which was one of the things preventing the model from being combined with the equivalent body model. Further, the new convergence scheme was also found to be more stable.

The third step of this work consisted of combining the equivalent body and the actuator disc models together. While the two models can be integrated by simply combining their linear systems used for solving potential flow, doing so does not take the boundary layer wake into account. Taking the wake into account is necessary as it causes an additional contraction of the actuator disc slipstream, which increases the drag of the body. As a result the wake was modelled by discretizing it into stream tubes. Within the potential flow model, the wake was taken into account by extending the equivalent body model downstream.

Finally, an option for modelling wind tunnel walls as a uniform cylinder was also implemented. The walls were considered in potential flow only and were modelled using the same approach as the slipstream of the actuator disc. The difference in pressure caused by the presence of the wind tunnel walls was found to agree closely with that predicted by a third party panel code.

9.2. Accuracy and computational speed

Validation of the computational model was performed by comparison with experimental and CFD results. The comparison with CFD results was unfortunately inconclusive, as the pressure drag was underpredicted by the present model by up to -41 %. Due to the limited data available, it was not possible to determine the source of the error.

On the other hand, the agreement with experimental data was much better. The computed drag of the body and the pressure within the boundary layer agreed well with the experiment for the unpowered configuration. The error in total drag was less than 1 %. For the powered configuration, the drag was unfortunately not measured experimentally. However, the trend of the pressure measurements was still very good. A small systematic error was observed however the source of this error was concluded to be at least partially a calibration error of measurement devices. The main reason for this being is that an error of similar magnitude was also observed between two experimental measurements made at the same location.

Several simplifications and assumptions have been made during the construction of the model. The ones that likely have the largest impact on the model accuracy can be summarized as follows:

Simplifications and assumptions impacting the model accuracy
- The turbulent boundary layer used, may not be able to accurately represent the boundary layer over the tail cone. Boundary layer models are known to not perform well in adverse pressure gradients, particularly over bodies of revolution when the boundary layer thickness becomes large with respect to the radius of the body. The boundary layer model also assumes that the flow is parallel to the surface. However, this was observed to not be the case in the trailing edge region.

- The actuator disc model assumes a uniform increase in pressure. This is not realistic of a propeller as the thrust produced typically drops towards the root and the tip.
- The actuator disc model including the boundary layer wake correction is inviscid. This means that the diffusion of velocity across the slipstream and due to non uniform inflow is not taken into account.

While the computational speed of the model has not been discussed explicitly, from a user experience it can be concluded that the model has potential to be competitive with CFD simulations. Even though, the model was constructed in Python and the code was not optimized for computational speed, it was still possible to compute a solution in the order of minutes. Another advantage of this model is that the setup is simple and no meshing is required.

9.3. Usability of the model

Once validated, the model has been used for analyzing the BLI benefit of the APPU propulsive fuselage concept and was shown to provide realistic power saving estimates. The PSC of the BLI propulsor was computed to be 10.9 % and the PSC of the entire configuration was estimated to be 2 %. The model can therefore be a useful tool for evaluating the performace of BLI configurations during the early design phase.

Thanks to the possibility of modelling wind tunnel walls, the model can also be used for correcting experimental data. Additionally, the model can also be used to estimate quantities that cannot be measured experimentally, such as the pressure drag and the viscous drag of the body.

9.4. Recommendations

During the construction of the model, several opportunities for improving the accuracy and functionality have been encountered and will be now summarized.

- The actuator disc model can be expanded in order to allow for a non-uniform thrust distribution. This can be done by stacking multiple actuator discs of increasing radii on top of each other.
- The model could be coupled with a blade element theory model. This would allow for computation of the thrust distribution based on propeller geometry, as well as an optimization of the propeller geometry. Additionally, the torque and shaft power of the propeller could also be evaluated.
- The boundary layer wake correction could be expanded to work for an actuator disc placed upstream of the trailing edge. This would be particularly useful, as in practice a propeller cannot be placed right at the triling edge due to structural reasons.
- The model for computing the boundary layer wake could be replaced with a viscous wake model, that would be able to predict the diffusion of velocity across the wake.
- The iterative procedure could be expanded to add an option of prescribing the flow velocity at a particular location in the flow field, rather than at an infinite distance away. This would allow for a better comparison of computed and wind tunnel test results.
- Taking the lessons learned into account, the computational model could be rewritten in a more computationally efficient programming language to increase the computational speed.

References

[1] European Commission et al. *Flightpath 2050 : Europe's vision for aviation : maintaining global leadership and serving society's needs*. Publications Office, 2011. DOI: `doi/10.2777/50266`.

[2] L. H. Smith Jr. "Wake ingestion propulsion benefit". In: *Journal of Propulsion and Power* 9.1 (1993), pp. 74–82. DOI: `10.2514/3.11487`.

[3] A. Seitz, A. Luisa Habermann, and M. van Sluis. "Optimality considerations for propulsive fuselage power savings". In: *Proceedings of the Institution of Mechanical Engineers, Part G: Journal of Aerospace Engineering* 235.1 (2020), pp. 22–39. DOI: `10.1177/0954410020916319`.

[4] S. Stückl et al. *DisPURSAL D1.2 – Report on the Technology Roadmap for 2035*. Tech. rep. Jan. 2015. URL: `https://cordis.europa.eu/docs/results/323/323013/final1-dispursal-d1-2-final.pdf`.

[5] J. R. Welstead and J. L. Felder. "Conceptual Design of a Single-Aisle Turboelectric Commercial Transport with Fuselage Boundary Layer Ingestion". In: *54th AIAA aerospace sciences meeting*. Jan. 2016, p. 1027. DOI: `10.2514/6.2016-1027`.

[6] A. Seitz et al. "Proof of Concept Study for Fuselage Boundary Layer Ingesting Propulsion". In: *Aerospace* 8 (Jan. 2021), p. 16. DOI: `10.3390/aerospace8010016`.

[7] A. Arntz et al. "Exergy-based Aircraft Aeropropulsive Performance Assessment: CFD Application to Boundary Layer Ingestion". In: *32nd AIAA Applied Aerodynamics Conference*. 2014, p. 2573.

[8] H. C. McLemore. *Wind-Tunnel Tests of a 1/20-Scale Airship Model With Stern Propellers*. Tech. rep. TN-D-1026. National Aeronautics and Space Administration, Jan. 1962. URL: `https://apps.dtic.mil/sti/citations/AD0270084`.

[9] A. L. Habermann et al. "Performance bookkeeping for aircraft configurations with fuselage wake-filling propulsion integration". In: *CEAS Aeronautical Journal* 11.2 (Dec. 2019), pp. 529–551. DOI: `10.1007/s13272-019-00434-w`.

[10] M. Drela. "Power Balance in Aerodynamic Flows". In: *AIAA Journal* 47.7 (July 2009), pp. 1761–1771. DOI: `10.2514/1.42409`.

[11] R. T. Kawai, D. M. Friedman, and L. Serrano. *Blended Wing Body (BWB) Boundary Layer Ingestion (BLI) Inlet Configuration and System Studies*. Tech. rep. CR-214534. NASA, Dec. 2006. URL: `https://ntrs.nasa.gov/citations/20070006754`.

[12] E. M. Greitzer et al. *N+3 Aircraft Concept Designs and Trade Studies, Final Report Volume 1*. Tech. rep. NASA/CR—2010-216794/VOL1. NASA Glenn Research Center, Dec. 2010. URL: `https://ntrs.nasa.gov/citations/20100042401`.

[13] A. Uranga et al. "Preliminary Experimental Assessment of the Boundary Layer Ingestion Benefit for the D8 Aircraft". In: *52nd Aerospace Sciences Meeting*. 2014, p. 0906. DOI: `10.2514/6.2014-0906`.

[14] M. Drela. "Development of the D8 transport configuration". In: *29th AIAA Applied Aerodynamics Conference*. June 2011, p. 3970. DOI: `10.2514/6.2011-3970`.

[15] A. Uranga et al. "Boundary Layer Ingestion Benefit of the D8 Transport Aircraft". In: *AIAA Journal* 55.11 (Nov. 2017), pp. 3693–3708. DOI: `10.2514/1.j055755`.

[16] A. T. Isikveren et al. "Distributed propulsion and ultra-high by-pass rotor study at aircraft level". In: *The Aeronautical Journal* 119.1221 (2015), pp. 1327–1376. DOI: `10.1017/s0001924000011295`.

[17] A. Seitz and C. Gologan. "Parametric design studies for propulsive fuselage aircraft concepts". In: *CEAS Aeronautical Journal* 6.1 (2015), pp. 69–82. DOI: `10.1007/s13272-014-0130-3`.

[18] L. Wiart et al. "Aeropropulsive Performance Analysis of the NOVA Configurations". In: *30th Congress of the International Council of the Aeronautical Sciences*. Sept. 2016.

[19] A. Yildirim et al. "Performance Analysis of Optimized STARC-ABL Designs Across the Entire Mission Profile". In: *AIAA Scitech 2021 Forum*. 2021, p. 0891.

[20] B. Della Corte et al. "Power Balance Analysis Experiments on an Axisymmetric Fuselage with an Integrated Boundary-Layer-Ingesting Fan". In: *AIAA Journal* 59.12 (2021), pp. 5211–5224. DOI: `10.2514/1.j060570`.

[21] A. R. Kriebel. *Interference Between a Hull and a Stern-Mounted Ducted Propeller*. Tech. rep. 161. Vidya, Sept. 1964. URL: `https://apps.dtic.mil/sti/citations/AD0612019`.

[22] G. A. M. van Kuik and L. E. M. Lignarolo. "Potential Flow Solutions for Energy Extracting Actuator Disc Flows". In: *Wind Energy* 19.8 (2015), pp. 1391–1406. DOI: `10.1002/we.1902`.

[23] M. Drela. "XFOIL: An analysis and design system for low Reynolds number airfoils". In: *Low Reynolds number aerodynamics*. Springer, 1989, pp. 1–12.

[24] V. C. Patel, A. Nakayama, and R. Damian. "Measurements in the thick axisymmetric turbulent boundary layer near the tail of a body of revolution". In: *Journal of Fluid Mechanics* 63.02 (1974), pp. 345–367. DOI: `10.1017/s0022112074001170`.

[25] B. Della Corte et al. "Experimental Investigation of the Flow Past and Axisymetric Body at Low Speed". In: *Proceedings of the 24th International Society of Air Breathing Engines Conference*. 2019, pp. 1–22.

[26] N. A. Balantrapu et al. "Turbulent Boundary Layer in a Strong Adverse Pressure Gradient Over a Body of Revolution". In: (July 2019).

[27] V. C. Patel. *A simple integral method for the calculation of thick axisymmetric turbulent boundary layers*. Tech. rep. IIHR Report No. 150. Iowa Institute of Hydraulic Research, The University of Iowa, 1973.

[28] P. D. Chappell. *The influence of body geometry and flow conditions on axisymmetric boundary layers at subcritical Mach numbers*. Tech. rep. 79020. ESDU, Sept. 1979. URL: `https://www.esdu.com/cgi-bin/ps.pl?sess=unlicensed_1220126142051nqp&t=doc&p=esdu_79020a`.

[29] T. Von Karman. *Calculation of Pressure Distribution on Airship Hulls*. Tech. rep. 6. 1930.

[30] W. L. Oberkampf and L. E. Watson Jr. "Incompressible potential flow solutions for arbitrary bodies of revolution". In: *AIAA Journal* 12.3 (1974), pp. 409–411.

[31] Gene H Golub, Per Christian Hansen, and Dianne P O'Leary. "Tikhonov regularization and total least squares". In: *SIAM journal on matrix analysis and applications* 21.1 (1999), pp. 185–194.

[32] C. Kaplan. *Potential flow about elongated bodies of revolution*. Tech. rep. NACA Report No. 516. 1936.

[33] G. Muhammad, N.A. Shah, and M. Mushtaq. "Calculation of Flow Past a Sphere Near the Ground Using an Indirect Boundary Element Method". In: *Kragujevac Journal of Science* 32 (2010), pp. 31–39.

[34] V. C. Patel. *An Experimental Study of the Thick Turbulent Boundary Layer Near the Tail of a Body of Revolution*. Tech. rep. IIHR Report No. 142. Iowa Institute of Hydraulic Research, The University of Iowa, Jan. 1973.

[35] N. Rott and L.F. Crabtree. "Simplified Laminar Boundary-Layer Calculations for Bodies of Revolution and Yawed Wings". In: *Journal of the Aeronautical Sciences* 19.8 (1952), pp. 553–565.

[36] M. R. Head. *Entrainment in the turbulent boundary layer*. Tech. rep. Reports and Memoranda No. 3152. Ministry of Aviation, 1958. URL: `https://citeseerx.ist.psu.edu/viewdoc/download?doi=10.1.1.227.1754&rep=rep1&type=pdf`.

[37] J. Anderson. *Fundamentals of Aerodynamics*. 6th. New York: McGraw-Hill Education, 2017.

[38] P. D. Chappell. *Geometrical characteristics of typical bodies*. Tech. rep. 77028. ESDU, 1977. URL: `https://www.esdu.com/cgi-bin/ps.pl?sess=unlicensed_1230214143429pzs&t=doc&p=esdu_77028g`.

[39] N. Korttkov and C. Hirsch. "Prediction of the effects of surface curvature and rotation in a turbulent boundary layer". In: *Bulletins de l'Académie Royale de Belgique* 70.1 (1984), pp. 109–124.

[40]   P. Lv et al. "Performance Analysis of Wake and Boundary-Layer Ingestion for Aircraft Design". In: *Journal of Aircraft* 53.5 (2016), pp. 1517–1526. DOI: 10.2514/1.c033395.

[41]   M. van Sluis, T. Sinnige, and L.L.M Veldhuis. *"Unsteady aerodynamic interaction of a fuselage boundary layer ingesting propeller"*. To be published 2023.

[42]   G. A. M. Van Kuik. *The Fluid Dynamic Basis for Actuator Disc and Rotor Theories: Revised Second Edition*. IOS Press, 2022.

[43]   AIRBUS. *Aircraft characteristics airport and maintenance planning*. 2017.

A
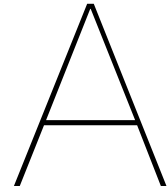
Validation of the turbulent boundary layer model

In order to check that model was correctly implemented, verification was performed using the four sets of results presented in the work of Patel [27] and the results are shown in Figures A.1 to A.4. In each set, the two left most plots represent the model inputs: The body geometry and the corresponding velocity. The four other plots compare the outputs of the model to Patel's results. In each case the integration was initialized using the first δ_2 and H data points of the validation data sets. Note that validation data for the friction coefficient C_f is not available in the first set and the only data set which contains a hypothetical velocity distribution input is the second one.

As can be seen, the agreement between the computed results and those of Patel is reasonably good. A likely source of error causing deviations is the inaccuracy of readings, considering that all data had to be read from poor quality graphs and the boundary layer model is quite sensitive to changes in geometry.
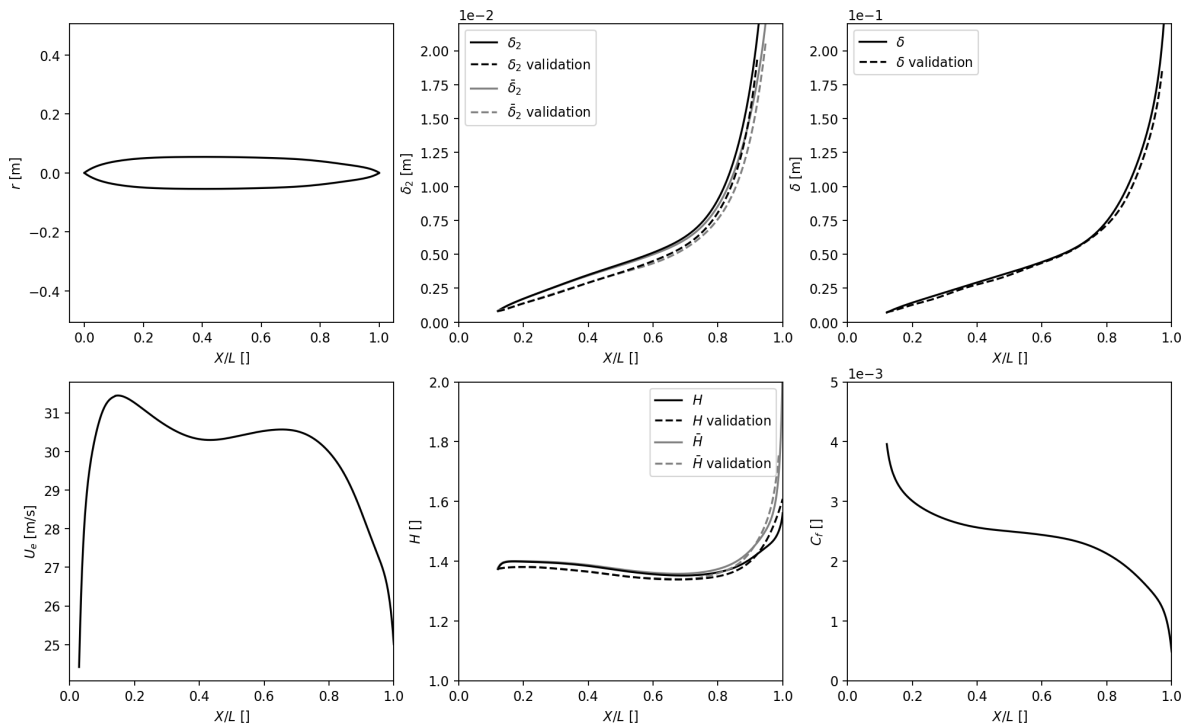

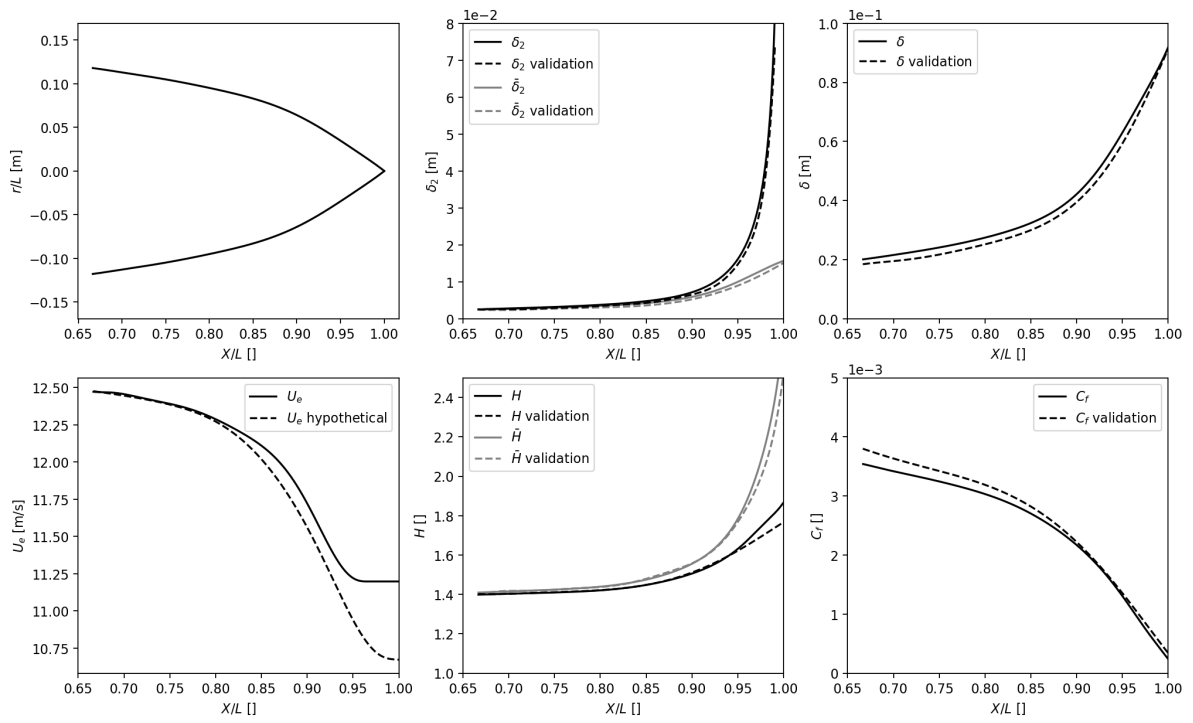**Figure A.1:** External flow over a model of the Akron airship.

68

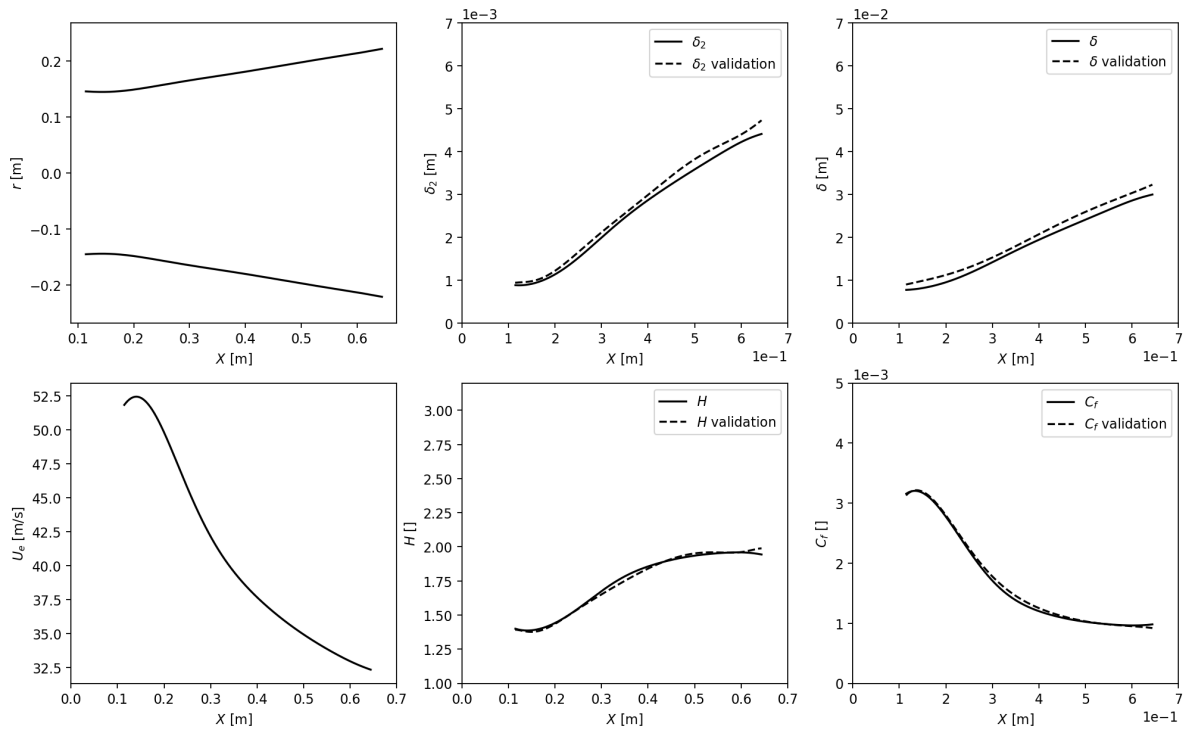**Figure A.2:** External flow over the aft cone of a BOR.

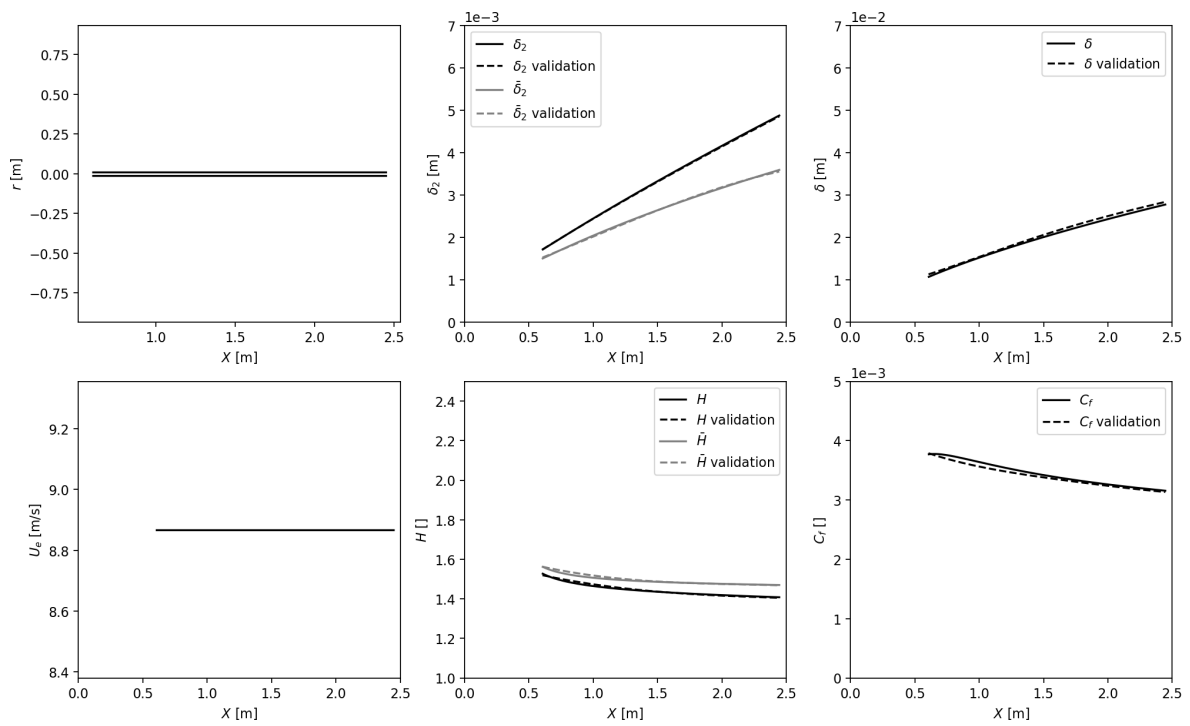**Figure A.3:** Internal flow through a conical diffuser.

Figure A.4: External flow over a cylinder of constant radius.

B

Induced velocities in potential flow

The velocity components U_X and U_R induced by a vortex ring i of strength Γ_i at the location (X, R) are given by Equation B.1 and Equation B.2 where $K(k)$ and $E(k)$ are the complete elliptic integrals of the first and second kind [22].

$$U_X = \frac{\Gamma_i}{4\pi} R_i \left[\left(R_i + R\frac{A}{B} \right) I_2 - \frac{R}{B} I_1 \right] \tag{B.1}$$

$$U_R = \frac{\Gamma_i}{4\pi} R_i \left(\frac{X - X_i}{B} \right) (I_1 - A I_2) \tag{B.2}$$

where $\qquad A = (X - X_i)^2 + R^2 + R_i^2, \qquad B = -2 R_i R$

$$I_1 = \frac{4}{\rho_2} K(k), \qquad I_2 = \frac{4}{\rho_2^3} \frac{E(k)}{1-k}, \qquad k = \sqrt{1 - \left(\frac{\rho_1}{\rho_2} \right)}$$

$$\rho_1 = \sqrt{(X - X_i)^2 + (R - R_i)^2}, \qquad \rho_2 = \sqrt{(X - X_i)^2 + (R + R_i)^2}$$

Similarly, the velocity components U_X and U_R induced induced at the location (X, R) by a semi-infinite vortex tube symmetric around the X axis that starts at the location (X_t, R_t) and extends infinitely in the positive X direction are given by Equation B.3 and Equation B.2. Here, γ is the vortex strength and $\Pi(\alpha^2, k)$ is the complete elliptic integral of the third kind.

$$U_X = -\frac{\gamma}{4\pi} \Theta \tag{B.3}$$

$$U_R = -\frac{\gamma}{2\pi} \sqrt{\frac{R_t}{R}} \left(\left(\frac{2}{k} - k \right) K(k) - \frac{2}{k} E(k) \right) \tag{B.4}$$

where $\qquad \Theta = \left(\frac{R_t - R}{|R_t - R|} + 1 \right) \pi + 2 \frac{X - X_t}{\rho_2} \left(K(k) - \frac{R - R_t}{R + R_t} \Pi(\alpha^2, k) \right)$

$$\alpha = 2 \frac{\sqrt{R_t R}}{R_t + R}$$